POLITECNICO DI MILANO

SCUOLA INTERPOLITECNICA DI DOTTORATO

Doctoral Program in Bioengineering

XXVII Cycle

Final Dissertation

Advanced microfluidic platforms for investigating the role of microenvironmental signaling on stem cell fate

Paola Occhetta

Tutors
Prof. Alberto Redaelli
Ing. Marco Rasponi

Co-ordinator of the Research Doctorate Course
Prof. Andrea Aliverti

05/03/2015

Table of contents

List of Abbreviations

2D	Bi-dimensional
3D	Three-dimensional
BSA	Bovine Serum Albumin
CFD	Computational Fluid Dynamic
CM	Center of Mass
CP	Continuous Phase
DP	Disperse Phase
EBs	Embryoid Bodies
ECM	Extracellular Matrix
Edu	5-ethynyl-2'-deoxyuridine
ELF97	(Enzyme-Labeled Fluorescence) phosphatase substrate
FBS	Fetal Bovine Serum
FGF2	Fibroblast Growth Factor 2
G'	Storage Modulus
G''	Loss Modulus
GelMA	Gelatin Methacrylate
GFP	Green Fluorescent Protein
HB	Staggered Herringbone
^{1}H-NMR	proton Nuclear Magnetic Resonance
hBM-MSC	human Adult Bone Marrow-derived Mesenchymal Stem/Stromal Cell
HUVECs	Human Umbilical Vein Endothelial Cells
LED	Light Emitting Diode
lPEI	linear Polyethylenimine
LVR	Linear Viscoelastic Region
ME	Mixing Efficacy

MM	Maintaining Medium
OM	Osteogenic Medium
PBS	Phosphate Buffer Saline
PDMS	Poly(dimethyl-siloxane)
PEGDA	Polyethylen Glycol Diacrylate
PFA	Paraformaldehyde
PI	Photoinitiator
PLL	Poly-L-Lysine
PMP	photo-mold-patterning
Re	Reynolds number
rhWnt3a	wingless-type MMTV integration site family member3a
SAOS2	Primary osteogenic sarcoma human cell line
SDG	Serial Dilution Generator
SFM	Serum Free Medium
SI	Selectivity Index
TE	Tissue Engineering
TGFβ3	Transforming growth factor β3
TMSPMA	3-(trimethoxysilyl) propyl methacrylate
U87-MG	human glioblastoma-astrocytoma epithelial-like
UV	Ultraviolet
VA-086	2,2-Azobis (2-methyl-*N*-(2-hydroxyethyl)propionamide)
µPIV	Microparticles Image Velocimetry

1

In vitro models in stem cell biology: from traditional to advanced culture platforms

1.1 The native cellular microenvironment

In vivo, cells are surrounded by a complex multi-factorial environment characterized by specific physicochemical properties (temperature, pH, oxygen tension), which provide cells with exogenous stimuli deriving from soluble factors, cell-matrix interactions, and cell-cell contacts. The orchestrated interplay of these biochemical and physical extracellular cues, referred to as *cell microenvironment*, regulates cells structure, function and behavior, ultimately guiding their fate [1].

The biochemical microenvironment is constituted by the combined role of cytokines, growth factors, hormones and other diffusive biomolecules. This environment contributes to the activation of complex signaling pathways, which modulate intrinsic regulatory mechanisms and, in turn, determine cell fates [2]. Such biochemical extracellular signaling takes place through autocrine and paracrine intercellular communication mechanisms, relying on the diffusion of biomolecules affecting the secreting cell (autocrine) or neighboring cells (paracrine). Their efficacy on the modulation of cell behavior depends on systems of proteins (including cell-surface receptors and intracellular signaling proteins) that enable cells to respond to a particular subset of signals in a specific way [3]. Moreover, characteristic properties of biochemical factors, including concentrations, half-life, and receptor binding affinities of the ligand of interest, contribute to determine their dynamic role on modulating the behavior of a specific cell [4].

In addition to soluble signals, also the solid-state microenvironment, consisting of extracellular matrix (ECM) factors, proteins immobilized to the ECM, and neighboring cells, plays a key role in regulating cell fate [5]. Indeed, the majority of cells in the body are adhesive-dependent, relying on the attachment to the surrounding ECM to survive. Physical communication between cells and ECM occurs by means of integrins, transmembrane receptors defining bridges between cell and ECM proteins. Integrins are also responsible for the mechanotransduction of exogenous signals, such as the chemical composition and mechanical status of the ECM, known to drive the regulation of cellular processes including migration, proliferation, differentiation and apoptosis [6]. Moreover, there are specialized tissues in which the selective adhesion of cells between each other's is crucial for the maintenance of their physiological structure and function (i.e. myocardium, endothelium). The regulation of such specialized interactions is governed by several cell adhesion and junction molecules. Among them, a family of Ca^{2+}-dependent adhesion molecules, named

cadherins, plays a key role in tissue morphogenesis, through the control of cell polarity and the dynamic regulation of cell adhesive contacts [7] during both the development of new tissues and the controlled growth and turnover of adult ones [8].

Together, soluble factors, matrix-bound cues, cell-cell contacts and cell-matrix adhesions form a complex three-dimensional (3D) cell microenvironment, which is also characterized by spatio-temporal dynamic gradients, acting as signals themselves to regulate cell function and behavior [9]. While chemical gradients are generated within the cell microenvironment due to diffusion mechanisms, gradients in ECM mechanical properties and compositions are intrinsically related with the heterogeneity of tissue structures and usually characterize the boundaries between different tissues [10].

Considering the described complexity of the native cell microenvironment, *in vitro* models recapitulating the dynamic combinatorial role of biochemical and physical factors are required to better understand the key pathways regulating cells behavior. The development of such accurate *in vitro* models is of particular interest in those applications of cell biology, such as drug screening studies, investigation over tissues morphogenesis, optimization of tissue engineering (TE) protocols, in which cell responses and long-term tissue functionalities are strictly dependent on multiple factors that act synergistically.

1.2 Macroscale *in vitro* models

To date, much of the current understanding in cell biology relies on traditional bi-dimensional (2D) *in vitro* cell culture models, which mainly consist on the static culture of cells seeded on polystyrene flat surface plates (mm to cm in characteristic dimensions). Such substrates, however, poorly mimic the native cellular microenvironment. Indeed, the 2D plastic surfaces usually exploited for culturing cells (i.e. Petri dishes, multiwell plates, flasks) feature levels of stiffness that are orders of magnitude higher than those found *in vivo*. They also lack in presenting 3D cues typical of the native cell physical microenvironment. Moreover, while cells are physiologically organized in proximity to each other, thus facilitating the intercellular communications, traditional *in vitro* culture environments are characterized by long distances among cells, and cell-cell interactions are rarely organized and mainly dependent on experimental seeding and culturing parameters. Furthermore, whereas in the native cell microenvironment the total amount of extracellular fluid volume is proportioned to cells volume, thus facilitating diffusion of nutrients and soluble factors and depletion of wastes, in traditional culture systems cells are immersed in large culture medium baths, changed at fixed time points before depletion. This leads to the necessity of overcharging medium with abnormally high concentrations of nutrients and soluble factors for ensuring a sufficient supply to cells. The non-physiological ratio between cell volume and medium volume, together with the usually static culture approach, also favors the generation of uncontrolled chemical gradients within samples, providing cells with a low control over the biochemical environment. Traditional cell culture approaches thus represent simplified models poorly able to recapitulate the complexity found *in vivo*, lacking in probing the combined role of different factors on specific cellular responses and subjecting cells to non-physiological culture environments, ultimately featuring inappropriate size-scales.

In the past few decades, several attempts have been made to address some of these issues proposing macroscale 3D culture models, relying on innovative biomaterials, often combined with laboratory-scale bioreactors [11]. These approaches attempt to control the 3D cell organization through the exploitation of scaffolds, designed to mimic specific characteristics of the native ECM and to provide local and long-range order for tissue development and function [12]. Many advances have been made in this direction in defining innovative biomimetic material formulations, either natural [13] or synthetic [14-17], and

strategies for processing them into a wide range of 3D architectures, better mimicking the structure of native tissues [18,19]. Furthermore, the combination of biomimetic scaffolds and bioreactor culture systems recently yielded promising results in engineering functional bioconstructs [20,21]. Bioreactors indeed enable a better control over culture environmental conditions (such as exchange of oxygen, nutrients and metabolites, delivery of biochemical regulatory factors) and offer the possibility to integrate *ad hoc* physical stimulations (*i.e.* hydrodynamic shear, mechanical compression or stretch, electrical gradients) [22,23]. Although providing a more reproducible and controlled strategy to investigate mechanisms of cell behavior within a 3D environment and to engineer functional constructs, these macroscale approaches still have to deal with size-scales that are orders of magnitude bigger than the native microenvironment, thus lacking in accurately controlling biological phenomena at a cellular level. Moreover, these approaches are usually limited by a tradeoff between the necessity of modeling the concurrent effect of multiple factors and, on the other hand, the requirement for simplifying the experimental setups for ensuring statistically significant results in a reasonable amount of time. Model accuracy is thus often sacrificed for higher throughput, or *vice versa*.

In this regards, application of microscale technologies to cell biology studies recently gave huge promises for simultaneously improving model accuracy and experimental throughput [24]. Indeed, they enable an unprecedented control over the cellular microenvironment, while reducing the time and the scale of experimental platforms for better matching the cellular level [25]. Moreover, they allow for easily testing many environmental factors simultaneously, miniaturizing assays for high-throughput applications [26]. Among them, microfluidic platforms have recently demonstrated great potentialities for defining *in vitro* models able to better recapitulate the complexity of cellular microenvironment.

1.3 Microfluidics as innovative tool for modelling the role of microenvironment signaling on cell fate

Microfluidics is defined as a set of technologies enabling for the controlled manipulation of small amounts (10^{-9} to 10^{-18} liters) of fluids, molecules and particles within artificially fabricated microsystems, using channels featuring dimensions from tens to hundreds of microns [27]. The control over fluid and particles flow is achieved through the integration of 3D microstructured geometries (e.g. channels, chambers, membranes) into microdevices, fabricated by means of molding or embossing techniques [28]. Soft lithography, first introduced by the Whiteside's group in the late 1990s [28], has been demonstrated to be one of the most robust strategy for microdevices fabrications, exploiting microstructured molds obtained through photolithography to produce polymer-based microchips by replica molding. Among others, the most popular material used in soft lithography for microfluidic applications is poly(dimethyl-siloxane) (PDMS). PDMS is an elastomeric rubber with particularly interesting properties, which make it ideal for rapid design, mold and fabrication of microfluidic systems featuring a wide range of geometries or for transferring micropatterns with high fidelity *via* micro-contact printing techniques [29]. Indeed, PDMS is cheap and easy to prototype, and allows for replicating features at sub-micrometric resolution; moreover, its chemical structure, characterized by inorganic siloxane backbone and organic methyl groups attached to silicon, confers to PDMS a unique combination of chemical and physical properties [30]. First, the PDMS's low glass transition temperature makes it fluid at room temperature, while increasing the temperature it can be readily converted into a solid elastomer by cross-linking in the presence of a curing agent (usually used in a ratio of 1:10 with the liquid silicon rubber base). While typically hydrophobic, it is possible to extended its range of applications by modifying the surface properties of PDMS and introducing reactive groups [31,32]. PDMS is then particularly suitable for cell culture studies, exhibiting high biocompatibility, gas permeability, low auto-fluorescence and optical transparency in a range of wavelengths comprised between 240nm and 1100nm, thus compatible with *on chip* imaging [33]. Moreover, its elastomeric nature allows it to readily deform if subjected to local displacement, thus being suitable for the integration of valves and pumping systems directly within the devices [34]. Finally, PDMS can be reversibly or irreversibly bonded to several substrates (*e.g.* PDMS, glass, polystyrene), aiming at

enclosing microchannels, by means of different strategies such as oxygen plasma treatment [35], partial thermal curing [36] or PDMS "stamp and stick"-based techniques [37,38].

Other than material-related properties, miniaturization has also advantages in terms of low cells and samples volume requirements and in the ability to scale the environment down to the cell size level. Moreover, the surface-to-volume ratio is highly increased at this length scale. This leads to maximize the available interface for mass and energy transfer phenomena, thus enhancing reactions efficiency, while reducing their time. This is of particular interest for the performance of biochemical and biological assays *on chip (i.e.* protein analyses [39], DNA amplifications and sequencing [40]), reducing measurement times, improving sensitivity, selectivity and reproducibility [41,42]. Furthermore, in contrast with traditional cell culture systems, which rely on excess amounts of nutrients and soluble factors in culture media, microfluidic platforms can be designed for culturing cells under continuous perfusion of medium through channels and chambers. This enables for creating more physiological culture environments by keeping nutrients and media factors constant through continuous supply of fresh media and removal of waste products. The intrinsic laminarity of the flow, characteristics of the micrometer scale, also leads to simplified and highly predictable fluid, mass and energy transport phenomena, which in turn allow an unprecedented control over the local environmental conditions, including temperature, pH, dissolved gas concentration, shear stress, and medium exchange rates, at length scales finally applicable to cellular microenvironments. The ability to predict and control fluid dynamics within microchannels also allows for precisely guiding the spatial positioning of soluble factors within microchannels, thus creating controlled chemical gradients, difficult to achieve within macroscopic cell culture models [43]. This fluidic peculiarity has been extensively exploited in cell culture applications for generating linear or complex soluble gradients by sequential merging, mixing and splitting two or more solutions, containing different biochemical stimuli [44-48]. Moreover, the same principle has been extended to the generation of patterns of solid cues, with the aim to obtain microenvironments exhibiting concentration gradients of immobilized adhesive molecules or featuring variable mechanical properties/chemical composition across the material [49,50]. These approaches enabled a substantially higher control and predictability in investigating the spatio-temporal dynamics of cells interaction with different combinations/concentrations of soluble and solid factors. Another remarkable advantage of culturing cells within microscaled platform is the

capability to bring the cell population down to few hundreds or even single cells, thus enabling for increasing the spatial and temporal resolution for a given experimental setup potentially at single cell level [51].

In conclusion, microfluidic technologies constitute an innovative approach for precisely *in vitro* tailoring the cell microenvironment, automating and parallelizing experimentations and coupling cell cultures directly with high-throughput analysis systems. Microfluidic platforms thus represent promising *in vitro* models that are increasingly exploited as enabling tools in the field of cell biology, from the performance of drugs or molecules screening experiments, to the optimization of culture conditions for inducing specific cell fates.

1.4 Motivation and outline of the thesis

In the last decade, microscale technologies have introduced invaluable benefits and advanced approaches for *in vitro* culturing cells within more physiologically inspired microenvironments. In this scenario, this PhD project envisions the exploitation of the main principles of microfluidics for the generation of innovative technological solutions for addressing specific questions in the field of cell biology. The aim of this research is thus the development of microfluidic platforms and techniques as tools for investigating and modeling the effect of different cues from the cellular microenvironment in addressing stem cell fate. In details, four microscale platforms and/or techniques, *ad hoc* conceived in the context of national and international collaborations, are presented in the following chapters. Each chapter is focused on a single platform and underlines how a specific microfluidic strategy has been applied to the definition of a technological solution for addressing a specific biological goal.

In Chapter 2, the development of a microfluidic platform is addressed to (i) generate and culture 3D cellular microaggregates under continuous flow perfusion while (ii) conditioning them with different combinations/concentrations of soluble factors. An exploitation of the platform is then proposed, in collaboration with the Tissue Engineering Laboratory (University Hospital of Basel, Switzerland), to perform studies on limb bud development and investigate processes involved in mesenchymal progenitor cells differentiation, towards a 'developmental engineering' approach for skeletal tissue regeneration.

In Chapter 3, a microscale strategy is introduced to spatially tailor the 3D microenvironment around cells, based on the combination of an innovative biocompatible photopolymerizable hydrogel (VA-086-GelMA) and an easy to handle photo-mold-patterning (PMP) technique. The work presented in this chapter is partially the result of a collaboration with the Cell and Tissue Engineering Laboratory (IRCCS Galeazzi Orthopedic Institute, Milano, Italy).

In Chapter 4, a microfluidic cell mixer is presented, as the result of a collaboration with the Tissue Engineering and Microfluidics Laboratory (TEaM, University of Queensland, Australia). The integration of this mixer as upstream functional element within

two different microfluidic platforms is then demonstrated for the automatic establishment of 2D and 3D osteogenic co-culture models, aiming at investigating the influence of pre-osteoblastic cells on human mesenchymal stromal cell osteogenic commitment.

In Chapter 5, a microfluidic platform is introduced for (i) trapping and culturing single cells into defined spatial configurations, (ii) while automatically delivering them concentration patterns of non-diffusive particles (i.e. gene vectors). An exploitation of the platform is then proposed to perform *on chip* high-throughput screening and optimization of transfection strategies, in the context of a collaboration with the Biocompatibility and Cell culture Laboratory (BioCell, Politecnico di Milano, Italy).

In the last Chapter, a general discussion of the PhD dissertation and conclusive remarks are presented.

References

1. Young EWK, Beebe DJ. *Fundamentals of microfluidic cell culture in controlled microenvironments.* Chemical Society Reviews 2010;39(3):1036-1048.
2. Taga T, Kishimoto T. *Cytokine receptors and signal transduction.* The FASEB Journal 1992;6(15):3387-96.
3. Alberts B, Johnson A, Lewis J, Raff M, Roberts K, Walter P. *Intracellular compartments and protein sorting.* 2002.
4. Alberts B, Johnson A, Lewis J, Raff M, Roberts K, Walter P. *Cell communication.* 2002.
5. Keung AJ, Kumar S, Schaffer DV. *Presentation Counts: Microenvironmental Regulation of Stem Cells by Biophysical and Material Cues.* Annual Review of Cell and Developmental Biology 2010;26(1):533-556.
6. Janmey PA, McCulloch CA. *Cell Mechanics: Integrating Cell Responses to Mechanical Stimuli.* Annual Review of Biomedical Engineering 2007;9(1):1-34.
7. Takeichi M. *Cadherin cell adhesion receptors as a morphogenetic regulator.* Science 1991;251(5000):1451-1455.
8. Gumbiner BM. *Regulation of cadherin-mediated adhesion in morphogenesis.* Nat Rev Mol Cell Biol 2005;6(8):622-634.
9. Sant S, Hancock MJ, Donnelly JP, Iyer D, Khademhosseini A. *Biomimetic gradient hydrogels for tissue engineering.* The Canadian Journal of Chemical Engineering 2010;88(6):899-911.
10. Discher DE, Mooney DJ, Zandstra PW. *Growth Factors, Matrices, and Forces Combine and Control Stem Cells.* Science 2009;324(5935):1673-1677.
11. Vunjak-Novakovic G. *Biomimetic Platforms for Tissue Engineering.* Israel Journal of Chemistry 2013;53(9-10):767-776.
12. Griffith LG, Swartz MA. *Capturing complex 3D tissue physiology in vitro.* Nat. Rev. Mol. Cell Biol. 2006;7(3):211-224.
13. Badylak SF. *The extracellular matrix as a biologic scaffold material.* Biomaterials 2007;28(25):3587-3593.
14. Zhao X, Kim J, Cezar CA, Huebsch N, Lee K, Bouhadir K, Mooney DJ. *Active scaffolds for on-demand drug and cell delivery.* Proceedings of the National Academy of Sciences 2011;108(1):67-72.
15. Shakesheff KM, Cannizzaro SM, Langer R. *Creating biomimetic micro-environments with synthetic polymer-peptide hybrid molecules.* Journal of Biomaterials Science, Polymer Edition 1998;9(5):507-518.
16. Lutolf MP, Raeber GP, Zisch AH, Tirelli N, Hubbell JA. *Cell-Responsive Synthetic Hydrogels.* Advanced Materials 2003;15(11):888-892.
17. Lim HL, Hwang Y, Kar M, Varghese S. *Smart hydrogels as functional biomimetic systems.* Biomaterials Science 2014;2(5):603-618.
18. Guilak F, Cohen DM, Estes BT, Gimble JM, Liedtke W, Chen CS. *Control of Stem Cell Fate by Physical Interactions with the Extracellular Matrix.* Cell Stem Cell 2009;5(1):17-26.
19. Assaf S, Deok-Ho K, Tal D. *Advanced micro- and nanofabrication technologies for tissue engineering.* Biofabrication 2014;6(2):020301.
20. Martin I, Wendt D, Heberer M. *The role of bioreactors in tissue engineering.* Trends in Biotechnology 2004;22(2):80-86.
21. Hansmann J, Groeber F, Kahlig A, Kleinhans C, Walles H. *Bioreactors in tissue engineering—principles, applications and commercial constraints.* Biotechnology Journal 2013;8(3):298-307.

22. Jin G, Yang GH, Kim G. *Tissue engineering bioreactor systems for applying physical and electrical stimulations to cells.* Journal of Biomedical Materials Research Part B: Applied Biomaterials 2014.
23. Martin I, Riboldi S, Wendt D. *Bioreactor Systems in Regenerative Medicine.* In: Shastri VP, Altankov G, Lendlein A, editors. Advances in Regenerative Medicine: Role of Nanotechnology, and Engineering Principles: Springer Netherlands; 2010. p 95-113.
24. Ranga A, Lutolf MP. *High-throughput approaches for the analysis of extrinsic regulators of stem cell fate.* Current opinion in cell biology 2012;24(2):236-244.
25. Ranga A, Gobaa S, Okawa Y, Mosiewicz K, Negro A, Lutolf MP. *3D niche microarrays for systems-level analyses of cell fate.* Nat Commun 2014;5.
26. Khademhosseini A, Langer R, Borenstein J, Vacanti JP. *Microscale technologies for tissue engineering and biology.* Proceedings of the National Academy of Sciences of the United States of America 2006;103(8):2480-2487.
27. Whitesides GM. *The origins and the future of microfluidics.* Nature 2006;442(7101):368-373.
28. Xia YN, Whitesides GM. *Soft lithography.* Annual Review of Materials Science 1998;28:153-184.
29. Bernard A, Renault JP, Michel B, Bosshard HR, Delamarche E. *Microcontact printing of proteins.* Advanced Materials 2000;12(14):1067-1070.
30. Tang SK, Whitesides GM. *Basic microfluidic and soft lithographic techniques.* Optofluidics: Fundamentals, Devices and Applications, McGraw-Hill Professional 2009:7-31.
31. Zhou J, Ellis AV, Voelcker NH. *Recent developments in PDMS surface modification for microfluidic devices.* Electrophoresis 2010;31(1):2-16.
32. Wong I, Ho C-M. *Surface molecular property modifications for poly (dimethylsiloxane)(PDMS) based microfluidic devices.* Microfluidics and nanofluidics 2009;7(3):291-306.
33. McDonald JC, Whitesides GM. *Poly(dimethylsiloxane) as a material for fabricating microfluidic devices.* Accounts of Chemical Research 2002;35(7):491-499.
34. Unger MA, Chou H-P, Thorsen T, Scherer A, Quake SR. *Monolithic Microfabricated Valves and Pumps by Multilayer Soft Lithography.* Science 2000;288(5463):113-116.
35. McDonald JC, Duffy DC, Anderson JR, Chiu DT, Wu HK, Schueller OJA, Whitesides GM. *Fabrication of microfluidic systems in poly(dimethylsiloxane).* Electrophoresis 2000;21(1):27-40.
36. Stroock AD, Whitesides GM. *Components for integrated poly (dimethylsiloxane) microfluidic systems.* Electrophoresis 2002;23(20):3461-73.
37. Mark AE, Michael AJ, Bruce KG. *Determining the optimal PDMS–PDMS bonding technique for microfluidic devices.* Journal of Micromechanics and Microengineering 2008;18(6):067001.
38. Satyanarayana S, Karnik RN, Majumdar A. *Stamp-and-stick room-temperature bonding technique for microdevices.* Microelectromechanical Systems, Journal of 2005;14(2):392-399.
39. Lion N, Reymond F, Girault HH, Rossier JS. *Why the move to microfluidics for protein analysis?* Current Opinion in Biotechnology 2004;15(1):31-37.
40. Zhang Y, Ozdemir P. *Microfluidic DNA amplification—A review.* Analytica Chimica Acta 2009;638(2):115-125.
41. Weibel DB, Whitesides GM. *Applications of microfluidics in chemical biology.* Current Opinion in Chemical Biology 2006;10(6):584-591.
42. Hansen C, Quake SR. *Microfluidics in structural biology: smaller, faster… better.* Current Opinion in Structural Biology 2003;13(5):538-544.

43. Stone HA, Stroock AD, Ajdari A. *Engineering flows in small devices.* Annual Review of Fluid Mechanics 2004;36(1):381-411.
44. Titmarsh D, Cooper‐White J. *Microbioreactor array for full-factorial analysis of provision of multiple soluble factors in cellular microenvironments.* Biotechnology and Bioengineering 2009;104(6):1240-1244.
45. Jeon NL, Baskaran H, Dertinger SKW, Whitesides GM, Van de Water L, Toner M. *Neutrophil chemotaxis in linear and complex gradients of interleukin-8 formed in a microfabricated device.* Nature Biotechnology 2002;20(8):826-830.
46. Lee K, Kim C, Ahn B, Panchapakesan R, Full AR, Nordee L, Kang JY, Oh KW. *Generalized serial dilution module for monotonic and arbitrary microfluidic gradient generators.* Lab on a Chip 2009;9(5):709-717.
47. Sahai R, Martino C, Castrataro P, Menciassi A, Ferrari A, Beltram F, Cecchini M. *Microfluidic chip with temporal and spatial concentration generation capabilities for biological applications.* Microelectron. Eng. 2011;88(8):1689-1692.
48. Kim C, Lee K, Kim JH, Shin KS, Lee K-J, Kim TS, Kang JY. *A serial dilution microfluidic device using a ladder network generating logarithmic or linear concentrations.* Lab on a Chip 2008;8(3):473-479.
49. He J, Du Y, Guo Y, Hancock MJ, Wang B, Shin H, Wu J, Li D, Khademhosseini A. *Microfluidic synthesis of composite cross-gradient materials for investigating cell–biomaterial interactions.* Biotechnology and Bioengineering 2011;108(1):175-185.
50. Burdick JA, Khademhosseini A, Langer R. *Fabrication of Gradient Hydrogels Using a Microfluidics/Photopolymerization Process.* Langmuir 2004;20(13):5153-5156.
51. Avesar J, Arye TB, Levenberg S. *Frontier microfluidic techniques for short and long-term single cell analysis.* Lab on a Chip 2014.

2

High-Throughput Microfluidic Platform for 3D Cultures of Mesenchymal Stem Cells, Towards Engineering Developmental Processes

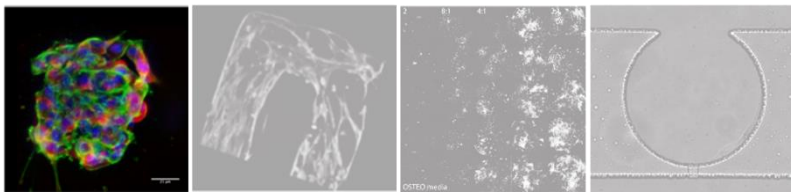

The work described in this chapter was partially carried out at the *Tissue Engineering Laboratory*, University Hospital of Basel, Basel, Switzerland

This chapter partially refers to:

High-Throughput Microfluidic Platform for 3D Cultures of Mesenchymal Stem Cells, Towards Engineering Developmental Processes. Occhetta P, Centola M, Tonnarelli B, Redaelli A, Martin I, Rasponi M, Scientific Reports (Under review)

Rationale

The design of strategies for generating physiologically relevant *in vitro* models of "proto-tissues", directly integrating high-throughput and automatic screening capabilities, could find great applicability in several applications of cell biology. In particular, research fields such as tissue morphogenesis, developmental biology and cancer biology, which mainly rely on the capability of cells to re-organize themselves, forming patterns on their own, could highly benefit from systems able to favor the spontaneous cell aggregation into controlled-sized cellular micromasses.

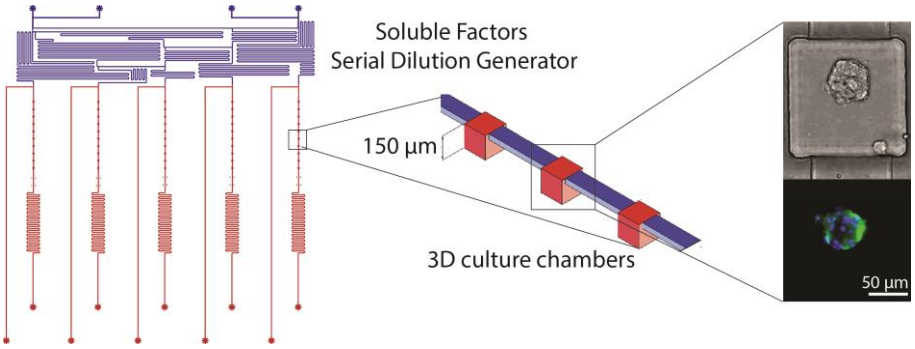

A microfluidic platform was introduced for 3D cellular micromasses generation and culturing under spatially defined patterns of soluble factors.

Moreover, *in vitro* models to screen the effect of different concentrations, combinations and temporal sequences of morpho-regulatory factors on stem/progenitor cells represent enabling tools to investigate and possibly recapitulate developmental processes for tissue engineering applications.

In this perspective, the platform presented in this chapter was here exploited to perform studies on limb bud development - in collaboration with the Tissue Engineering Laboratory (University Hospital of Basel, Switzerland) - with the aim to investigate processes involved in mesenchymal progenitor cells differentiation, towards a 'developmental engineering' approach for skeletal tissue regeneration. More in detail, this chapter addresses the development of a microfluidic platform to (i) generate and culture 3D cellular microaggregates under continuous flow perfusion while (ii) conditioning them with different combinations/concentrations of soluble factors (*i.e.* growth factors, morphogens or drug molecules), in a high-throughput fashion.

2.1 Introduction

The *in vitro* recapitulation of key mechanisms involved in embryonic organogenesis is increasingly being recognized of great importance in the field of Tissue Engineering (TE) [1] and more in general of regenerative medicine [2,3]. Several techniques for regenerating functional tissues have indeed found inspiration from developmental biology paradigms [4], giving rise to the "so-called" field of developmental engineering [5]. This approach consists in faithfully recapitulating *in vitro* the temporal sequence of events occurring in the developing embryo and it has been successfully applied in the context of skeletal TE, leading to significant results in terms of endochondral bone formation using both embryonic stem cells [6] and a more clinically relevant cell source, such as human adult bone marrow-derived mesenchymal stem/stromal cells (hBM-MSC) [7,8]. Although suffering from an overall heterogeneity in cell responses, these latter approaches have been recently employed for *in vitro* recapitulating early stages of limb development [9] - namely cell condensation, undifferentiated proliferation of a mesenchymal cell population and pre-chondrogenesis [10]. Developmental biology models suggest how these steps are tightly regulated by the interplay of specific signaling pathways – namely, Wnt/β-catenin, FGF and TGFβ/BMP – defining complex and spatio-temporally dynamic gradients [11]. In detail, the proper activation of Wnt-canonical and FGF pathways initially promotes the expansion of an undifferentiated pool of limb progenitors, which subsequently are capable to undergo chondrogenesis under the influence of members of the TGFβ/BMP superfamily [12,13]. Several studies have been made in the attempt of elucidating the role of such pathways on hBM-MSC fate, mainly using 2D cell cultures and, only recently, more relevant 3D models, consisting in culturing cell macropellets [14-16]. However, these 3D approaches still suffer from an overall heterogeneity in cell responses and a consistently low proliferation rate [17]. Main reasons for their inadequacy are (i) the non-physiological forced initial cell condensation in macropellets, (ii) the presence of necrotic cores within aggregates due to the excessive number of cells (typically ranging from tens to hundreds thousands cells), (iii) the suboptimal culture conditions (i.e., the poor control over morphogen delivery), and (iv) the formation of chemical gradients within the volume of samples due to diffusion limitations. More effective and reliable i*n vitro* models are thus required for investigating the response of mesenchymal cell systems to external morphoregulatory stimuli.

Microfluidics has been increasingly applied for generating high-throughput cell culture models, featuring unprecedented spatio-temporal control over microenvironmental conditions [18]. The establishment of a highly controlled continuous perfusion of culture medium within microchannels has indeed been demonstrated to maintain more uniform and controlled culture conditions than traditional static approaches, providing constant convective dilution of catabolites and stable supply of nutrients and morphogens stimulatory factors [18,19]. Moreover, the ability to handle cells and fluids in precise spatial configurations allows to precisely tailor the microenvironment around cells, potentially achieving spatio-temporally controlled delivery of morphogens combinations [20]. Several microfluidic devices able to establish high-throughput 2D cell culture features were developed, either within research laboratories [21-24] or as commercial platforms (e.g. CellASIC™ ONIX Platform, Millipore). However, the control over the third dimension still remains poorly explored due to the challenge of combining microfabrication techniques to the size-scale of 3D micro-tissues. While promising results have been achieved generating cellular microaggregates through conventional systems (i.e. microwells) and subsequently trapping them within microfluidic channels [25-27], the ability to combine generation, culture under continuous perfusion, and analyses of micro-tissues within a single microfluidic device, has only been achieved by means of self-aggregating embryoid bodies (EBs), and in a low-throughput manner [28,29].

In this study, we combined the advantages of microfluidics and 3D culture systems in the attempt of developing a physiological *in vitro* model of limb development. To this aim, we reported an innovative microfluidic platform for generating and culturing 3D adult hBM-MSCs microaggregates under continuous and controlled laminar flow perfusion. The platform consists of two functional units: (i) a 3D culture area and (ii) a serial dilution generator (SDG). The culture area was specifically designed to favor the condensation of tens of mesenchymal cells within fluidically-connected microchambers located in spatially defined configurations, accomplishing the formation of microaggregates with uniform size and shape [30]. Two different SDG layouts were then implemented: the first characterized by a logarithmic configuration, thus allowing to investigate the effects of soluble factors over a wide concentration range; the second featuring a linear layout for finer tunings within narrower concentration windows.

The developed microfluidic platform was exploited to demonstrate a more uniform and repeatable response of 3D microaggregates to specific morphogens involved in limb bud development (*i.e.*, Wnt and FGF pathways), in comparison with traditional macromass pellet culture models [31]. Finally, the effect of concentration patterns of a key morphoregulatory factor (TGFβ3) on hBM-MSC 3D proliferation and differentiation was preliminary investigated in a high-throughput fashion, confirming the suitability of the platform to be further exploited as an *in vitro* model for sequentially guiding hBM-MSC towards the recapitulation of primordial steps of the endochondral route.

2.2 Microfluidic platform design and fabrication

In the following paragraphs, the design and fabrication steps of the presented microfluidic platform will be detailed.

2.2.1 Microfluidic platform for generating and culturing 3D microaggregates

Two microfluidic platforms were designed and fabricated for generating and culturing cell microaggregates under spatially controlled chemical microenvironments (Fig.2.1a). in details, two different SDG layouts were designed based on a resistive flow scheme consisting of microfluidic networks [32] for generating linear (100%, 80%, 60%, 40%, 20%, 0%) as well as logarithmic (100%, 10%, 1%, 0.1%, 0%) concentration profiles of soluble factors. The microfluidic networks were composed of thin fluidic-resistance microchannels (70 μm wide and 70 μm tall), whose lengths were dimensioned to allow diffusive mixing of soluble factors, while ensuring equal flow rates among outlets. For this purpose, flow rates up to 12 μl/h were considered for mixing chemical species featuring diffusion coefficients down to $D \sim 10^{-6}$ cm^2 sec^{-1}. Both SDGs were rather compact, occupying a footprint of about 2.5 cm^2. In order to perform correctly, the ratio between flow rates at input ports (A1 and B1 in Fig.2.1a) was computed, resulting in 1:1 for the linear configuration and 1:3.5 for the logarithmic one.

Serial dilutions are thus independently delivered to downstream culture units. Each unit (Fig.2.1a, C1-C6) comprised 10 cubic culture chambers (side of 150 μm) and was integrated with a secondary channel (Fig.2.1a, D1-D6). Chambers were dimensioned for culturing 3D microaggregates while ensuring enough space for their early expansion. Two secondary inlets (Fig.2.1a, A2-B2) were also included in the layouts to facilitate the medium change operations, defining a by-pass for the device.

2.2.2 Fabrication of the microfluidic platform

Final microfluidic layouts (Fig.2.1a) were designed through a CAD software (AutoCAD, Autodesk Inc.) and the corresponding master molds were realized through photolithography techniques [33]. A thin microfluidic layer (thickness 1mm) was obtained by replica molding of PDMS (Sylgard® Dow Corning, Michigan, USA). Briefly, liquid PDMS was cast on the mold in ratio 10:1 w/w (pre-polymer to curing agent), degassed and cured at 80°C for 3 h. The obtained PDMS microstructured layer was permanently bonded facing up

to a flat PDMS slab (thickness 5mm), upon 1 min of air plasma treatment (Harrick Plasma, NY, USA), thus closing the channels. Input and output ports were obtained through a 0.5mm biopsy puncher (Harris Uni-CoreTM). The chip was finally permanently bonded to a glass coverslide (diameter 50mm, thickness 150µm; VWR International Inc., PA, USA) upon an additional 1 min exposure to air plasma (Fig.2.1b). External connections were realized through tygon tubing (ID = 0,02"; Qosina, NY, USA) and stainless steel couplers (23 gauge; Instech Laboratories Inc., PA, USA).

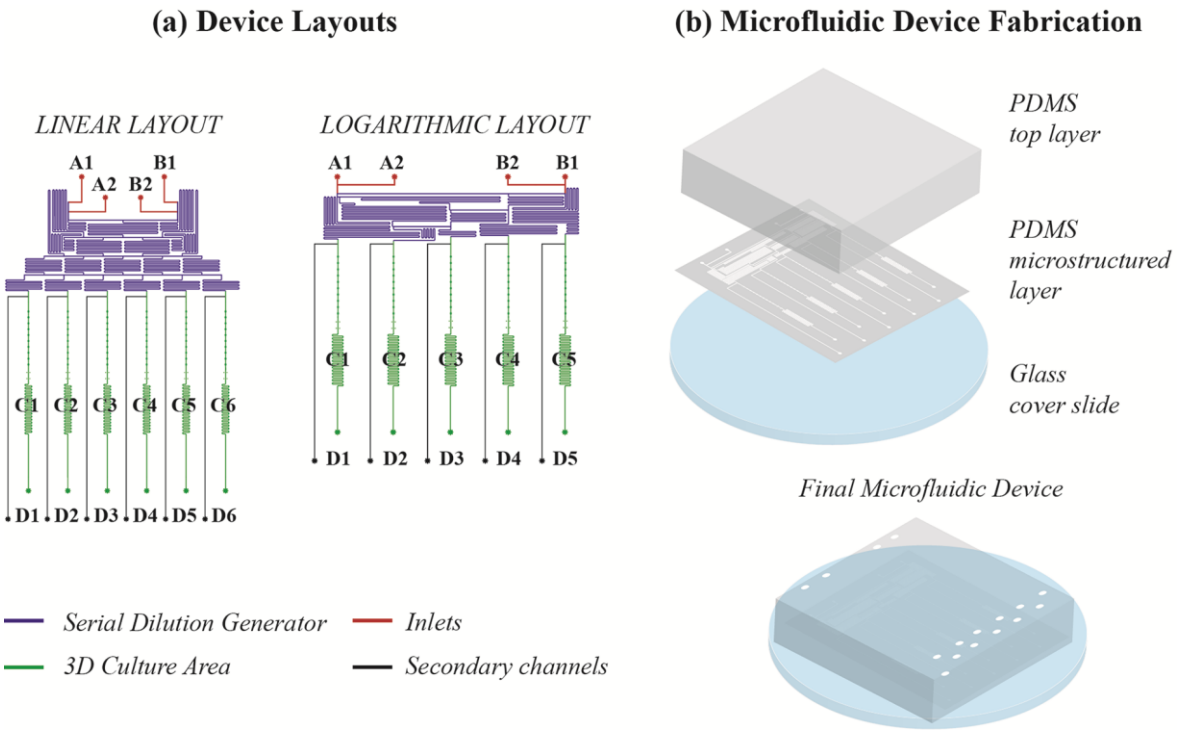

Figure 2.1. *Microfluidic device layouts (a) and fabrication process (b). The chip layouts consisted of a serial dilution generator – either featuring a linear or a logarithmic configuration - and a 3D culture area (a). Dilutions of chemicals were generated from two main inlets (A1-B1) and delivered to downstream culture units (C1-C6); furthermore, each unit was provided with a secondary channel (D1-D6). Two additional inlets (A2-B2) facilitated the medium change operations, defining a by-pass for the device. The final device was fabricated with PDMS following standard soft-lithography techniques. First, the PDMS microstructured layer was bonded facing up to a PDMS top layer; then the device was bonded on a glass cover slide (b).*

2.3 Functional characterization of the serial dilution generator (SDG)

In this paragraph, linear and logarithmic SDGs experimentally characterization is described, in terms of distribution of flow rates and generation of designed chemical concentration patterns at the outlets.

First, flow rate distributions generated by both SDG configurations was assessed to verify the correct partitioning of the inflow among culture units. Tygon tubings were connected at the output ports and an overall flow rate of 24µl/h for the linear SDG and 45µl/h for the logarithmic one was imposed through the inlets. The outflow from each outlet was quantified by measuring the travel length of each meniscus within the tubing and obtained flow rates resulted rather uniformly distributed among the outlets in both SDG configurations. In the linear version, a maximum variation of 3% from the expected value (4 µl/h *per* unit) was detected. Similarly, in the logarithmic configuration, imposing a total inflow of 45 µl/h, a maximum variation of 5% from the expected value (9 µl/h *per* line) was obtained.

Quantitative evaluations of chemical patterns generated by SDGs were then performed, using two different readout approaches. For the linear configuration, two dye solutions were pumped through the main inlets at a flow rate of 10 µl/h each, as exemplified in Fig.2.2a. After the achievement of a steady state condition, samples of 20 µl (n=3) were collected from each outlet. A spectrophotometer (NanoDrop 2000c, Thermo Scientific, Wilmington, USA) was used to detect the average emission wavelength for each condition. The six dilutions collected from the outlets matched with the expected linear distribution (R^2=0.9891) (Fig.2.2b).

For the logarithmic SDG a more sensitive readout was required, being the output dilutions widespread over four orders of magnitude. In details, a solution of 20 mg/ml bovine serum albumin (BSA, Sigma, Buchs SG, Switzerland) in dH_2O was pumped into the right inlet (A1) at a flow rate of 10 µl/h while dH_2O was pumped into the left one (B1) at 35 µl/h. After the achievement of a steady state condition, samples of protein dilutions were collected from each outlet (n=3) and the BSA concentration was measured by means of a BCA Protein Assay kit (Pierce, Thermo Fisher Scientific, Reinach, Switzerland), following the manufacturer's indications. The BSA concentration of the five dilutions collected from the output ports were measured to range over four orders of magnitude (1, 0.1, 0.01, 0.001 and

0, as negative control), matching the expected logarithmic distribution (R^2=0.9908) (Fig.2.2c).

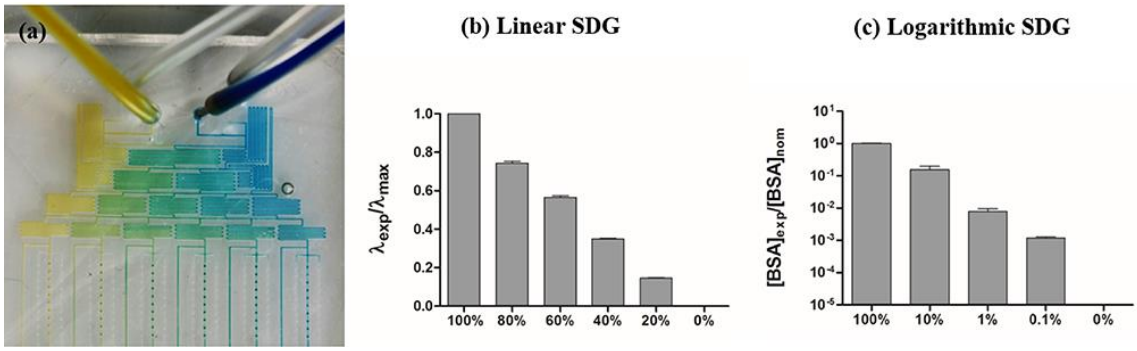

Figure 2.2. *Characterization of serial dilution generators (SDGs). The linear device was perfused with dye solutions and, after reaching the steady state, a linear color pattern was visible in the SDG (a). The quantitative measurement of the emission wavelengths of the 6-outlet solutions (normalized for the λmax) resulted in a linear trend (n=3) (b). The logarithmic device was characterized by perfusing 20 mg/ml BSA solution and measuring the concentration achieved after mixing within the SDG by means of a BCA assay. The quantitative measurement of the 5-outlet solutions resulted in a logarithmic trend, matching the expected concentrations (n=3) (c).*

2.4 Generation, culture and analyses of 3D hBM-MSCs micromasses within the microfluidic platform

Following paragraphs report the preliminary biological validation performed on the presented microfluidic platform. Isolation and expansion procedures of hBM-MSCs were first described (2.4.1), followed by methods for the establishment of control macroscale pellet cultures (2.4.2) and microaggregates seeding with the device (2.4.3). Assays performed within the microfluidic platform were then detailed, regarding quantification of micromasses dimensions (2.4.4), cell proliferation (2.4.5) and immunofluorescence analyses (2.4.6).

2.4.1 Adult hBM-MSCs isolation and expansion

Human mesenchymal stromal cells cultures (hBM-MSCs) were established as previously described [34]. hBM-MSCs were expanded in alpha-MEM containing 10% fetal bovine serum (FBS), 4.5 mg/ml D-glucose, 0.1 mM nonessential amino acids, 1 mM sodium pyruvate, 100 mM HEPES buffer, 100 Ul/ml penicillin, 100 µg/ml streptomycin, and 0.29 mg/ml L-glutamate, further supplemented with 5 ng/ml FGF2 (Fibroblast Growth Factor2; R&D Systems, Minneapolis, MN, USA). Medium was changed twice a week and hBM-MSCs were used between P1 and P3 for the experiments.

2.4.2 Establishment of macroscale pellet cultures

Macromass pellets were established and used as control. In details, aliquots of 2.5 x 10^5 cells/0.25 ml hBM-MSC were centrifuged at 1,100 rpm for 5 min to form pellets. Pellets were cultured under static conditions up to one week in serum free medium (SFM), consisting of DMEM with 1 mM sodium pyruvate, 100 mM HEPES buffer, 100 UI/ml penicillin, 100 µg/ml streptomycin, 0.29 mg/ml L-glutamate, 0.1 mM ascorbic acid 2-phospate (Sigma), ITS+1 (Sigma, 10 µg/ml insulin, 5.5 µg/ml transferrin, 5 ng/ml selenium), 5 µg/ml human serum albumin, and 4.7 µg/ml linoleic acid further enriched with 1 ng/ml TGFβ3 and medium was changed twice a week.

2.4.3 Microaggregates generation and culture within the microfluidic device

Before cell seeding, microfluidic devices were sterilized by autoclaving (121°C, 20 min, wet cycle) and dried overnight at 80°C to recover PDMS hydrophobicity and minimize

cell adhesion in the chambers during the seeding. Devices were then submerged in sterile PBS and degassed [35]. Subsequently, SFM was perfused through the main inlets of the device (Fig.1a, A1 and B1).

After expansion hBM-MSCs were detached, diluted to the concentration of 10^7 cells/mL in SFM (not to bias the cell condensation), and seeded into the culture units by perfusing 0.1 µl/min of cell suspension from all outlets (C1-C6), while maintaining an opposite mild medium flow (0.5 µl/min) from each inlet (A1-B1). The secondary channels (D1-D6) were used as waste during the seeding procedure to avoid cell clogging in the upstream channels, while they were clamped during the culture period. Once culture chambers were filled with hBM-MSCs, a continuous flow rate of 5 µl/h *per* line was applied and maintained throughout the entire experiment, while the microfluidic platform was incubated under standard culture conditions (T=37°C, 5% CO_2 and humidified atmosphere). Phase contrast images of hBM-MSCs seeded into the microchambers were acquired every 15 minutes during the first 4 hours of culture to monitor the microaggregates condensation.

Microaggregates were cultured up to seven days under continuous perfusion of different conditioning media. In details, SFM was enriched either with 1 ng/ml TGFβ3 or with a combination of 20 ng/ml rhWnt3a (wingless-type MMTV integration site family member3a; R&D) and 5 ng/ml FGF2.

2.4.4 Correlation between microaggregates diameter and cell number

A previously implemented algorithm [36] for determining the number of chondrocytes in an aggregate starting from its two-dimensional macroscopic profile was applied to our model. Briefly, the algorithm correlates the diameter of an aggregate with the corresponding cell number by means of a sphere packing theory. Fig.1.3 shows the theoretical relationship between diameter and cell number, having upper and lower bounds.

Experimental results obtained through our microfluidic approach were compared to the algorithm in order to determine the degree of matching. In details, hBM-MSC microaggregates were formed within the platform and after 3 hours live phase contrast images were acquired by means of a Olympus BX-61 microscope (Olympus, Tokyo, Japan). The diameter of each microaggregate was calculated as the average of two measurements. Microaggregates were subsequently fixed in 4% paraformaldehyde (PFA) and immunofluorescence stained for Dapi as described below. Confocal Z-stack images of the immunofluorescence microaggregates were acquired by means of a Nikon A1R Nala

Confocal microscope. The number of cells was then calculated through the ImageJ software (NIH, http://imagej.nih.gov).

The experimental results obtained with hBM-MSCs microaggregates were shown to match with the theoretical model (Fig.2.3, R^2=0.9565). The model was thus used during experiments for estimating the number of cells starting from the measurement of microaggregates diameter.

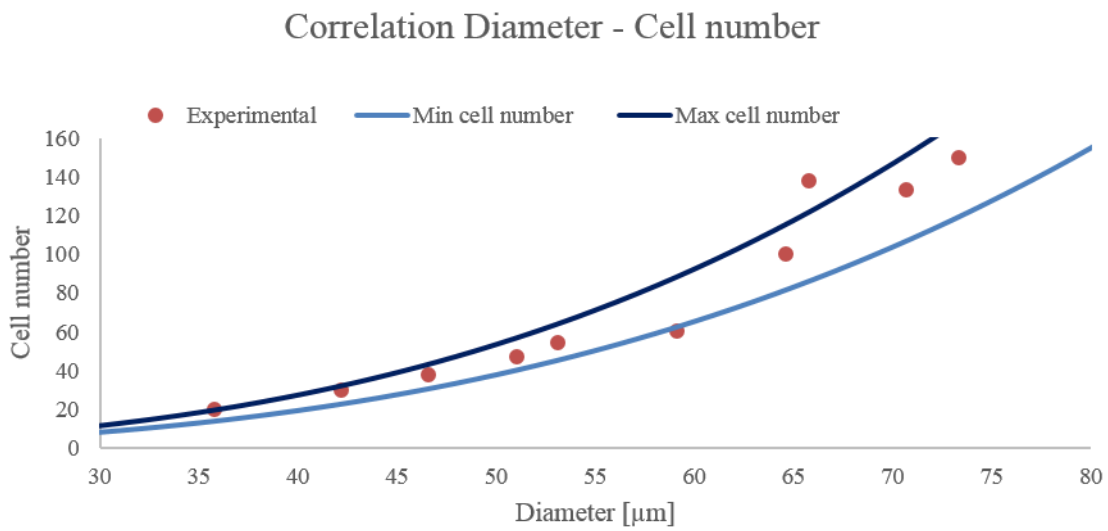

Figure 2.3. *Validation of a previously implemented algorithm (Martin et al., 1997) for correlating diameter and cell number in the proposed hBM-MSCs microaggregates model. The theoretical relationship between diameter and cell number were plot and compared to the experimental data.*

2.4.5 3D cell proliferation assays

The number of hBM-MSCs in the S-phase of the cell cycle was quantified through a 5-ethynyl-2'-deoxyuridine (Edu)-based assay (Molecular Probes, Life Technologies). Briefly, SFM enriched with 10 µM Edu was either added to the macropellet cultures or continuously perfused within the microfluidic device at specific time points (day 2 and 6). Different incubation times with Edu were tested (Fig.2.4a-c) and an exposure time of 24 hours was selected as the one giving an adequate temporal window over the cell cycle [17]. Incorporation of Edu and quantification of Edu^+ cells were determined via immunofluorescence staining, as described in the *Immunofluorescence analyses* sub-section. Negative controls were obtained by treating samples with colchicine (100 ng/ml; Invitrogen, Life Technologies) from day 0 of culture, to inhibit cell division (Fig.2.4d). Further negative controls were established by preventing cells from Edu exposure (Fig.2.4e).

Microaggregates live phase contrast images were acquired using an Olympus BX-61 (Olympus, Tokyo, Japan) and the average diameters were evaluated through the ImageJ software. The corresponding cell number was calculated in correlation with the microaggregates diameter applying an algorithm developed by Martin et al. [36] and validated for our specific samples (see paragraph 2.4.4). For macropellets, similar analyses on the diameter changes were performed, while the cell number quantification was carried out by means of a standard CyQUANT® cell proliferation assay kit (Molecular Probes, Life Technologies).

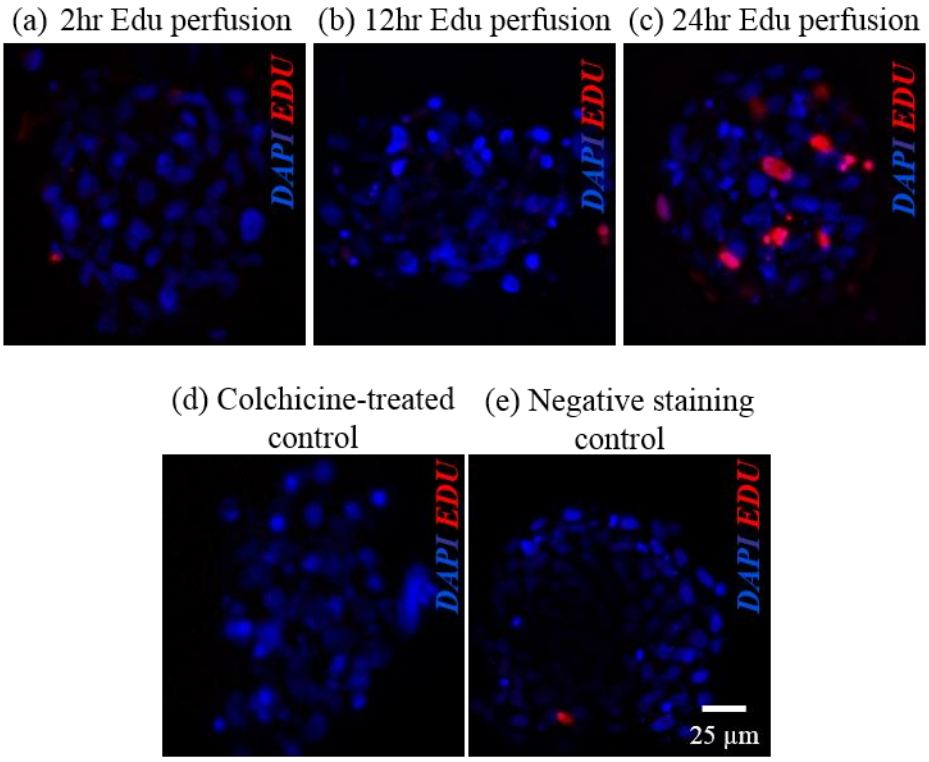

Figure 2.4. *Controls defined for Edu immunofluorescence staining. Different Edu exposure time were tested for studying the 3D proliferation of microaggregates (2hr, 12hr and 24hr) (a-c), obtaining adequate results in terms of temporal window over the cell cycle only for the 24hr exposure (c). To establish experimental negative controls, some samples were treated with colchicine to inhibit cell division (d). Negative staining controls were finally obtained preventing cells from Edu exposure (e).*

2.4.6 Immunofluorescence analyses

At specific time points, immunofluorescence analyses were performed using Dapi as counterstaining. Microaggregates were fixed by perfusing 4% PFA for 20 min and immunofluorescence stainings were obtained by sequentially perfusing the required

solutions directly within the device at constant flow rate (1 µl/min). Briefly, a solution of 3% goat serum and 0.5% Tween20 (Sigma) in PBS was perfused for 45 min to permeabilize cells and to block nonspecific bindings. Expression of vinculin and N-cadherin were detected by perfusing 10 µg/ml Mouse Anti-Vinculin (BD, Allschwil, Switzerland) and Mouse Anti-N cadherin (R&D) for 1 hour. Actin cytoskeleton was stained by further perfusing a FITC-conjugated phalloidin solution (BD) for 45 min. Cell proliferation and expression of Collagen II within microaggregates was also evaluated by perfusing 10 µg/ml of Rabbit Anti-Ki67 and 10 µg/ml of Mouse Anti-Collagen II (R&D) solutions for 1 hour. Finally, microaggregates were perfused with specific secondary antibodies (Goat Anti-Mouse IgG1 Alexa Fluor 546-conjugated for vinculin, Goat Anti-Mouse IgG1 Alexa Fluor 488-conjugated for N-cadherin and Collagen II and Goat Anti-Rabbit IgG for Ki67) for 45 min. Immunofluorescence for Edu staining was performed on both Edu-treated microaggregates and sections of macropellets by using Alexa Fluor 555-conjugated Click-iT Edu Assay kit (Molecular Probe, Life Technologies), according to the manufacturer's indications. The microaggregates staining was performed by sequentially perfusing the required solutions directly within the microfluidic platform, as described above. Instead, macropellets were fixed in 4% paraformaldehyde overnight, dehydrated, and embedded in paraffin. Five micrometers thick sections were then cut by means of a Microm HM400 microtome and the Edu staining was obtained following a standard protocol [17].

Confocal images of immunofluorescence microaggregates were acquired directly within the devices by means of a Nikon A1R Nala Confocal microscope (Nikon, Tokyo, Japan), while immunofluorescence sections of macropellets were analyzed by means of an Olympus BX-61 microscope [17]. The 3D percentage of Edu^+ cells over the total number of cells was calculated through ImageJ software (NIH).

2.5 Towards developmental engineering: recapitulation of early stages of limb development through adult hBM-MSCs within the microfluidic platform

In the next paragraphs, the exploitation of the previously optimized microfluidic platform as a tool for *in vitro* recapitulating early stages of limb development through adult hBM-MSCs is described. Obtained results are fully detailed, regarding hBM-MSCs spontaneous condensation into microaggregates (2.5.1), subsequent 3D proliferation (2.5.2) and response to specific morphogens stimulations (2.5.3), and compared with that achieved from macroscale control models. Finally, results obtained using the microfluidic platform as a high-throughput tool for screening the concentration-dependent effect of TGFβ3 on hBM-MSCs micromasses are reported (2.5.4).

2.5.1 Microaggregates condensation within the microfluidic device

Live phase contrast images of hBM-MSCs deposited into microchambers documented a progressive cell condensation occurring within three hours from the seeding (Fig.2.5a). Estimated the shear stress experienced by hBM-MSCs during this time frame negligible (lower than 10^{-3} dyne/cm^2 deriving from an imposed flow rate of 0.5μl/h), the reported cell condensation was classified as non-externally induced, leading after 24 hours to the generation of micromasses condensed into roughly spherical bodies (Fig.2.5b). At this time point, the measured diameter was (56.2±3.9) μm, implying that each aggregate occupied around 3% of the chamber volume, and consisted of an averaged cell number of 77±15, as from experimental correlation achieved through the model previously described.

Early expression of adhesion proteins and interconnections among cells were also assessed, as further proofs of the hBM-MSCs effective condensation within the microdevice. Fig.2.5c shows the expression of neural cadherin (N-cadherin) within microaggregates after 3 hours from seeding. Noteworthy, the formation of an actin cytoskeleton network as well as the expression of vinculin was also detected (Fig.2.5d), tightly interconnecting cells within microaggregates.

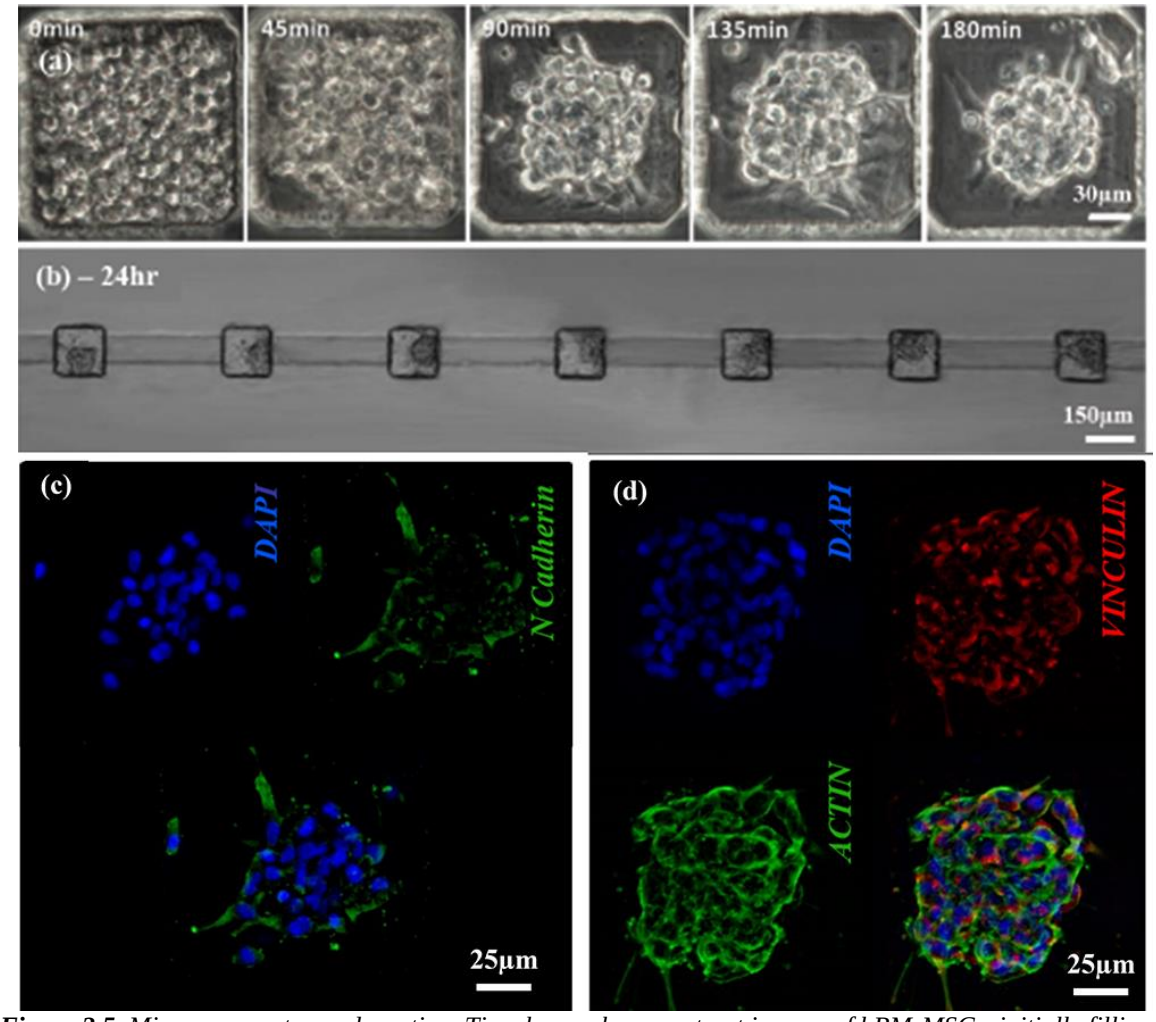

***Figure 2.5**. Microaggregate condensation. Time lapse phase contrast images of hBM-MSCs, initially filling a microchamber. Cells started to aggregate within tens of minutes while reaching a complete non-externally induced condensation after 3 hours from the seeding (a). Resulting microaggregates were cultured within the chambers initially occupying about 3% of the volume (b). Immunofluorescence images showed the expression of adhesion proteins. The achievement of a full hBM-MSCs condensation is confirmed after 3 hours from seeding by N-cadherin expression, a cell adhesion molecule involved in the initiation of cell condensation (c). Moreover, the presence of an actin cytoskeleton network was showed, tightly connecting the cells after 3 hours from seeding (d).*

2.5.2 3D cell proliferation: comparison between macroscale and microfluidic models

Cell proliferation of perfused micromasses was assessed over a period of 7 days [17] in culture upon TGFβ3 conditioning, and compared to traditional 3D macroscale cultures (macromass pellets). In particular, two parameters were monitored throughout the culture: (i) the total number of proliferative (i.e. Edu positive, Edu^{+}) cells within samples, and (ii) the variations of aggregate dimensions.

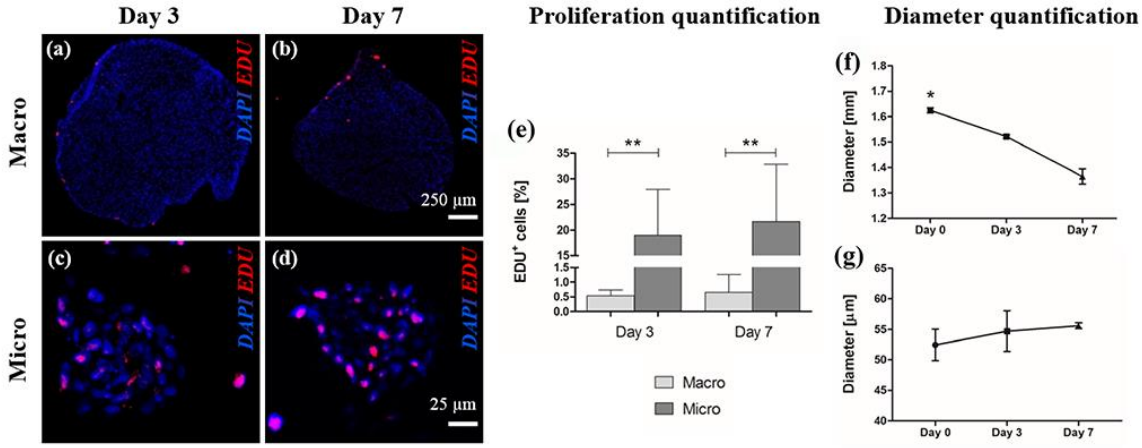

Figure 2.6. *Comparison between macroscale pellet and microfluidic models in terms of 3D cell proliferation potential. Representative Edu immunofluorescence images showed a higher and more homogeneously spatially distributed number of Edu-expressing cells within the microaggregates (c, d) than within the pellet sections (a, b), as confirmed by a statistically significant difference in the %Edu+ cells for both the considered time points (e). The assessment of the aggregates diameter over 7 days showed opposite trends: a statistically significant decrease for macroscale pellets (f) while a slight increase for the microfluidic model (g). (Macroscale: n = 3. Microscale: n=5. *p < 0.05. **p < 0.01).*

Fig.2.6a-d shows representative images of the Edu incorporation assay, acquired for both macro- and micro- scales. The macromass pellets exhibited up to 0.64±0.34% Edu^+ cells at day 7 (Fig.2.6e), while a statistically significant higher number (i.e., 21.64±11.13% at day 7, Fig.2.6e) was found within microaggregates. It is also worth noting that Edu^+ cells were mostly found along the contour of macromass pellets (Fig.2.6a,b), while proliferative cells were present uniformly within the volume of perfused micromasses (Fig.2.6c,d). The specificity of the Edu incorporation was confirmed by analyzing colchicine-treated samples, where no proliferative cells were detected (Fig.2.4d).

These results were consistent with an opposite trend in diameter change. Macromass pellets exhibited a statistically significant reduction in diameter (-15.33±3.90%) from day 0 to day 7 (Fig.2.6f), associated with a drop in the DNA content (Fig.2.7). An overtime increase in dimensions was conversely measured for the micromassess (+4.71±1.85%) during the same timeframe (Fig.2.6g), correlated with a growth in cell number (Fig.2.3).

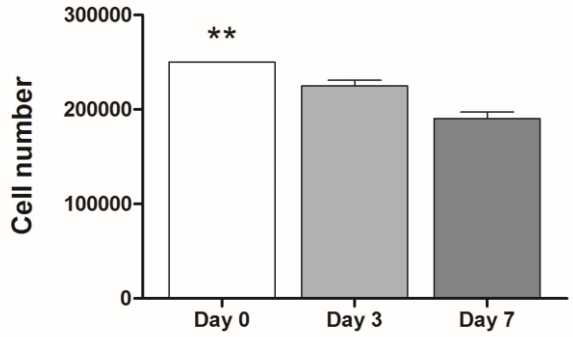

Figure 2.7. *CyQuant quantification of cell number within macroscale pellets during 7 days of culture.*

2.5.3 Effect of Wnt3a, FGF2 and TGFβ3 on perfused micromasses proliferation

The effect of different morphogen combinations on hBM-MSC perfused micromasses proliferation was assessed within the microfluidic platform. In details, microaggregates were cultured for 3 days in SFM conditioned either with a combination of 20 ng/ml rhWnt3a and 5 ng/ml FGF2 or with 1ng/ml of TGFβ3. A control condition (named vehicle) was also established, culturing microaggregates in SFM only. The tested combinations and concentrations of morphogens were selected based on promising results in terms of hBM-MSCs proliferation obtained through preliminary experiments carried out on 2D cultures (data not showed). After 3 days in culture, the vehicle condition exhibited a slight increase in cell number, comparable with that obtained in the TGFβ3 group. Conversely, the percentage increase of cell number with respect to day 0 was significantly higher when microaggregates were conditioned with Wnt3a+FGF2 (66.4%±15.1%) compared to both TGFβ3 (11.1%±4.0%) and vehicle conditions (3.7%±6.4%) (Fig.2.8a).

Collagen II expression was then assess for the three tested conditions, as to investigate the role of selected morphogens in early expression of a chondrogenic marker in hBM-MSCs perfused micromasses. Collagen II was only detected in the TGFβ3-treated group, possibly indicating its role in triggering a differentiation towards the chondrogenic lineage already after three days in culture (Fig.2.8d). Conversely, no Collagen II was expressed either in the (Wnt3a+FGF2)-stimulated group (Fig.2.8c) or in the control condition (Fig.2.8b).

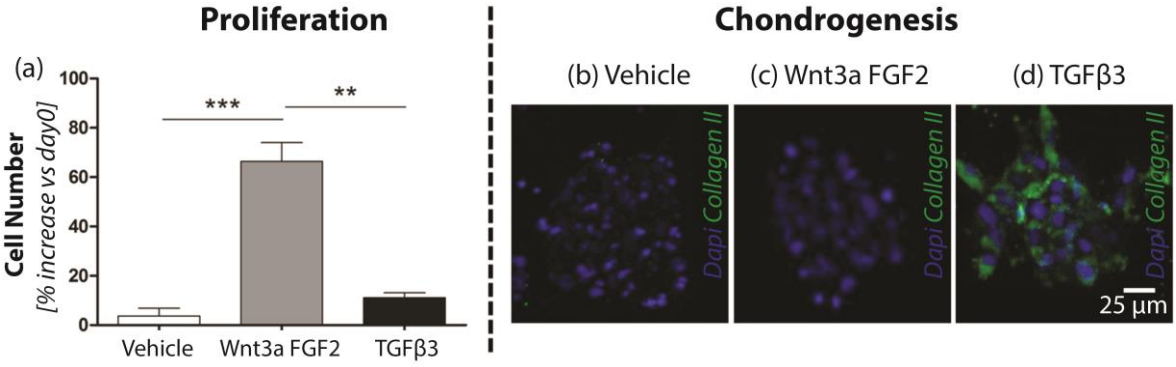

Figure 2.8. *Effect of Wnt3a, FGF2 and TGFβ3 on hBM-MSC microaggregates behavior. After 3 days in culture, the percentage increase of cell number with respect to day 0 was significantly higher when microaggregates were conditioned with Wnt3a+FGF2 compared to TGFβ3 condition (a). A negative control was also performed (named vehicle), culturing microaggregates in SFM without morphogens, leading during the 3 days culture to a slight increase in cell number, comparable with that obtained in the TGFβ3 group. Collagen II expression was then investigated for the three conditions. Results showed an expression of Collagen II only in the TGFβ3-treated group, possibly indicating its role in triggering a differentiation towards the chondrogenic lineage (d). Conversely, no Collagen II was detected neither in the (Wnt3a+FGF2)-stimulated group (c) or in the control condition (b).*

2.5.4 Logarithmic screening over the effect of TGFβ3 on micromasses

The microfluidic platform was finally exploited as a high-throughput tool for screening the concentration-dependent effect of morphogens on hBM-MSCs perfused micromasses. Throughout the SDG unit, hBM-MSCs micromasses were cultured under continuous perfusion of chondrogenic medium (SFM enriched with of 10^{-7} M dexamethasone), while serial dilutions of TGFβ3 were established throughout the logarithmic SDG configuration. In details, four orders of magnitude of TGFβ3 concentrations were spanned (0.1, 1, 10 and 100 ng/ml, and 0 ng/ml as negative control condition) (Fig.2.9).

After 7 days in culture, the highest concentration of TGFβ3 (100 ng/ml) resulted to be toxic and lead to micromasses disaggregation (Fig.2.9a-b), with no detectable cell proliferation or chondrogenesis (Fig.2.9c-d). At concentrations commonly used for *in vitro* chondrogenic differentiation protocols [31,37], cells did not proliferate but consistently deposited type II collagen. Interestingly, the lowest TGFβ3 concentration (0.1 ng/ml) could maintain proliferating cells over seven days in culture, while inducing chondrogenic differentiation, as assessed by type II collagen deposition.

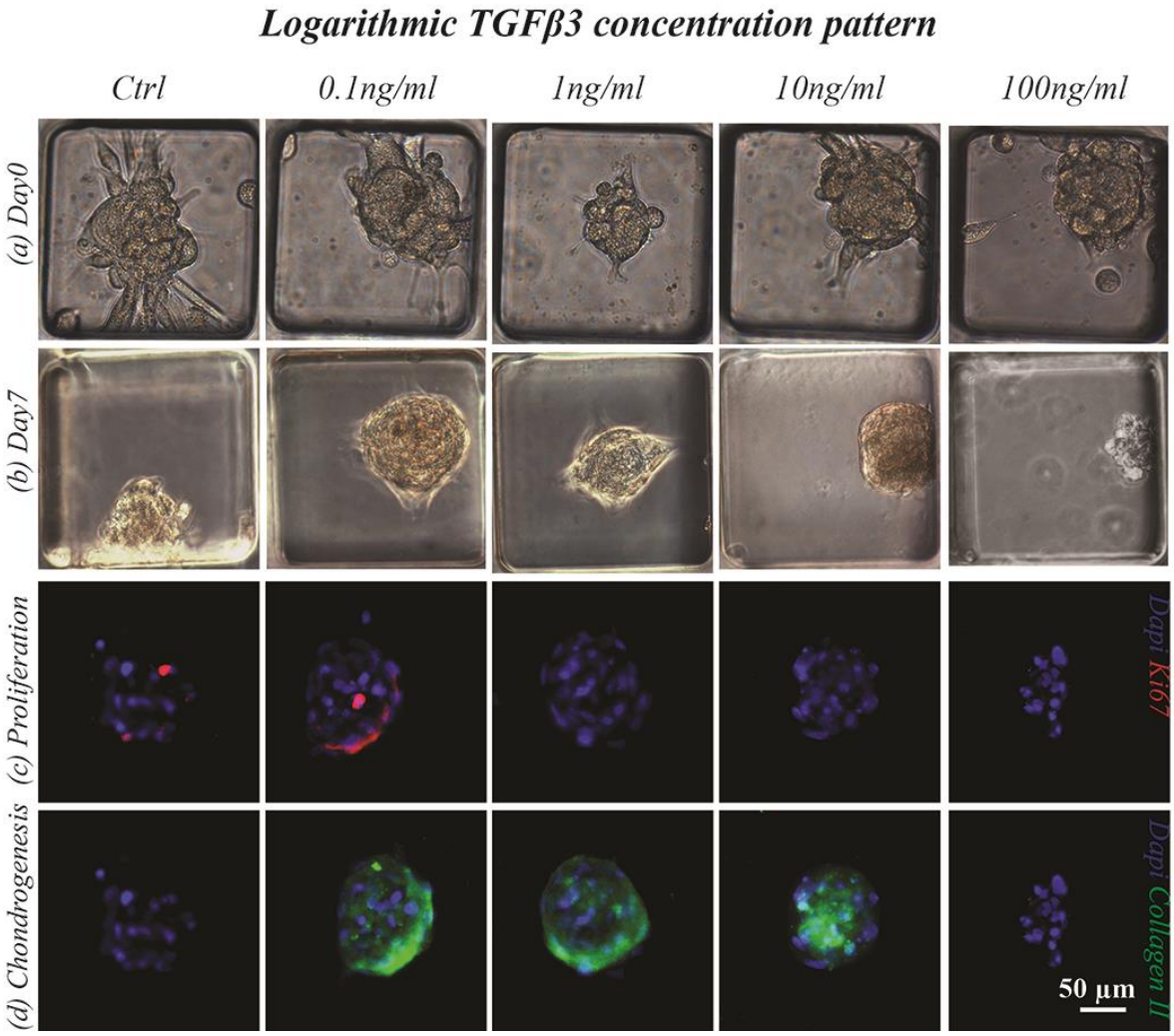

Figure 2.9. *Logarithmic screening over the effect of TGFβ3 on micromasses proliferation and differentiation. hBM-MSCs were cultured for 7 days under continuous perfusion of a concentration gradient of TGFβ3 spanning over four order of magnitude (0, 0.1, 1, 10 and 100ng/ml). Phase contrast images at day0 (a) and day7 (b) showed the toxic effect of the highest factor concentration, leading at micromasses disaggregation at the end of the culture period. Cell proliferation (c) and chondrogenesis (d) were investigated after 7 days in culture by staining microaggregates for Ki67 and Collagen II expression, underling TGFβ3 concentration-dependent cell responses.*

2.6 Discussion

The recapitulation of the events occurring during the limb development is currently being widely pursued to develop *in vitro* and *in vivo* strategies for skeletal tissue regeneration, according to the principles of "developmental engineering" [8]. In this regard, the reproducible instruction of clinically-relevant cell sources (e.g., hBM-MSCs) toward the endochondral route requires a deep understanding over their response to key morphoregulatory stimuli in relevant 3D models [9]. In this study, we developed a microscale platform for 3D mesenchymal cell micromasses *in vitro* generation and culture under continuous and controlled perfusion, compatible with high-throughput exposure to exogenous factors and live cell imaging. We demonstrated that hBM-MSCs could spontaneously form 3D aggregates upon injection into the designed culture microchambers, and respond more uniformly and efficiently to key morphogens when perfused in the system as compared to traditional macroscale and static approaches. The work thus provides a proof-of-principle of the potentialities of the microfluidic platform as a high-throughput tool to screen the effect of key morphogens on 3D perfused micromasses specification at a more physiological level, finally aiming at recapitulating the endochondral route starting from adult cell sources in a spatio-temporally controlled fashion.

To date, several strategies have been developed to induce the condensation of cell micromasses by means of static approaches (i.e., hanging-drop techniques, microwells) [38-42], aiming at demonstrating the benefits of the scale reduction of 3D models. Although successful, these approaches still rely on static and manual culture systems, unable to efficiently investigate 3D cell responses in a automatic manner. Conversely, some attempts have been made to inject previously formed micromasses within microfluidic platforms for the subsequent culture under controlled conditions [25-27]. However, only few available devices integrate both functionalities, and they mainly rely on the intrinsic ability of embryonic cells to spontaneously form EBs [28,29]. Attempts have been recently made for generating microaggregates within microfluidic platforms starting from adult cell sources; nonetheless, they were mostly based on complex multiple-layer designs in which cell condensation was induced through the formation of vortices and rotational flows within microchambers [43,44].
We developed an innovative microfluidic platform consisting of a single layered device integrating independent culture units, each featuring 10 cubic chambers (thus potentially useful for studying paracrine effect), serially connected to a fluidic network designed to

precisely deliver given concentrations of morphogens. Integrating for the first time the capabilities to (i) generate 3D hBM-MSC micromasses into defined spatial configurations and (ii) culturing them under continuous laminar flow perfusion of specific morphogens concentrations, the proposed microfluidic platform thus represent a powerful tool for modeling 3D biological systems at a physiological scale.

In particular, the platform allowed obtaining condensation of tens of hBM-MSCs (77±15) within each culture microchamber into spherical micromasses, without the need of any rotational flow or external induction. This was possible due to (i) the low adhesiveness of the PDMS substrate, (ii) the geometry and size of the microwells, and (iii) the relative ratio between the cell number and well size, yielding a high cell density in a confined small volume. The possibility to achieve a non-externally induced condensation of hBM-MSCs thus gave insights for overcoming one of the major limitation of traditional scaffold-free systems involving 3D mesenchymal cell cultures, which are mainly based on macromass pellets [17,31]. Indeed, such models require an initial forced centrifugation step, which leads to the establishment of too tight cell-cell and cell-ECM interactions, high variability in the time required to form 3D aggregates (24÷72 hours), which anyhow results longer with respect to the limb mesenchymal progenitor condensation process, and non-uniformly shaped tissues [45]. Conversely, the proposed platform allowed to achieve an initial non-externally induced condensation of hBM-MSCs within 3 hours, generating micromasses featuring rather uniform sizes (56.2±3.9μm) and dimensionally similar to the native model. The effective interconnection among cells, forming condensed micromasses and not only cell clusters, was further demonstrated by the early formation of actin networks and by a uniform expression of vinculin and N-cadherin throughout their entire volume. A deeper investigation should though be performed for further characterizing the biological pathways involved in hBM-MSCS aggregation, in order to compare the proposed non-externally induced condensation model with the spontaneous condensation phenomena occurring during limb development.

The platform was further exploited for culturing generated micromasses under controlled perfusion aiming at investigating the uniformity of their response to external morphogens stimuli. Compared with traditional macropellets models, which mainly suffered from an overall heterogeneity in cell responses correlated with the presence of necrotic cores [17,47], perfused micromasses responded to TGFβ3 exhibiting a 33.8-fold higher percentage of Edu^+ cells, homogeneously spread throughout the whole volume. These observations

confirmed the potentiality of the model in replicating the 3D expansion step occurring during the early stages of limb development [11], thus overcoming one of the main limits of macroscale models, i.e. an overall drop in cell number independently from the culture conditions [17]. Furthermore, by using fixed, previously optimized morphogen concentrations [17], optimized throughout preliminary dose-dependent studies on 2D hBM-MSCs cultures, a pre-chondrogenic expansion similar to that occurring in the native limb bud was achieved. Indeed, through a combination of Wnt3a and FGF2, an increase in cell number of 66.4±15.1% was observed in the perfused micromasses from day 0 to day 3, whereas no expression of collagen type-II was detected. Conversely, the perfusion of TGFβ3-based medium induced an earlier onset of TGFβ-mediated chondrogenesis compared to macroscale models [48], as exemplified by the expression of collagen type-II already after 3 days in culture.

Finally, the exploitation of the serial dilution generator unit allowed for screening the concentration-dependent effect of a key morphoregulatory factor (TGFβ3) on the 3D hBM-MSCs model. The obtained proof-of-principle results underline the efficacy of the presented model to detect different cell responses in the presence of different morphogen concentrations, spanning over four orders of magnitude. Interestingly, the lowest concentration tested (100 pg/ml) was enough to trigger specific cellular responses (i.e. chondrogenic specification), which cannot be detected at the macroscale without delivering ten times higher concentrations of the morphogen. The presence of secondary inlets within the platform will allow for integrating an automatic temporal control over the delivery of morphogens for further investigating the temporal dynamic of key signaling pathways.

Our findings indicate the potentiality of the presented microfluidic system to investigate the effect of key morphogens, applied in a controlled and high-throughput fashion in different sequences, combinations and concentration ranges, on early stages of 3D chondrogenesis by hBM-MSCs.

Conclusive remarks

In this chapter, an innovative microfluidic strategy was introduced for generating, culturing and conditioning 3D stem cell microaggregates within a chemically controlled microenvironment. The presented microfluidic device was used particularly to replicate the initial stages of the endochondral route, providing a more uniform cell response to external cues compared to traditional macroscale and static approaches. Allowing the investigation of cartilage development signals, the microscale platform thus represents a powerful tool to develop novel and more effective cartilage repair strategies based on adult stem cell chondrogenesis.

Building on the presented results, we envision further applications of the microfluidic platform for systematic studies as an *in vitro* limb bud model, as well as in the pharmaceutical industry for screening compounds intended to induce regeneration of mesenchymal tissues. Furthermore, the applicability of the system may also be extended to different cell sources, where initial cell condensation and the onset of a 3D structure are phenomena expected to mediate a physiological response to exogenous signals.

Considering its peculiarities and capabilities, the presented platform could finally find application as screening tool in the field of cancer biology. Indeed, the ability to screen directly *on chip* the effect of different concentrations/combinations of chemotherapeutics agents on 3D micromasses, mimicking the pathological microenvironment, could lead to a better understanding of etiology, yielding a faster development of treatment strategies of cancer-related diseases.

References

1. Abo A, Clevers H. *Modulating WNT receptor turnover for tissue repair.* Nature Biotechnology 2012;30(9):835-836.
2. Sasai Y, Eiraku M, Suga H. *In vitro organogenesis in three dimensions: self-organising stem cells.* Development 2012;139(22):4111-4121.
3. Sasai Y. *Cytosystems dynamics in self-organization of tissue architecture.* Nature 2013;493(7432):318-326.
4. Leucht P, Minear S, Ten Berge D, Nusse R, Helms JA. *Translating insights from development into regenerative medicine: The function of Wnts in bone biology.* Seminars in Cell & Developmental Biology 2008;19(5):434-443.
5. Lenas P, Moos M, Jr., Luyten FP. *Developmental Engineering: A New Paradigm for the Design and Manufacturing of Cell-Based Products.* Part I: From Three-Dimensional Cell Growth to Biomimetics of In Vivo Development. Tissue Engineering Part B-Reviews 2009;15(4):381-394.
6. Jukes JM, Both SK, Leusink A, Sterk LMT, Van Blitterswijk CA, De Boer J. *Endochondral bone tissue engineering using embryonic stem cells.* Proceedings of the National Academy of Sciences of the United States of America 2008;105(19):6840-6845.
7. Scotti C, Tonnarelli B, Papadimitropoulos A, Scherberich A, Schaeren S, Schauerte A, Lopez-Rios J, Zeller R, Barbero A, Martin I. *Recapitulation of endochondral bone formation using human adult mesenchymal stem cells as a paradigm for developmental engineering.* Proceedings of the National Academy of Sciences of the United States of America 2010;107(16):7251-7256.
8. Scotti C, Piccinini E, Takizawa H, Todorov A, Bourgine P, Papadimitropoulos A, Barbero A, Manz MG, Martin I. *Engineering of a functional bone organ through endochondral ossification.* Proceedings of the National Academy of Sciences of the United States of America 2013;110(10):3997-4002.
9. Tonnarelli B, Centola M, Barbero A, Zeller R, Martin I. *Chapter Eleven - Re-engineering Development to Instruct Tissue Regeneration.* In: Brigitte G, editor. Current Topics in Developmental Biology: Academic Press; 2014. p 319-338.
10. Zeller R, Lopez-Rios J, Zuniga A. *Vertebrate limb bud development: moving towards integrative analysis of organogenesis.* Nature Reviews Genetics 2009;10(12):845-858.
11. ten Berge D, Brugmann SA, Helms JA, Nusse R. *Wnt and FGF signals interact to coordinate growth with cell fate specification during limb development.* Development 2008;135(19):3247-3257.
12. Oldershaw RA, Baxter MA, Lowe ET, Bates N, Grady LM, Soncin F, Brison DR, Hardingham TE, Kimber SJ. *Directed differentiation of human embryonic stem cells toward chondrocytes.* Nature Biotechnology 2010;28(11):1221-U80.
13. Inoue T, Kagawa T, Fukushima M, Shimizu T, Yoshinaga Y, Takada S, Tanihara H, Taga T. *Activation of canonical Wnt pathway promotes proliferation of retinal stem cells derived from adult mouse ciliary margin.* Stem Cells 2006;24(1):95-104.
14. Johnstone B, Hering TM, Caplan AI, Goldberg VM, Yoo JU. *In Vitro Chondrogenesis of Bone Marrow-Derived Mesenchymal Progenitor Cells.* Experimental Cell Research 1998;238(1):265-272.
15. Boland GM, Perkins G, Hall DJ, Tuan RS. *Wnt 3a promotes proliferation and suppresses osteogenic differentiation of adult human mesenchymal stem cells.* Journal of Cellular Biochemistry 2004;93(6):1210-1230.
16. Baksh D, Tuan RS. *Canonical and non-canonical wnts differentially affect the development potential of primary isolate of human bone marrow mesenchymal stem cells.* Journal of Cellular Physiology 2007;212(3):817-826.

17. Centola M, Tonnarelli B, Scharen S, Glaser N, Barbero A, Martin I. *Priming 3D cultures of human mesenchymal stromal cells toward cartilage formation via developmental pathways.* Stem Cells and Development 2013;22(21):2849-58.
18. El-Ali J, Sorger PK, Jensen KF. *Cells on chips.* Nature 2006;442(7101):403-411.
19. Titmarsh D, Hidalgo A, Turner J, Wolvetang E, Cooper-White J. *Optimization of Flowrate for Expansion of Human Embryonic Stem Cells in Perfusion Microbioreactors.* Biotechnology and Bioengineering 2011;108(12):2894-2904.
20. Titmarsh DM, Chen H, Wolvetang EJ, Cooper-White JJ. *Arrayed cellular environments for stem cells and regenerative medicine*. Biotechnol. J. 2012:n/a-n/a.
21. Frank T, Tay S. *Flow-switching allows independently programmable, extremely stable, high-throughput diffusion-based gradients.* Lab on a Chip 2013;13(7):1273-1281.
22. Titmarsh DM, Ovchinnikov DA, Wolvetang EJ, Cooper-White JJ. *Full factorial screening of human embryonic stem cell maintenance with multiplexed microbioreactor arrays.* Biotechnology Journal 2013;8(7):822-834.
23. Xiong B, Ren K, Shu Y, Chen Y, Shen B, Wu H. *Recent Developments in Microfluidics for Cell Studies.* Advanced Materials 2014:n/a-n/a.
24. Kinney MA, McDevitt TC. *Emerging strategies for spatiotemporal control of stem cell fate and morphogenesis.* Trends in Biotechnology 2013;31(2):78-84.
25. Suri S, Singh A, Nguyen AH, Bratt-Leal AM, McDevitt TC, Lu H. *Microfluidic-based patterning of embryonic stem cells for in vitro development studies.* Lab on a Chip 2013;13(23):4617-4624.
26. Cimetta E, Sirabella D, Yeager K, Davidson K, Simon J, Moon R, Vunjak-Novakovic G. *Microfluidic bioreactor for dynamic regulation of early mesodermal commitment in human pluripotent stem cells.* Lab on a Chip 2012.
27. Ruppen J, Cortes-Dericks L, Marconi E, Karoubi G, Schmid RA, Peng R, Marti TM, Guenat OT. *A microfluidic platform for chemoresistive testing of multicellular pleural cancer spheroids.* Lab on a Chip 2014;14(6):1198-1205.
28. Torisawa Y-s, Chueh B-h, Huh D, Ramamurthy P, Roth TM, Barald KF, Takayama S. *Efficient formation of uniform-sized embryoid bodies using a compartmentalized microchannel device.* Lab on a Chip 2007;7(6):770-776.
29. Torisawa Y-s, Mosadegh B, Luker GD, Morell M, O'Shea KS, Takayama S. *Microfluidic hydrodynamic cellular patterning for systematic formation of co-culture spheroids.* Integrative Biology 2009;1(11-12).
30. Lise A, Stringa E, Woodward W, Mello M, Tuan R. *Embryonic Limb Mesenchyme Micromass Culture as an In Vitro Model for Chondrogenesis and Cartilage Maturation.* In: Tuan R, Lo C, editors. Developmental Biology Protocols: Humana Press; 2000. p 359-375.
31. Johnstone B, Hering TM, Caplan AI, Goldberg VM, Yoo JU. *In vitro chondrogenesis of bone marrow-derived mesenchymal progenitor cells.* Experimental Cell Research 1998;238(1):265-272.
32. Jeon NL, Dertinger SKW, Chiu DT, Choi IS, Stroock AD, Whitesides GM. *Generation of solution and surface gradients using microfluidic systems.* Langmuir 2000;16(22):8311-8316.
33. Xia YN, Whitesides GM. *Soft Lithography.* Angew. Chem., Int. Ed. 1998;37:550.
34. Martin I, Muraglia A, Campanile G, Cancedda R, Quarto R. *Fibroblast Growth Factor-2 Supports ex Vivo Expansion and Maintenance of Osteogenic Precursors from Human Bone Marrow.* Endocrinology 1997;138(10):4456-4462.
35. Monahan J, Gewirth AA, Nuzzo RG. *A Method for Filling Complex Polymeric Microfluidic Devices and Arrays.* Analytical Chemistry 2001;73(13):3193-3197.

36. Martin I, Dozin B, Quarto R, Cancedda R, Beltrame F. *Computer-based technique for cell aggregation analysis and cell aggregation in in vitro chondrogenesis.* Cytometry 1997;28(2):141-146.
37. Frenz DA, Liu W, Williams JD, Hatcher V, Galinovic-Schwartz V, Flanders KC, Van de Water TR. *Induction of chondrogenesis: requirement for synergistic interaction of basic fibroblast growth factor and transforming growth factor-beta.* Development 1994;120(2):415-424.
38. Teixeira LSM, Leijten JCH, Sobral J, Jin R, van Apeldoorn AA, Feijen J, van Blitterswijk C, Dijkstra PJ, Karperien M. *High Throughput Generated Micro-aggregates of Chondrocytes Stimulate Cartilage Formation In Vitro and In Vivo.* European Cells & Materials 2012;23:387-399.
39. Fennema E, Rivron N, Rouwkema J, van Blitterswijk C, de Boer J. *Spheroid culture as a tool for creating 3D complex tissues.* Trends in Biotechnology 2013;31(2):108-115.
40. Bartosh TJ, Ylostalo JH. *Preparation of Anti-Inflammatory Mesenchymal Stem/Precursor Cells (MSCs) Through Sphere Formation Using Hanging-Drop Culture Technique.* Current Protocols in Stem Cell Biology: John Wiley & Sons, Inc.; 2007.
41. Hildebrandt C, Büth H, Thielecke H. *A scaffold-free in vitro model for osteogenesis of human mesenchymal stem cells.* Tissue and Cell 2011;43(2):91-100.
42. Kapur SK, Wang X, Shang H, Yun S, Li X, Feng G, Khurgel M, Katz AJ. *Human adipose stem cells maintain proliferative, synthetic and multipotential properties when suspension cultured as self-assembling spheroids.* Biofabrication 2012;4(2):025004.
43. Ota H, Yamamoto R, Deguchi K, Tanaka Y, Kazoe Y, Sato Y, Miki N. *Three-dimensional spheroid-forming lab-on-a-chip using micro-rotational flow.* Sensors and Actuators B: Chemical 2010;147(1):359-365.
44. Ota H, Miki N. *Microfluidic experimental platform for producing size-controlled three-dimensional spheroids.* Sensors and Actuators A: Physical 2011;169(2):266-273.
45. Babur BK, Ghanavi P, Levett P, Lott WB, Klein T, Cooper-White JJ, Crawford R, Doran MR. *The Interplay between Chondrocyte Redifferentiation Pellet Size and Oxygen Concentration.* PLoS ONE 2013;8(3):e58865.
46. Goldring MB, Tsuchimochi K, Ijiri K. *The control of chondrogenesis.* Journal of Cellular Biochemistry 2006;97(1):33-44.
47. Dexheimer V, Frank S, Richter W. *Proliferation as a Requirement for In Vitro Chondrogenesis of Human Mesenchymal Stem Cells.* Stem Cells and Development 2012;21(12):2160-2169.
48. Hung S-C, Kuo P-Y, Chang C-F, Chen T-H, Ho LL-T. *Alpha-smooth muscle actin expression and structure integrity in chondrogenesis of human mesenchymal stem cells.* Cell and Tissue Research 2006;324(3):457-466.

3

Tailoring the 3D microarchitecture around cells: photopolymerizable hydrogel-based photo-mold-patterning (PMP) protocol

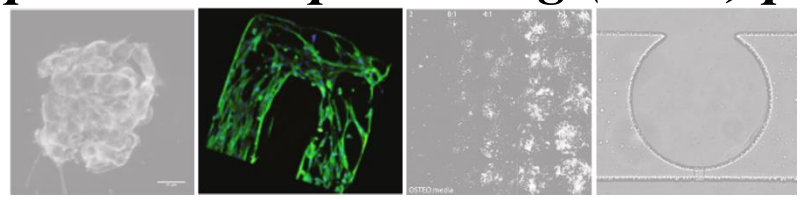

This chapter partially refers to:

Fabrication of 3D cell-laden hydrogel microstructures through photo-mold-patterning. Occhetta P, Sadr N, Piraino F, Redaelli A, Moretti M, Rasponi M. Biofabrication 2013 (vol.5 issue 3 pp.10) DOI: 10.1088/1758-5082/5/3/035002

VA-086 Methacrylate Gelatine Photopolymerizable Hydrogels: a Parametric Study for Highly Biocompatible 3D Cell Embedding. Occhetta P, Visone R, Russo L, Cipolla L, Moretti M, Rasponi M. Journal of Biomedical Materials Research: Part A 2014 DOI: 10.1002/jbm.a.35346

Rationale

While some 3D cell culture approaches rely on the ability of cells to re-organize themselves, including the study of tissue morphogenesis introduced in Chapter 2, in others a pre-determined guiding of cell patterning in the 3D environment is crucial for obtaining functional cellular responses. Most of the native tissues are indeed characterized by spatially organized 3D functional units (or "building blocks"), which define cells–cells and cells–extracellular matrix interactions. The ability to design *in vitro* models mimicking this spatial organization contributes to a better understanding over the role of 3D ECM microarchitecture on different cells behavior and, in perspective, to engineer functional constructs.

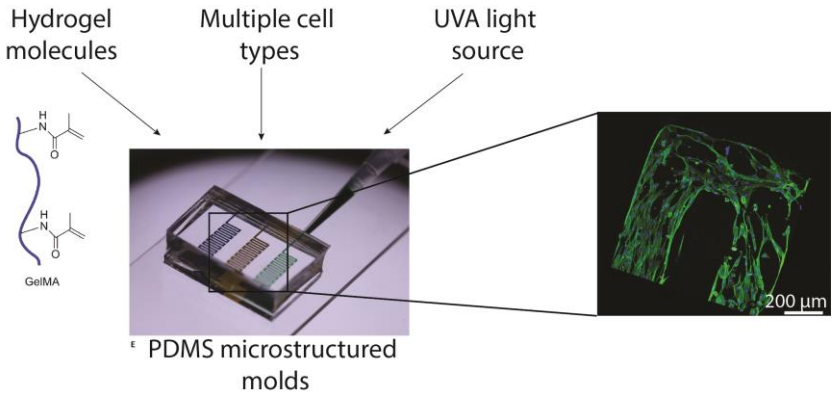

A microscale strategy for spatially tailoring the 3D microenvironment around cells was introduced, which combines an innovative biocompatible photopolymerizable hydrogel (VA-086-GelMA) and an easy to handle photo-mold-patterning (PMP) technique, based on the use of PDMS microstructured molds.

In this perspective - within the context of a collaboration with the Cell and Tissue Engineering Laboratory (IRCCS Galeazzi Orthopedic Institute, Milano, Italy) - we introduced a novel protocol for tailoring the microarchitecture of the environment around cells, through the generation of 3D cell-laden hydrogel microscaled models. The proposed approach combines an innovative biocompatible photopolymerizable hydrogel (VA-086-GelMA) and an easy to handle photo-mold-patterning (PMP) technique, based on the use of PDMS microstructured molds. The introduced method could thus be considered as a promising and cost effective tool for designing spatially accurate *in vitro* models mimicking the "building-blocks" of native tissues.

3.1 Introduction

Tissues in the body are composed of functional 3D units, characterized by a spatially organized microarchitecture comprised of cells and ECM [1]. Each cell continuously interacts with its surrounding 3D microenvironment through biochemical, biomechanical and bioelectrical signals, which vary dynamically in both time and space and contribute in the regulation of cellular behavior and fate processes [2]. When developing new *in vitro* models or functional bio-constructs, the ability of spatially and functionally replicating the native tissue microarchitecture is one of the crucial steps to obtain reliable and physiologically consistent cell responses [3]. Indeed, while traditional 2D *in vitro* culture techniques lack in reproducing the complex microarchitecture found *in vivo*, 3D models have been demonstrated to recapitulate unprecedented cues from the native environment [4]. Nevertheless, only few recent technological approaches succeeded in tailoring the microscale 3D geometrical features of cell microenvironment [5]. Among other methods, the combination of novel biomaterials and microfabrication technologies has been rapidly generating perspectives for addressing this challenge [6-8].

In this contest, the choice of appropriate biomaterials becomes crucial in order to mimic native tissues microenvironment with respect to both biological integration and geometrical replication. These requirements have been showed to be potentially satisfied by using polymeric hydrogels [9]. Indeed, hydrogels exhibit high similarities to the natural ECM [10] thanks to some unique properties, such as highly swollen network structures, which maximize nutrients transfers, the presence of functional groups, which can be chemically modified to add specific functions, and mechanical properties easily tunable within a wide range [11]. Moreover, they have been demonstrated to be highly affine with innovative microtechnologies such as photo- and soft- lithographic approaches [12], making them suitable to obtain 3D biomimetic replicates with a highly controlled microtopography. A variety of synthetic [13-16] and natural [17-20] macromolecules have been used so far to fabricate hydrogel-based engineered environments [9], either as substrates for cellular seeding [13 21] or as cell-laden 3D matrices [14,15 10]. In particular, the fabrication of cell-laden hydrogels is tightly correlated to the biocompatibility of the crosslinking approach. Most chemical methods are not compatible with 3D encapsulation of viable cells, usually relying on cytotoxic chemicals or enzymatic agents to trigger the polymerization [17]. On the other hand, thermal hydrogel reticulation has been investigated in combination with inexpensive soft lithography

techniques, resulting in micropatterned 3D structures with dimension ranging between 1000 µm [22] and 50 µm [23]. However, the presence of living cells within the biomaterial poses an upper temperature threshold to 37°C, generally resulting in relatively long crosslinking time. Being the temporal control over reaction a critical parameter to generate uniformly populated 3D constructs, additional rotating systems may be required to thermally crosslink cell-laden hydrogels in order to prevent cell tendency to settle down and thus achieve a uniform 3D cell distribution within the matrix [24]. On the other hand, fast crosslinking reaction corresponds to rapid gel viscosity increase, a characteristic that compensates cells tendency to settle down and favors a uniform 3D cell distribution within the microstructures. In this perspective, light responsive hydrogels (or photohydrogels) have been successfully used to obtain 3D patterns within tens of seconds [25]. Photopatterning techniques are generally based on the presence of a photomask between the light source and the pre-polymer solution, the latter including light-specific photoinitiator (PI) molecules [26]. Based on this approach, the fabrication of free standing microgels [27] as well as micropatterns [28] has been demonstrated. In addition, photopatterning was iterated for the construction of multicellular patterns [29] as well as the free standing microgels were assembled based on different interaction forces (interface based, magnetic, acoustic) to form complex macrostructures [30]. However, similarly to photolithography, the achievable resolution of microgels obtained with photopatterning approaches is strongly affected by light source collimation [31]. Moreover, the suitability of the photopolymerization process for embedding viable cells relies on the definition of optimal and biocompatible combinations of polymeric precursors, light source and PI. Among others, methacrylate gelatin (GelMA) has been widely investigated in the last few years in combinations with different PI molecules and lights sources [32]. GelMA is indeed a cheap and easy to handle derivative of collagen, which presents both natural cell binding motifs, such as RGD and MMP-sensitive degradation sites, and different amino acid side-chain functionalities (carboxylic acid, amines, hydroxyl) allowing for further covalent modifications [17]. Irgacure 2959 is widely considered the golden standard for GelMA hydrogel cross-linking [17,32-34]; however, with an adsorption peak around 320nm and a not negligible toxicity to cells, its use had to be accurately optimized for its limited biocompatibility properties [35]. Among others, VA-086, a water soluble azo initiator molecule, recently proved to yield low cytotoxic effects in both precursor and radical forms

[36], together with an absorption peak, corresponding to a range of wavelengths between 365 and 385nm, more conservative in terms of cell viability.

In the present study, a new gelatin-based photopolymerizable hydrogel was introduced, obtained exploiting a biocompatible combination of VA-086 photoinitiator and UVA LED light source. The effect of photopolymerization parameters was first systematically investigated to assess how the pre-polymer concentration (GelMA) and light irradiance influences VA086-GelMA hydrogels crosslinking, mechanical and biological properties at the macroscale (as detailed in paragraphs 3.2 and 3.3). Moreover, with the aim of obtaining 3D uniformly dispersed cell-laden micropatterns replicating user defined geometrical features, we present a simple and innovative microscaled Photo-Mold Patterning (PMP) protocol based on VA086-GelMA hydrogels (introduced in the paragraph 3.4). This protocol combines the advantages of thermal mold patterning approaches (high resolution without the need of expensive collimated light sources) [22] with the benefits of using photopolymerizable hydrogels (reduced crosslinking time) [17], proving for the first time the possibility to generate highly viable cell-laden micropatterns through a low-cost and versatile UVA LED light source.

3.2 VA086-GelMA hydrogels synthesis and functional characterization

In the following paragraphs, a novel photopolymerizable hydrogel, named VA-086-GelMA, is introduced. First, GelMA synthesis and chemical characterization are described (3.2.1). Subsequently, an innovative GelMA photopolymerization protocol, based on biocompatible photoinitiator (VA-086) and UV light source (UVA LED), is presented (3.2.2) and fully characterized evaluating crosslink time (3.2.3), mechanical properties and biocompatibility (3.2.5) of the resulting hydrogels as function of different crosslinking parameters (GelMA and PI concentration, light irradiance).

3.2.1 Gelatin methacrylate synthesis and ^{1}H NMR characterization

Methacrylated gelatin (GelMA) was synthesized following a previously reported protocol [32] (Fig.3.1a). Briefly, type A porcine skin gelatin (Sigma-Aldrich Corporation, St. Louis, Missouri, USA) was dissolved at 10% (w/v) in phosphate buffer saline (PBS, GIBCO) solution (pH=7.5) at 50°C. 15% (v/v) Methacrylic anhydride (acrylate agent, MA, Sigma-Aldrich Corporation, St. Louis, Missouri, USA) was then added to the gelatin solution at a rate of 0.1 ml/min until reaching the desired volume and allowed to react while vigorously stirring. After three hours, the reaction was quenched by adding pre-heated PBS and the obtained solution was dialyzed for ten days against distilled water at 50°C throughout 12-14KDa cutoff dialysis tubing (Sigma-Aldrich Corporation, St. Louis, Missouri, USA). The solution was finally filtered, freeze-dried for 66 hours and stored at -80°C until further use.

As previously described for MA-gelatin[17], the efficacy of the methacrylation reaction was determined by ^{1}H-NMR analyzing the signals coming from the methacrylic moiety before cross-linking, since the resonances from the methacrylamide methylene protons occur in a region free from other signals due to the protein (5.2-5.7 ppm). In details, 30 mg of both GelMA and plain gelatin were dissolved in 0.6 mL of D_2O; the sealed NMR tubes were heated to 70°C till complete dissolution. The spectra were recorded at 400 MHz on a Varian Mercury instrument and showed a successful methacrylation.

3.2.2 VA-086-GelMA hydrogel photopolymerization

GelMA hydrogels were obtained by radical cross-linking of methacrylamide modified gelatin in the presence of a PI activated by a 1.8 W LED (385 nm; LZ4-00UA00, LED Engine, Inc.) light source (Fig. 3.1b). In details, the PI molecule 2,2-Azobis (2-methyl-

N-(2-hydroxyethyl)propionamide) (VA-086, Wako Chemicals GmbH, Germany) was dissolved in PBS at room temperature at 1.5% (w/v). Subsequently, GelMA was added to the PI solution and mixed at room temperature until complete dissolution. Through a standard micropipette, 20µl of this prepolymer solution were placed inside a Petri dish into a silicone cylindrical well (diameter= 6mm and height= 0.5mm) obtained by means of a biopsy puncher. The sample was thus irradiated using the LED source until complete polymerization, and the required time was recorded. A sample was considered fully polymerized whether it satisfied the following criteria: (i) it maintained a 3D shape without releasing macroscopic debris upon silicone template removal and (ii) it did not dissolved when immersed in PBS and incubated at 37°C up to 1 hours.

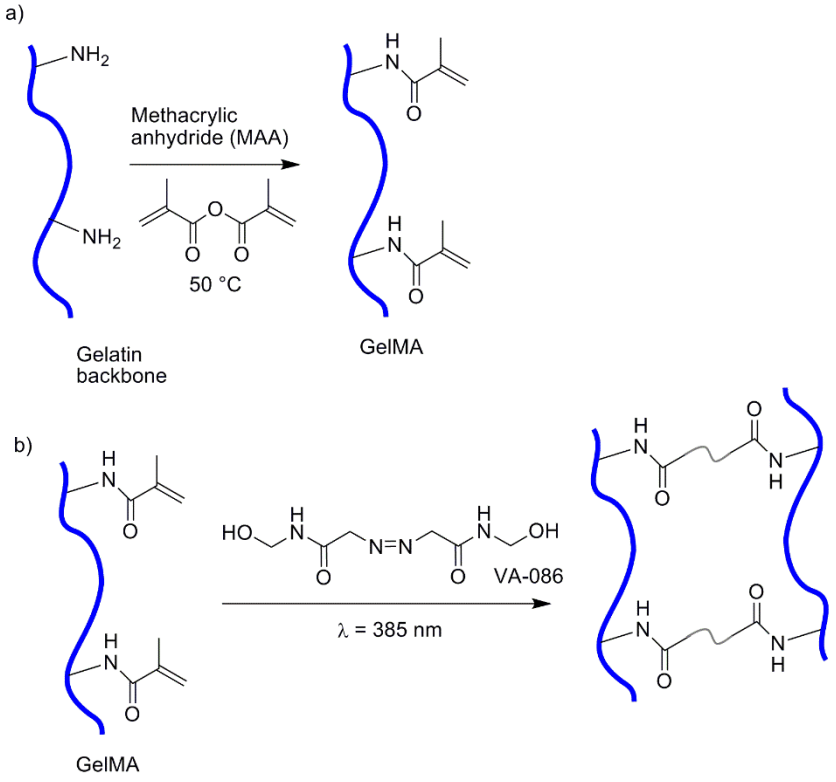

Figure 3.1. *Methacrylated gelatin (GelMA) synthesis and cross-linking reaction. Gelatin monomers were reacted with methacrylic anhydride (MA) to replace lysine groups with methacrylate pendant groups (a). Hydrogel network was then created cross-linking GelMA using a LED light source in the presence of a photoinitiator (b).*

3.2.3 Parametric study on VA-086-GelMA hydrogel photopolymerization time

The described photopolymerization protocol was fully characterized for the synthesized material, by assessing the influence of different parameters on the cross-linking time. In particular, the considered parameters were (i) the irradiance of the light source (1.5-

14 mW/cm^2), and (ii) the GelMA concentration (5%, 7.5% and 10% w/v) in the pre-polymer solution (see Table 3.1). Furthermore, the effect of PI concentration (0.5%, 1%, 1.5% w/v) was evaluated on a GelMA concentration of 10% (w/v). Each condition was tested in triplicates and the polymerization times were recorded.

Table 3.1 *Parameters tested during GelMA photopolymerization to assess their influence on sample cross-linking time*

% GelMA in pre-polymer solution (w/v)	5, 7.5, 10
Irradiance (mW/cm^2)	1.5 , 2, 3.5, 6, 14

First, the influence of the gelatin concentration was evaluated, maintaining VA-086 concentration at 1.5% (w/v). Figure 3.2a shows a comparison between polymerization times of samples obtained for GelMA concentrations of 5, 7.5 and 10% (w/v) for different irradiance conditions. Time values higher than 360s were considered too long for cell embedding procedure and, coherently, not reported. As expected, the polymerization time decreased increasing the irradiance for all the tested conditions. Moreover, increasing the GelMA concentration, the polymerization time decreased. In particular, for high MA GelMA, polymerization times decreased from 320sec to 140sec at 1.5mW/cm^2 and from 140sec to 35sec at 14mW/cm^2, when GelMA concentration was increased from 5% to 10% (w/v).

To assess the influence of PI concentration on polymerization times, GelMA was tested fixing the concentration at 10% (w/v) and varying VA-086 concentration from 0.5% to 1.5% (w/v). Increasing the VA-086 concentration resulted in a drop of the cross-linking time among all irradiance intensities (Fig.3.2b). In details, the increase of VA-086 content reaction times dropped from 250sec to 140sec and from 45sec or 30sec at 1.5mW/cm^2 and 14mW/cm^2, respectively.

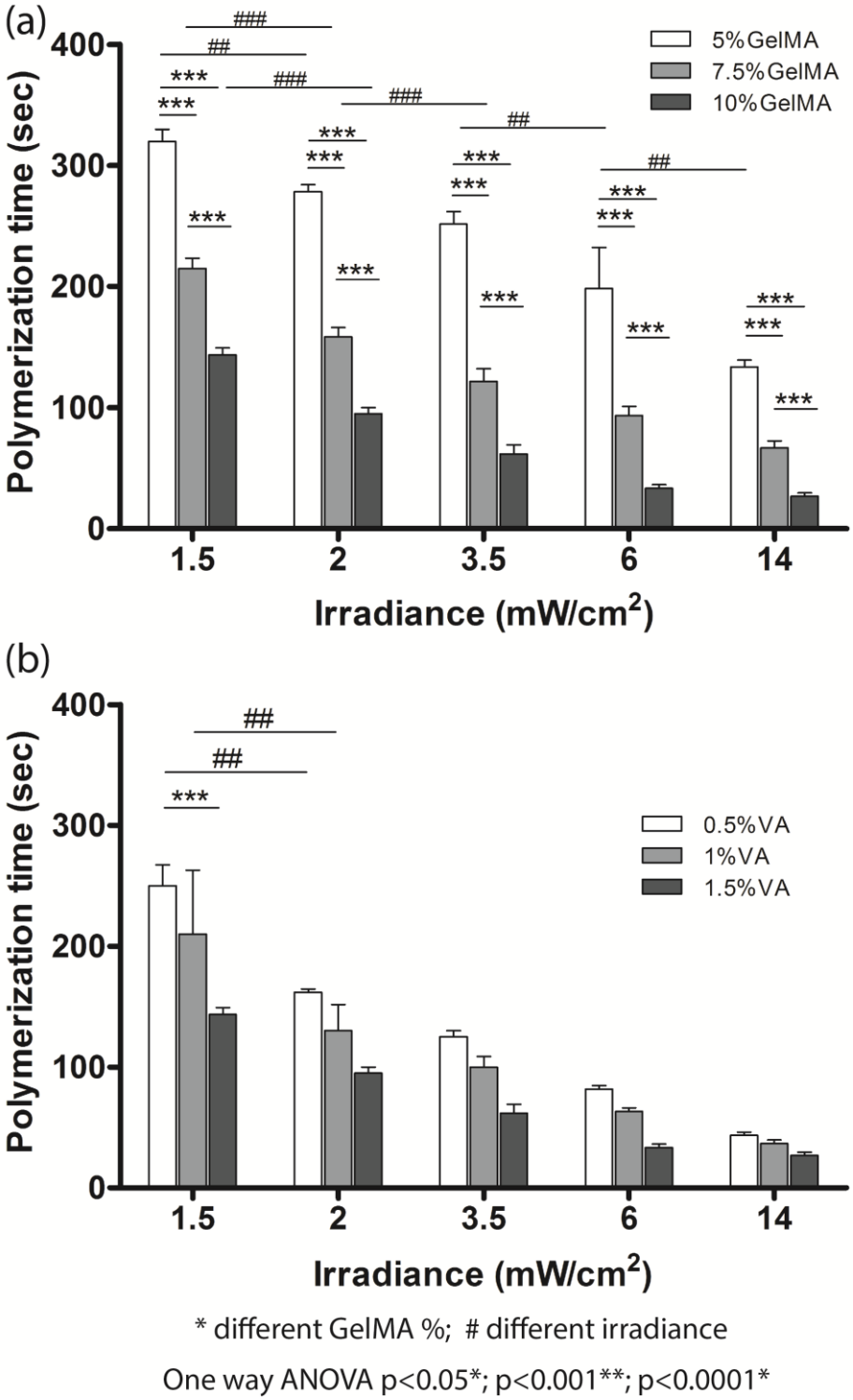

Figure 3.2. *GelMA cross-linking time in function of LED irradiance. Comparison between polymerization times of GelMA samples obtained varying gelatin (a) or VA-086 (b) concentration. Error bars represent positive standard deviations. (One way ANOVA p<0.05*; p<0.001**; p<0.0001* - * different GelMA %; # different irradiance).*

3.2.4 VA-086-GelMA hydrogel rheological characterization

Dynamic shear oscillation tests were performed on GelMA samples at concentration of 5%, 7.5% and 10% (w/v), in order to assess the effect of GelMA concentration on hydrogel mechanical properties. Rheological measurements were carried out with an AR 1500ex rheometer (TA Instruments, USA) using a cone-plate geometry (diameter= 2cm, truncation= 32um, working gap= 32µm). Mechanical spectra were recorded at both 25°C and 37°C in a constant strain mode, with a deformation of 0.3% and incremental frequencies ranging from 0.01 to 10 Hz. Samples were obtained photo-polymerizing 500 µl of GelMA pre-polymer (1.5% of VA-086) inside a 24-wells plate at 2mW/cm^2.

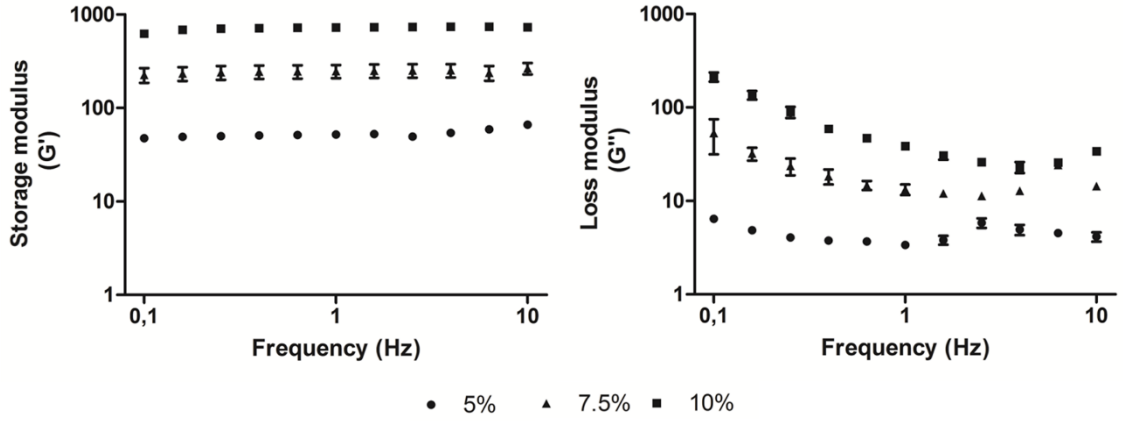

Figure 3.3. *Storage (G') and loss (G'') modulus of cross-linked GelMA in function of frequencies at 37°C. Sample photopolymerization was performed varying gelatin concentration (5%, 7.5%, 10% w/v) while maintaining 1.5% of VA-086 and using a 2 mW/cm^2 irradiance. Axes are in Log scale and error bars identify both positive and negative standard deviation.*

The data in Fig.3.3 represent the average of the storage (G') and loss (G'') modulus with standard deviation obtained at 37°C. In general, storage moduli resulted higher than loss moduli at all concentrations tested, as shown in Fig.3.3. Increasing GelMA concentration from 5% to 10% (w/v), resulted in an increase of both G' and G'', suggesting an enhancement of gel stiffness. Starting from the results of this analysis, we then showed how the storage modulus (G') is independent from the frequency in each condition tested, confirming the chosen range of frequencies corresponds to the linear viscoelastic region (LVR) [37]. We thus compared obtained materials in terms of G'. In particular, results in Fig.3.4 showed the averaged value of G' for the LVR. Increasing GelMA concentration from 5% to 10% (w/v), resulted in a statistically significant increase in G'.

Temperature was finally found not to significantly affect hydrogel mechanical properties, as demonstrated by comparable results achieved at 25°C and 37°C for all the tested conditions (Fig.3.5).

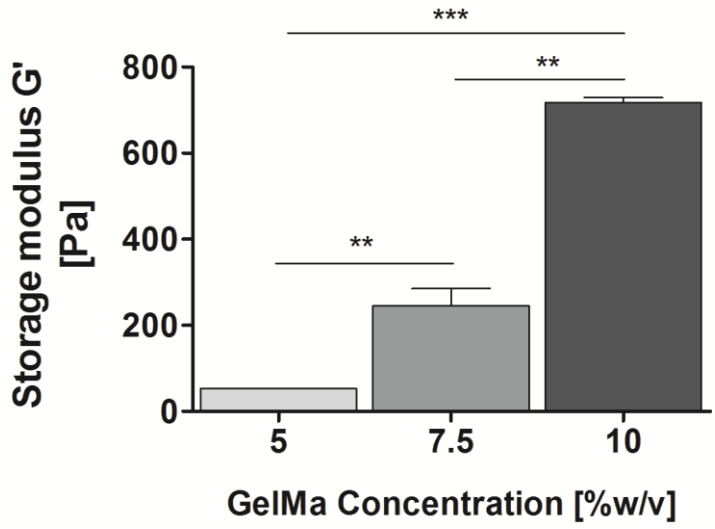

Figure 3.4. *Averaged value of the Storage (G') modulus within the LVR for cross-linked GelMA samples. Sample photopolymerization was performed, varying gelatin concentration (5%, 7.5%, 10% w/v) while maintaining 1.5% of VA-086 and using a 2 mW/cm^2 irradiance. Error bars identify both positive standard deviation (n=3 **p < 0.01. ***p < 0.001).*

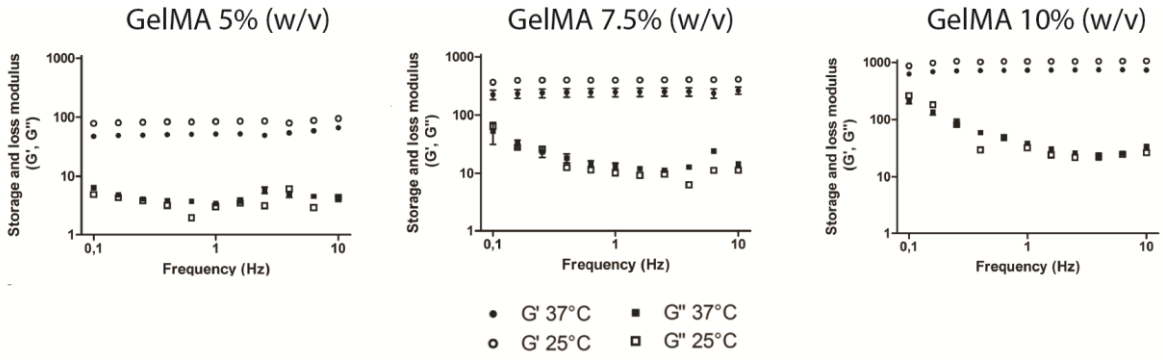

Figure 3.5. *Comparison of storage (G') and loss (G'') modulus of cross-linked GelMA obtained at 37°C and 25°C. Sample photopolymerization was performed varying gelatin concentration (5%, 7.5%, 10% w/v) while maintaining 1.5% of VA-086 and using a 2 mW/cm^2 irradiance. Axes are in Log scale and error bars identify both positive and negative standard deviation.*

3.2.5 Photoinitiator and light source biocompatibility assessment

To assess possible cytotoxic effects of factors used during the VA086-GelMA hydrogel photopolymerization, experiments were carried out on 2D cultures of human bone marrow derived stromal cells (hBM-MSCs) and primary human umbilical vein endothelial cells expressing green fluorescent protein (HUVECs GFP), as detailed in following paragraphs.

Cell sorting and expansion

hBM-MSCs were isolated from bone marrow aspirates obtained from donors undergoing total hip replacement, after written consent. Bone marrow was centrifuged and cells were plated at a density of 1 x 10^5 cells/cm^2 and cultured overnight. Suspended cells were then removed and adherent cells were expanded. hBM-MSCs culture was carried out in complete medium consisting of α-modified Eagle's medium, 10% FBS, 10 mM HEPES, 1 mM sodium pyruvate, 100 U ml^{-1} penicillin, 100 μg ml^{-1} streptomycin and 292 μg ml^{-1} L-glutamine (all GIBCO®) supplemented with 5 ng ml^{-1} FGF2 (Peprotech). When 70-80% confluence was reached, cells were harvested and frozen. At need, cells were then thawed, seeded at lower density (3 x 10^3 cells cm^{-2}) and expanded again. Medium refresh was performed every four days.

Primary human umbilical vein endothelial cells constitutively expressing green fluorescent protein (HUVEC GFP; Children's Hospital, Boston, MA) were expanded in endothelial cells growth medium EGM^{-2} supplemented with the bullet kit which includes: 2% FBS, ascorbic acid, heparin, hydrocortisone and human growth factors (fibroblast, R3-insulin) including vascular endothelial growth factor (all LONZA®). Cells were passaged when 70-80% of confluence was reached and the medium exchange was performed every four days. A standard cell culture incubator, maintaining 5% of CO_2 level and 37°C, was employed for cell culture.

Biocompatibility assays

Biocompatibility assays were performed on 2D cultures of hBM-MSCs and HUVECs GFP. At this purpose, cells were seeded at a density of 3 x 10^3 and 10 x 10^3 cells cm^{-2} for hBM-MSCs and HUVECs GFP, respectively. Samples with identical cell numbers were frozen in order to be used as DNA reference. Right after seeding, cells still in suspension were subjected to different photocrosslinking conditions (as described in Table

3.2). No stimuli were applied in the condition used as control. Independently from the duration of the treatment, cells were allowed to adhere for a period of 4 hours before medium change. After 24 hours under standard culture conditions (chosen to reasonably neglect the cell proliferation as cause of variations in cell number or specific metabolic activity), each sample was analyzed in terms of metabolic activity. In details, cells were incubated for 4 hours in AlamarBlue 10% v/v solution (Invitrogen) and the absorbance was detected using a spectrophotometer at 570 nm (Victor X3, PerkinElmer, Waltham, MA, USA). The number of cells contained in each well was then evaluated. Samples were frozen at -80°C overnight to promote cell lysis and therefore DNA extraction. DNA quantification was performed by means of a commercially available fluorescence based kit, namely CyQUANT® Cell Proliferation Assay (Invitrogen). Working solutions were prepared according to the manufacturer's protocols. Sample fluorescence intensity, detected with a spectrophotometric approach (485/538 nm), was associated to cell DNA content through a calibration curve. The reference samples, containing the number of cells seeded at the initial time point were used to normalize DNA content in each sample and calculate cell number per sample. Finally, for each sample the absorbance value relative to the metabolic activity was normalized to the cell number and used as indicator for the specific cellular metabolic activity.

Table 3.2 summarizes the conditions tested, eliciting from combinations of: PI type, PI exposure time and light source exposure time. For each cell type, five replicates were evaluated for each condition tested (n=5).

Table 3.2 *Scheme of the conditions tested on HUVEC GFP and hBM-MSCs to assess UV light and PI effect on cell viability.*

Condition name	**PI (exposure time)**	**Light Source (exposure time)**	**Photocrosslinking condition tested**
CTRL	-	-	No stimuli
SE VA-086	VA-086 (4hr)	-	PI (short exposure)
LE VA-086	VA-086 (24hr)	-	PI (long exposure)
SE Irg-2959	Irgacure 2959 (4hr)	-	PI (short exposure)
LE Irg-2959	Irgacure 2959 (24hr)	-	PI (long exposure)
UV	-	λ =385nm (3mins)	UV light
UV + VA-086	VA-086 (4hr)	λ =385nm (3mins)	Combined UV light and PI

The effect of long and short exposure to photoinitiator inactive molecules was first analyzed, by comparing the PI used in the presented protocol (VA-086) with the widely used

Irgacure-2959 [34]. Two solutions were prepared by dissolving VA-086 (Wako Chemicals GmbH) and Irgacure 2959 (Ciba Chemicals) in culture medium at 1.5% w/v and 0.05% w/v, respectively (due to different photoinitiator activities) [36]. Solutions were then used to suspend cells at the target concentrations. PI molecule were either removed after 4 hours (short exposure, SE conditions) or left in solution until the end of the experiment (long exposure, LE conditions). Comparable results in terms of cell viability were obtained with both the investigated PIs, as detailed in Fig.3.6a and b. In details, VA-086 in a 30-fold higher mass concentration than Irgacure-2959 (1.5% w/v compared to 0.05% w/v) didn't significantly affect cell viability and specific metabolic activity compared to control conditions after a 4 hours exposure time. A long exposure to VA-086 caused a decrease in HUVEC GFP number, though maintaining a high specific metabolic activity comparable both to control and LE Irgacure conditions. This can however be considered an extreme case, since for the presented protocol the cell exposure to VA-086 is limited to the photopolymerization time (maintained lower than 360 seconds).

Being VA-086 molecules activated at a wavelength range of 365-385nm, the cytocompatibility of a 385nm LED light source was also assessed both individually and in combination with PI molecule. Three minutes exposure to 1W 385nm LED was applied to cells in standard culture medium (UV condition) and cells in 1.5% w/v VA-086 culture medium (UV + VA-086 condition), respectively. The exposure time of 3 minutes was chosen as the mean photopolymerization time required hydrogel photopolymerization. The sole UV irradiation did not cause any significant decrease on cells viability nor metabolic activity after a 3 min exposure time compared to the conditions in absence of irradiation (Fig.3.6a, b, d and e). Finally, treatment with UV and VA-086 (3min; 1.5% w/v) did not show any statistically significant reductions on cell number and metabolic activity compared to the control conditions (Fig.3.6c and f).

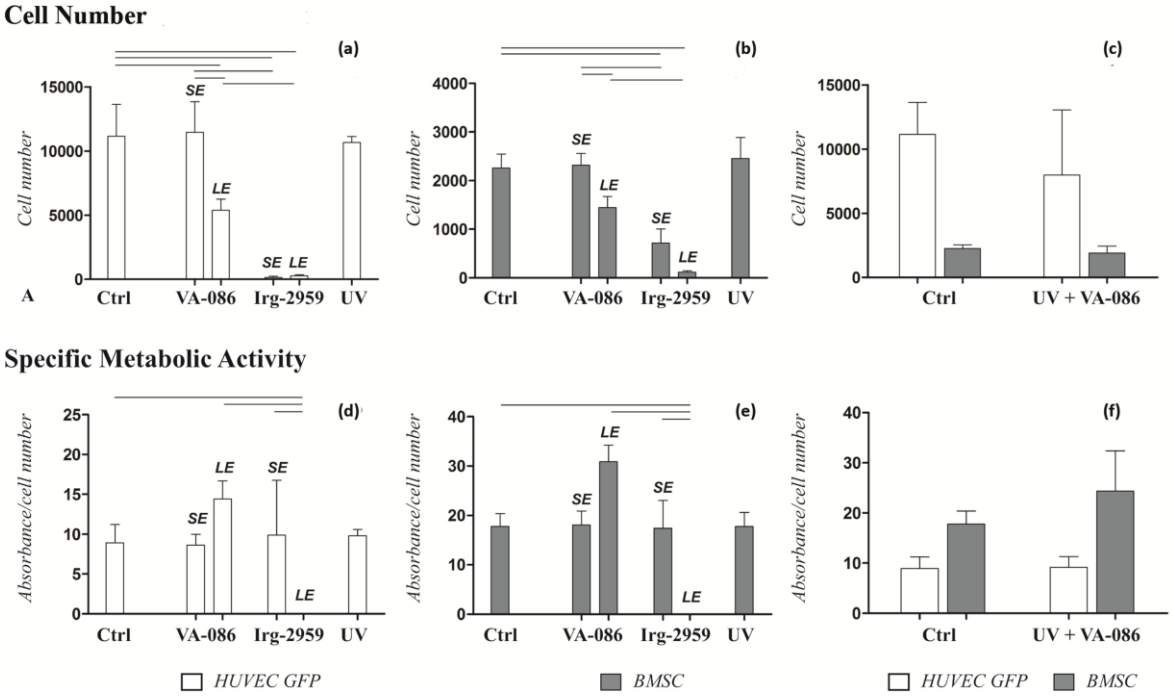

Figure 3.6. *PI and UV cytotoxicity analyses. HUVEC GFP and hBM-MSCs 2D cultures were subjected to different photocrosslinking treatments to assess the cytocompatibility of VA-086-GelMA hydrogels polymerization. Single and combined effects of Short Exposure (SE, 4hr) and Long Exposure (LE, 24hr) inactive PI molecules (VA-086 and Irg-2959) and UV (λ=385nm for 3min) were tested 24 hours after the treatment. For both cell types, the presence of both the PI molecules and the exposure to UV didn't cause any statistically significant reduction in cell number and specific metabolic activity compared to control. A reduction in HUVEC GFP number was detected for VA-086 LE though maintaining a high specific metabolic activity (a, b, d and e). The combination of VA-086 and UV resulted favorable in terms of cell viability demonstrating the biocompatibility of the protocol (c and f). (Error bars: ±SD; n=5. All the reported comparisons are statistically significant for p<0.05).*

3.3 3D cell-laden VA086-GelMA hydrogels: macroscale models

In the next paragraphs, the previously characterized VA-086-GelMA hydrogel is exploited for the generation macroscale models for 3D cell culturing. As a preliminary biological validation, hBM-MSCs behavior when cultured within VA-086-GelMA hydrogels is first reported (3.3.1). Moreover, the establishment of hBM-MSCs/HUVECs 3D macroscale co-culture models is introduced (3.3.2).

3.3.1 Cell embedding and 3D culture

Biological validations were carried out to assess the influence of concentration of GelMA on 3D cellular behavior. hBM-MSCs were thus embedded within VA-086-GelMA hydrogels at different concentrations (5%, 7.5% and 10% w/v), and cultured up to seven days. In details, the methacrylated gelatin was completely dissolved in a filtered 1.5% (w/v) PI solution, subsequently used to resuspend previously trypsinized hBM-MSCs at a final concentration of 2 x 10^6 cells/ml. The photopolymerization reaction was thus carried out as previously described maintaining sterile conditions, by irradiating the sample for 3 minutes with a LED irradiance of 2 mW/cm^2. Samples containing the same cell numbers were produced and frozen to be subsequently used as DNA references. The obtained cell-laden samples were incubated under standard culture conditions and cultured up to seven days, while refreshing media every 3 days. Cell metabolic activity and proliferation inside 3D hydrogels were then evaluated after 3 and 7 days in culture. In details, at the defined time points, each sample was washed in PBS, placed in a new well, and incubated at 37°C in 10% v/v AlamarBlue solution (Invitrogen Corporation, Isbad, CA, USA). After 4 hours, the absorbance of the resulting solution at 570 nm was measured using a spectrophotometer (Victor X3, PerkinElmer, Waltham, MA, USA). The DNA in each sample was then evaluated by means of the CyQUANT cell proliferation assay (Invitrogen Corporation, Isbad, CA, USA). Samples were frozen at -80°C overnight and digested for 16 hours at 60°C with 250 µL of ProteinaseK (Sigma-Aldrich Corporation, St. Louis, Missouri, USA). After digestion, 5 µl of the sample and 195 µl of the working solution, previously prepared according to the manufacturer's protocols, were placed into a 96 black multiwall plate. Sample fluorescence intensity was detected with a spectrophotometer at 485/538 nm and subsequently related to cell DNA content through a calibration curve, as previously described. The reference samples were used to normalize DNA content in each sample.

Finally, for each sample the metabolic activity value was normalized to the DNA content to assess the specific cellular metabolic activity.

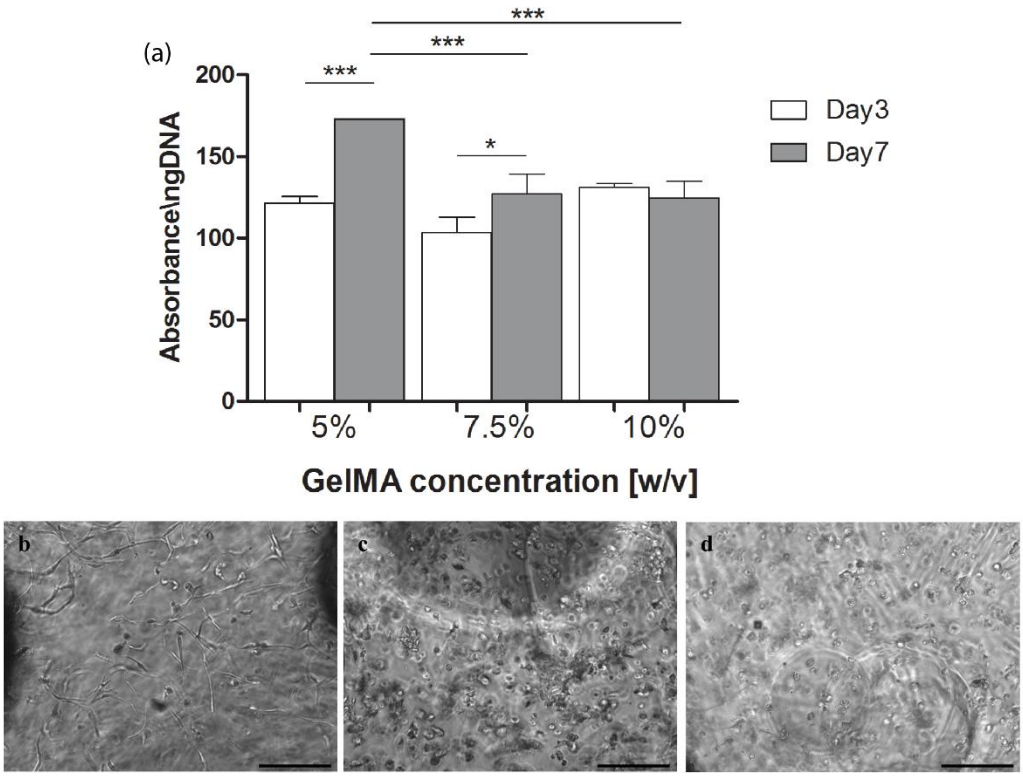

Figure 3.7. *Specific metabolic activity of hBM-MSCs cultured up to 7 days within GelMA at different concentrations (a). Cell laden GelMA samples were cross-linked with 2 mW/cm2 irradiance in the presence of 1.5% VA-086. Cell morphology after 7 days of culture was also assessed. hBM-MSCS embedded within 5% GelMA appeared more elongated (b), while 7.5% and 10% gelatin sample showed rounded cells (c, d) (Image scale bar= 200µm).*

After 3 days in culture, hBM-MSCs showed similar specific metabolic activity for all the conditions tested (Fig.3.7a). After 7 days in culture, however, cells showed a higher cell metabolic activity as compared to the previous time point. In particular, metabolic activity of both 5% and 7.5% (w/v) GelMA samples had a statistically significant enhancement compared to corresponding samples at day 3. Concerning cell morphology, after 7 days of culture, hBM-MSCs appeared more elongated in GelMA at 5% (w/v), while almost rounded in both the 7.5% and 10% (w/v) ones (Fig.3.7b).

3.3.2 hBM-MSCs/HUVECs 3D macroscale co-culture model

To evaluate cell elongation and interaction within gels with different mechanical properties, co-cultures of hBM-MSCs and HUVECs GFP were established for all GelMA concentrations (5%, 7.5% and 10% w/v).

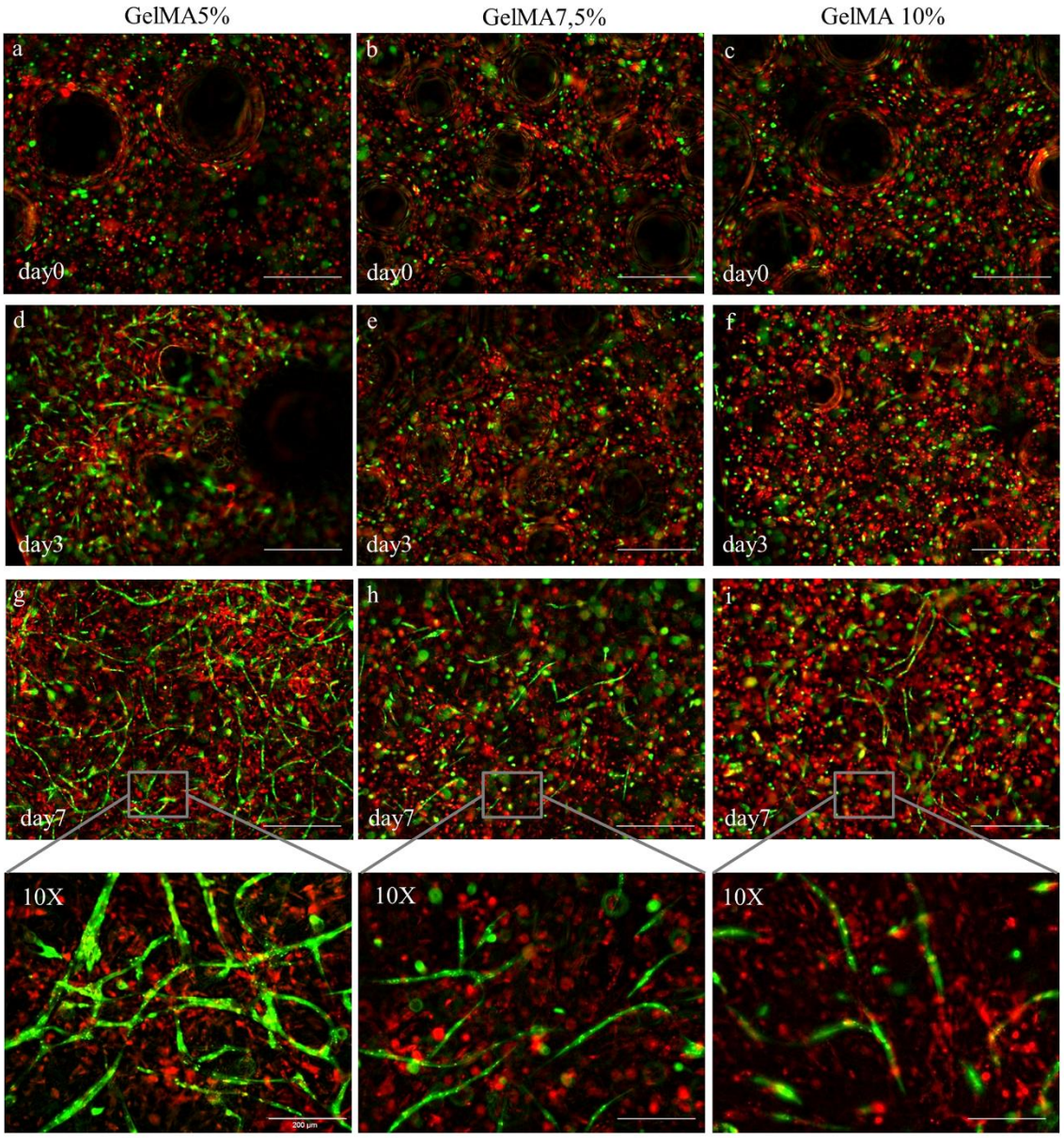

Figure 3.8. *Cell behaviour when co-cultured within GelMA hydrogels. HUVECs GFP (green) and hBM-MSCs (red) were co-cultured up to seven days within 5%, 7.5% and 10% (w/v) GelMA samples. Immediately after embedding, cells appeared rounded in all samples (a-c). After 3 days of culture HUVECs started to interact within 5% (w/v) gel (d) while maintained a rounded-shape in 7.5% and 10% (w/v) hydrogel samples (e-f). After 7 days, within 5% (w/v) GelMA samples, HUVECs developed a network-like structure (g), whereas in 7.5% and 10% (w/v) GelMA, HUVECs appeared sparsely connected and hBM-MSCs remained rounded (h-i). Black and cell free regions resulted from N2 gas release during photo-polymerization (Image scale bar= 500 µm (a-i) and 200µm for 10X magnifications).*

In details, hBM-MSCs were made fluorescent through a 10 minutes incubation in culture medium enriched with 5µl/ml of Vibrant (Invitrogen Corporation, Isbad, CA, USA). Cells were resuspended at a final concentration of 3 x 10^6 cells/ml in the pre-polymer solution, maintaining an hBM-MSCs/HUVECs ratio of 1:1. The polymerization was performed as previously described and samples with either only hBM-MSCs or HUVECs were established as controls. All the cell-laden samples were cultured in HUVECs culture medium and maintained in standard culture conditions for up to seven days, while medium change was performed every 3 days.

After 3 days in culture, HUVECs started to elongate within the 5% (w/v) GelMA (Fig. 3.8d), while maintaining a more round-shape in both 7.5% and 10% (w/v) GelMA samples (Fig.3.8e and f). The maximum cell spreading was reached after 7 days of culture in 5% GelMA samples (Fig.3.8g), in which the formation of a fully developed HUVECs network was detected. In the remaining gels (7.5% and 10% w/v), HUVECs appeared sparsely connected and did not form any network-like structure and hBM-MSCs remained almost rounded for the whole culture period (Fig.3.8h and i). Culturing hBM-MSCs and HUVECs apart, on the contrary, resulted in isolated and round-shaped cells within all three GelMA concentrations tested and for all the seven days of culture (Fig.3.9).

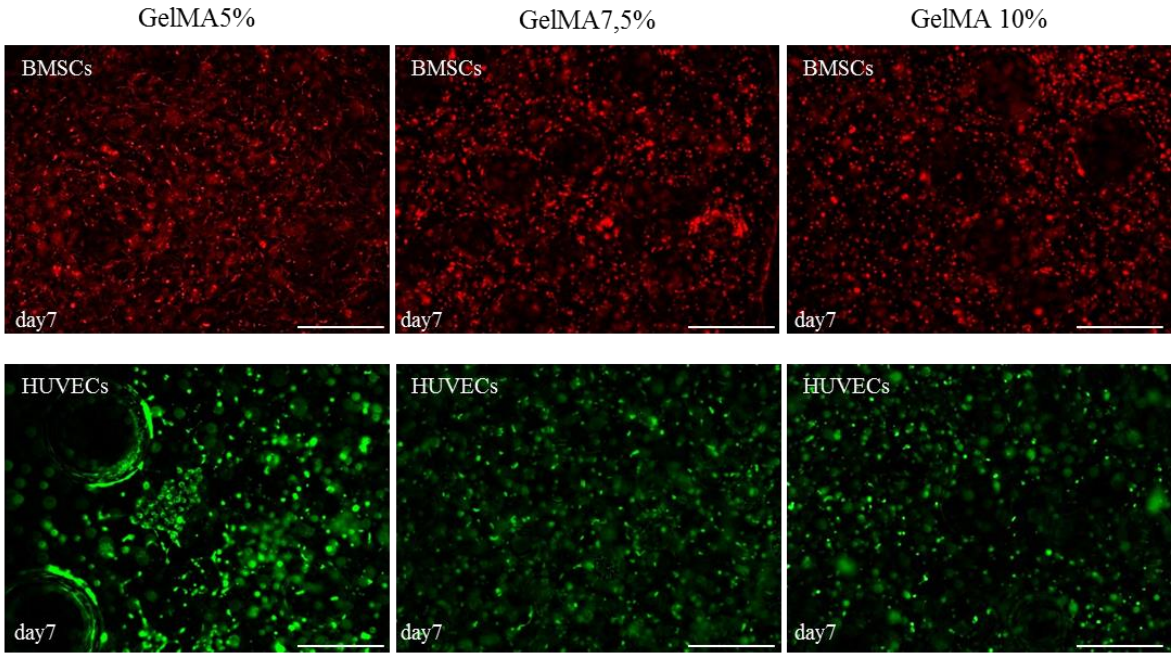

Figure 3.9. *Cell behaviour within GelMA hydrogel established as co-culture control. HUVECs GFP and hBM-MSCs (red) were cultured up to seven days within 5%, 7.5% and 10% (w/v) GelMA samples. After 7 days, both cell types appeared almost rounded within all GelMA samples. (Image scale bar= 500 µm).*

3.4 3D cell-laden VA086-GelMA micropatterns: an innovative photo-mold-patterning (PMP) protocol

A novel photo-mold-patterning (PMP) protocol for hydrogel micro-structuring is introduced in these paragraphs, based on the previously characterized VA-086-GelMA hydrogel (Fig.3.10). As described in paragraph 3.4.1, the PMP protocol consists of four main steps: 1) a PDMS microfluidic chip with geometrically defined micropatterns is placed against a glass substrate and used as mold; 2) a cell-laden pre-polymer light-sensitive solution is loaded within the microchannels; 3) UVA light is provided through the PDMS layer until complete crosslinking; 4) once the stamp is removed, cell-laden microstructures are obtained on the glass substrate. In the next paragraphs, a complete characterization of the PMP protocol is reported. First, its versatility and reliability in generating differently shaped and multi-height micropatterns is showed (3.4.2). Then, the ability of embedding cells defining 3D uniform distributions is demonstrated (3.4.3). Finally, the establishment of spatially controlled 3D hBM-MSCs and HUVECs GFP mono- (3.4.4) and co-cultures (3.4.5) is detailed.

3.4.1 Photo-Mold Patterning (PMP) protocol

Layouts of desired hydrogel micropatterns were designed through a CAD software (AutoCAD, Autodesk Inc.) and the corresponding master molds were realized through standard photolithography techniques [38]. Stamps were produced by replica molding on the master molds by casting PDMS in a ratio 10:1 w/w (pre-polymer to curing agent), degassing and curing at 80°C for 3 hours. The PDMS stamps were trimmed so to show microchannels openings on their lateral sides and subsequently air-plasma treated to induce surface hydrophilicity. PMP devices were finally assembled by placing the stamps against histology glass slides, which were previously treated with 3-(trimethoxysilyl) propyl methacrylate (TMSPMA) (Sigma- Aldrich®) to enhance hydrogel adhesion [39].

10% w/v VA-086-GelMA prepolymer solution was prepared as previously described and used to suspend cells at the desired final concentration. In addition to VA-086-GelMA hydrogel, polyethylen glycol diacrylate (PEGDA, Sigma- Aldrich®) was also considered as a commercially available alternative to assess the versatility of the proposed protocol. Through a standard pipettor, 2.5 µl of the cell-laden pre-polymer solution were placed in contact with a PMP device opening and allowed to fill the corresponding microchannel

driven by capillary forces. Once completely filled, the sample was irradiated for 3 minutes with a LED irradiance of 2 mW/cm^2. Subsequently the PDMS mold was removed leaving the hydrogel micropattern adherent on the glass slide. The sequence of operations for the PMP protocol is depicted in Fig.3.10.

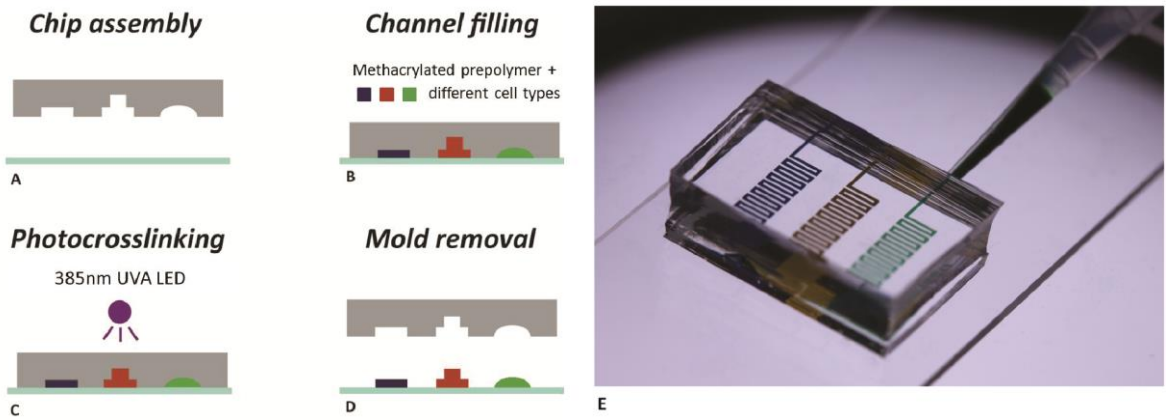

Figure 3.10. *Photo-Mold Patterning (PMP) protocol. The PDMS microfluidic mold is placed against a 3-(trimethoxysilyl) propyl methacrylate (TMSPMA) treated slide (a). Hydrogel prepolymer is injected into the channels (b), and the photopolymerization is achieved using a commercial LED emitting at 385nm (c). Upon PDMS removal, the 3D patterns are revealed on the glass substrate (d). An example of PMP is reported, where three mold channels were independently filled with different colors (e).*

3.4.2 Evaluation of PMP versatility and reliability: development of differently shaped and multi-height hydrogel micropatterns

To evaluate the PMP ability to reliably achieve differently shaped micropatterns, two chip layouts were first considered for both PEGDA and GelMA hydrogels. In particular, a straight channel and a serpentine configuration were conceived, both having channel width of 250µm and height of 80µm. An exposure time of 3 minutes to UVA LED, combined with a 1.5% w/v PI concentration allowed to achieve highly defined micropatterns, narrowly replicating 250 µm width and 80 µm height PDMS mold features for both the configurations (Fig.3.11). Moreover, the PMP protocol was demonstrated to be applicable to both the materials tested, leading to comparable results in terms of 3D geometry replication. As shown in Fig.3.11e and f, even using a non-collimated light source, the cross sections obtained from both PEGDA and GelMA resulted squared, replicating the PDMS channels layout without any magnification of patterns width [31].

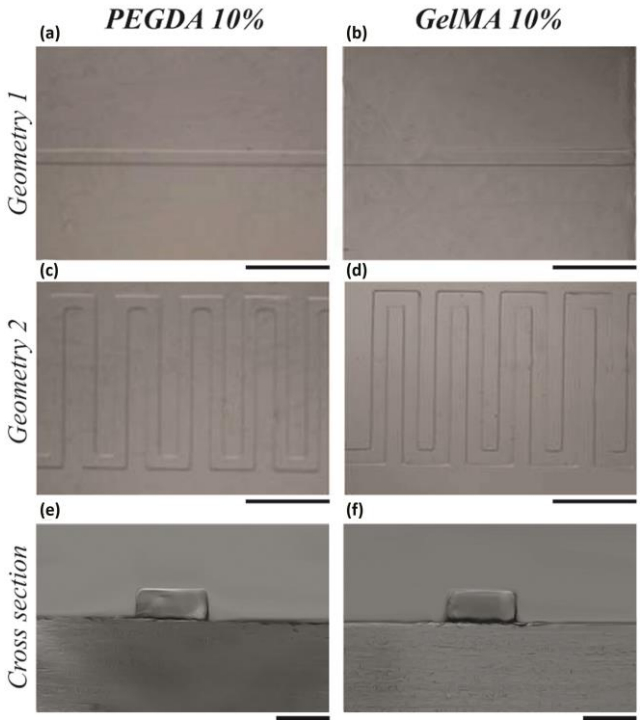

Figure 3.11. *3D replication of different geometries through PMP. Phase images of hydrogels obtained from 10% w/v PEGDA (a, c and e) and 10% w/v GelMA (b, d and f) polymer precursors upon a 3 minutes UVA exposure in the presence of 1.5%w/v VA-086. PMP allowed to achieve micrometrically defined patterns, narrowly replicating 250 µm width and 80 µm height mold features for both the configurations and the materials tested (a-d; scale bars: 1000 µm). The hydrogel cross sections obtained from both PEGDA and GelMA resulted squared, exactly reproducing the PDMS channel lateral layouts (e-f; scale bars: 200 µm).*

Moreover, the potentiality of PMP protocol to fabricate microstructures characterized by multiple heights within a single step procedure was assessed. A mold layout containing 500 µm wide channels with multiple height steps (210 µm and 60 µm, respectively) was realized through PDMS replica molding from a laser ablated polyester film/glass master mold [40]. Exploiting this PDMS mold as geometrical constraint, VA-086-GelMA micropatterns were obtained within a 3 minutes exposure to a UVA LED, as previously described. The obtained structures were analyzed by means of a stereomicroscope and the results are reported in Fig.3.12 (details of the two cross-sections are depicted in the insets a and b).

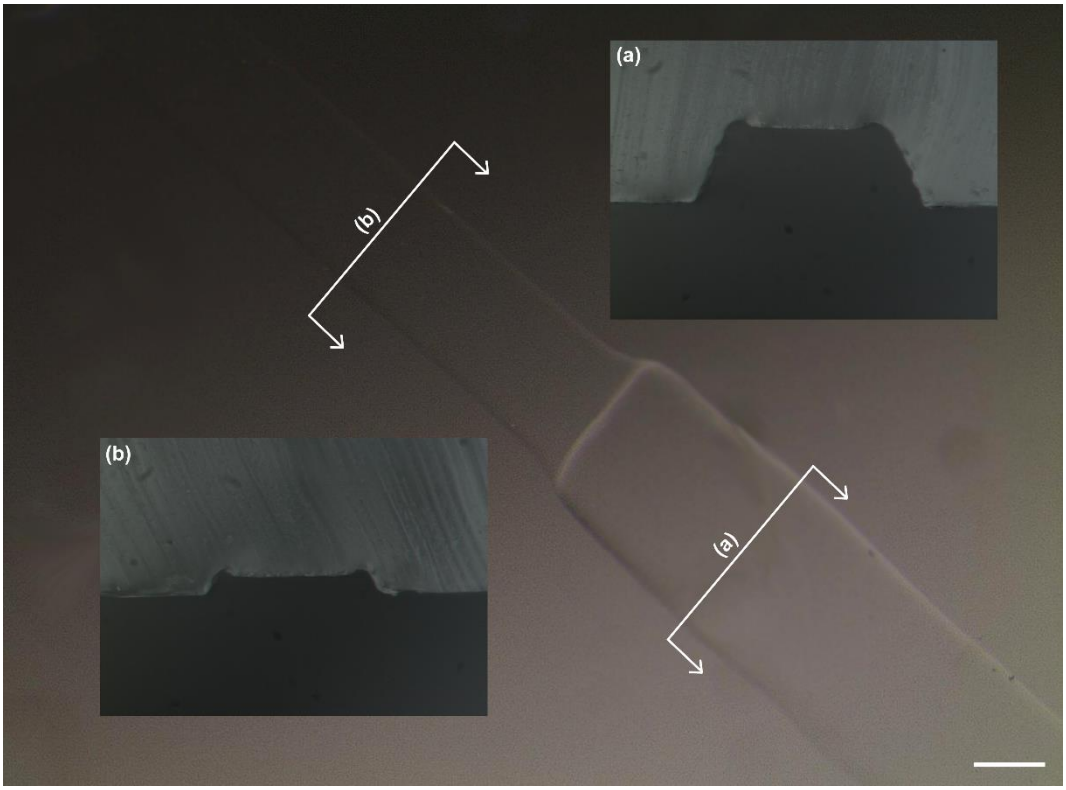

Figure 3.12. *3D replication of a multiple heights channel through PMP. Stero microscope images of hydrogels obtained from 10% w/v GelMA polymer precursors upon a 3 minutes UVA exposure in the presence of 1.5%w/v VA-086. The PDMS mold used as geometrical constrains have two different cross sections, 210 µm (a) and 60 µm (b) high respectively. Exploiting the possibility to have multiple heights features within the same mold, PMP allowed achieving different feature sizes within a single step procedure. (Scale bars: 200 µm).*

3.4.3 Cell embedding within micropatterns: a 3D distribution analysis

The potentiality of PMP protocol in achieving a 3D uniform cellular dispersion was assessed. In details, HUVECs GFP were encapsulated within VA-086-GelMA through the PMP protocol, and the resulting micropatterns were analyzed in terms of 3D cell distribution. Cells were trypsinized, counted and resuspended at different initial concentrations (1, 5 and 10 x 10^6 cells/ml) into 10% w/v GelMA containing 1.5% w/v VA-086 prepolymer solution and the PMP protocol was performed as previously described leading to cell-laden micropatterns formation. Specifically, the range of initial cell densities were considered in the perspective to obtain constructs targeting tissues with different cellularity. Immediately after the photopolymerization, micropatterns were treated sequentially with 4% paraformaldehyde and 0.1% Triton-X to fix and permeabilize cells, followed by DAPI (Invitrogen) to fluorescently stain cell nuclei. Samples were thus mounted on slides and observed by fluorescent confocal microscopy (Leica TCS SP8). The 3D position of cell nuclei was analyzed with a semi-automated object 3D counter plugin of the NIH ImageJ

software, using an intensity-based algorithm and verified in 10% microscope fields by manual counts. To assess the cell distribution along the channel length, three equidistant channel areas (l=1mm) were chosen in correspondence to the inlet, center and outlet regions. Each area was then divided along its width and height in ten (w=25µm) and four (h=20µm) bands, respectively. The number of cells present in each region of interest was evaluated to quantify the cell distribution in both lateral and vertical channel dimensions. For each cell concentration tested, three samples of the straight channel configuration were considered (n=3).

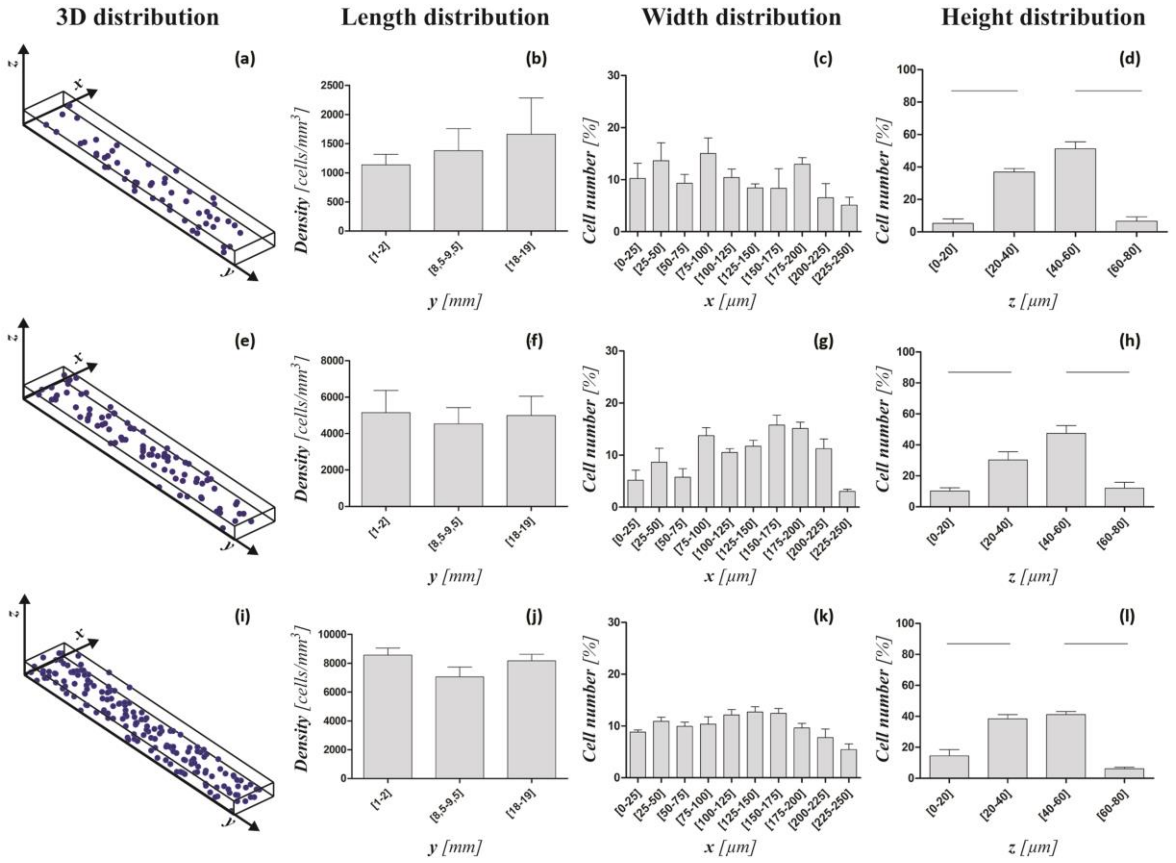

Figure 3.13. *3D cells spatial distribution. Positions of cell nuclei geometrical centers at densities of 1, 5 and 10 x 106 cell ml-1 were plotted from data obtained by analyzing confocal images of the DAPI stained cell-laden micropatterns at day 0. Cells were uniformly distributed along the channels length (b, f and j) and width (c, g and k). While a higher cell density was detected in the two central bands (l=20µm) of the channels height (d, h and l), the overall cell distribution resulted 3D uniform within the micropatterns (a, e and i). (Error bars: ±SD; n=3. All the reported comparisons are statistically significant for p<0.05).*

The desired cellular microtopography, defined by the pattern geometry, was achieved resulting in a uniform distribution of HUVECs GFP dispersed along straight GelMA micropatterns, as shown by the geometrical center positions of the cell nuclei (Fig.3.13a, e and i). For all the concentrations tested, cells preserved a tridimensional distribution along

the whole channel after the photopolymerization, resulting homogenously dispersed within both the gel length (Fig.3.13b, f and j) and width (Fig.3.13c, g and k). The analysis of cells distribution along the microgels height (Fig.3.13d, h and l) resulted in a statistically significant higher cell density in the two central bands (20µm each) of the channels ($p<0.05$), probably due to the flow dynamics during the solution injection.

3.4.4 Cell culture within VA-086-GelMA hydrogel micropatterns

HUVECs GFP (Fig.3.14a and c) and hBM-MSCs (Fig.3.14b and d) were embedded in 3D VA-086-GelMA micropatterns at $10x10^6$ and $3x10^6$ cells/ml, respectively, and their behavior was recorded over a 7 days culture period [22,28].

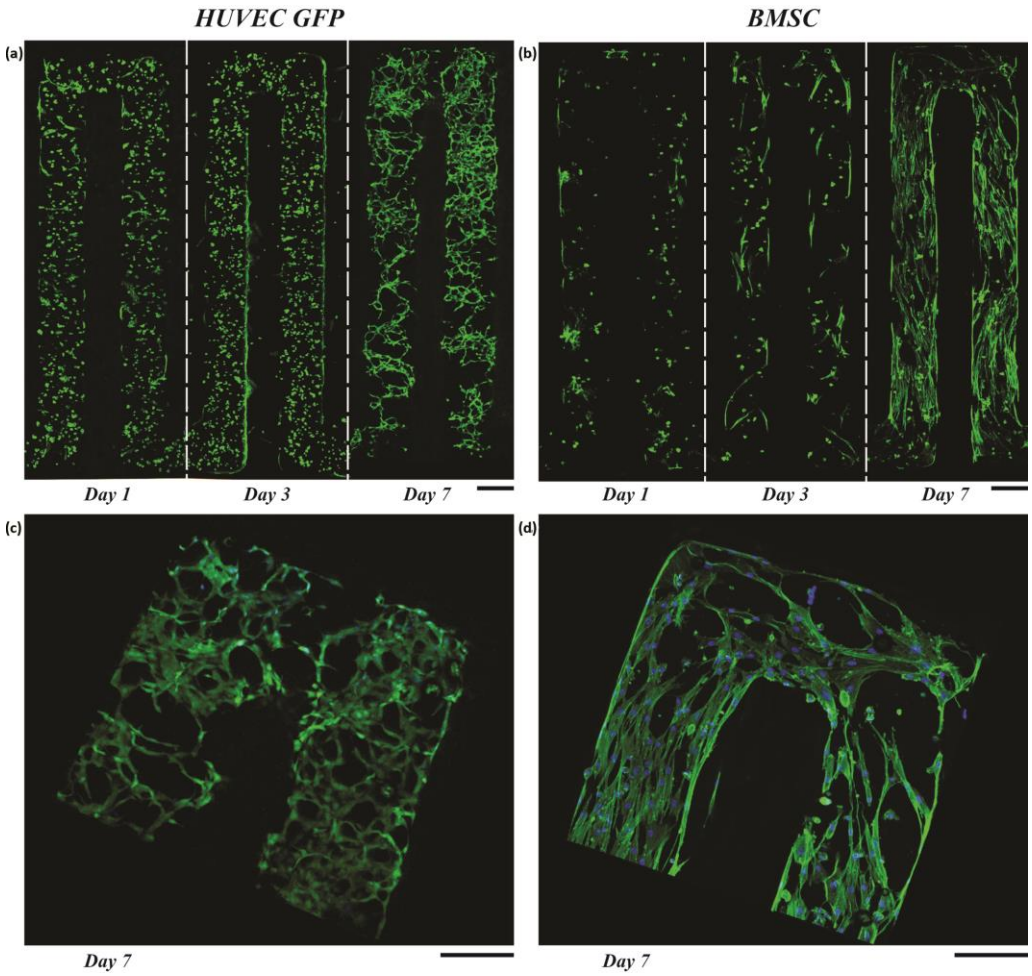

Figure 3.14 *Cell behavior within hydrogel micropatterns. HUVEC GFP (a and c) and hBM-MSC (b and d) were embedded within GelMA micropatterned hydrogels by PMP and cultured for 7 days. (a and b) The day 1 cell rounded morphology gave way at day 3 to a migration of both cell types from the center to the surface of the patterns, reaching the maximum cell spreading by day 7 of culture. (Representative images of F-actin stained samples; z step=5.48 µm. Scale bar =250 µm.). At day 7, HUVEC GFP created network-like structures preferentially near the outer surface of the hydrogel (c), while hBM-MSCs showed a tendency to align along the main axis of the microstructures (d). (Representative F-actin/DAPI stained 3D projections; z=80.22 µm. Scale bar =250 µm.).*

This biological validation was only carried on VA-086-GelMA, being PEGDA not suitable for cell adhesion in its native form [41]. For this purpose, cells were trypsinized, counted and resuspended into 10% w/v GelMA containing 1.5% w/v VA-086 prepolymer solution and the PMP protocol was performed as previously described. The glass slides containing cell-laden microgels were gently washed with PBS to remove possible unreacted PI molecules, incubated under standard culture conditions and cell behavior was evaluated at days 1, 3 and 7. For each time point, the micropatterns were treated sequentially with 4% paraformaldehyde and 0.1% Triton-X to fix and permeabilize cells, followed by phalloidin (BODIPY® 558/568 phalloidin, Invitrogen) and DAPI (Invitrogen) to fluorescently stain respectively filamentous F-actin and cell nuclei. Samples were thus mounted on slides and observed by fluorescent confocal microscopy (Leica TCS SP8).

After 24 h of culture both cell types started to actively elongate within VA-086-GelMA hydrogels. At day 3, both types of cells started to migrate from the center to the surface of micropatterns. The maximum cell spreading was reached by day 7 of culture (Fig.3.14c and d), when the cells completely covered the surface of micropatterns. While HUVEC GFP cells created network-like structures, preferentially near the outer surface of the hydrogel, hBM-MSCs showed a tendency to align along the main axis of the microstructures.

3.4.5 PMP as microscale approach for defining co-culture models with highly controlled microarchitectures

The potentiality of PMP protocol to spatially organize different cell types by means of a single exposure step was first assessed. Differently shaped PDMS molds were thus developed through replica molding from laser ablated polyester film/glass master molds [40]. Designed layouts allowed for the simultaneous injection of different cell-laden pre-polymer solutions within separated features of the same mold. In details, hBM-MSCs were divided in two groups, each labeled either through red or green Vybrant (Molecular Probes, V-22889). GelMA micropatterns embedding labeled hBM-MSCs ($10x10^6$ cells ml^{-1}) were obtained as previously described. The samples were immediately analyzed by means of fluorescent confocal microscopy (Leica TCS SP8). Fig.3.15a and b show two eliciting 3D spatially organized microarchitectures in which two cell types (labeled in this case) are embedded in different areas, separated but close to each other thus allowing interactions detected after 5 days in culture (Fig.3.15b-f). This single step procedure can thus be used as

flexible tool to combine different cell types (and potentially materials), creating more complex geometries.

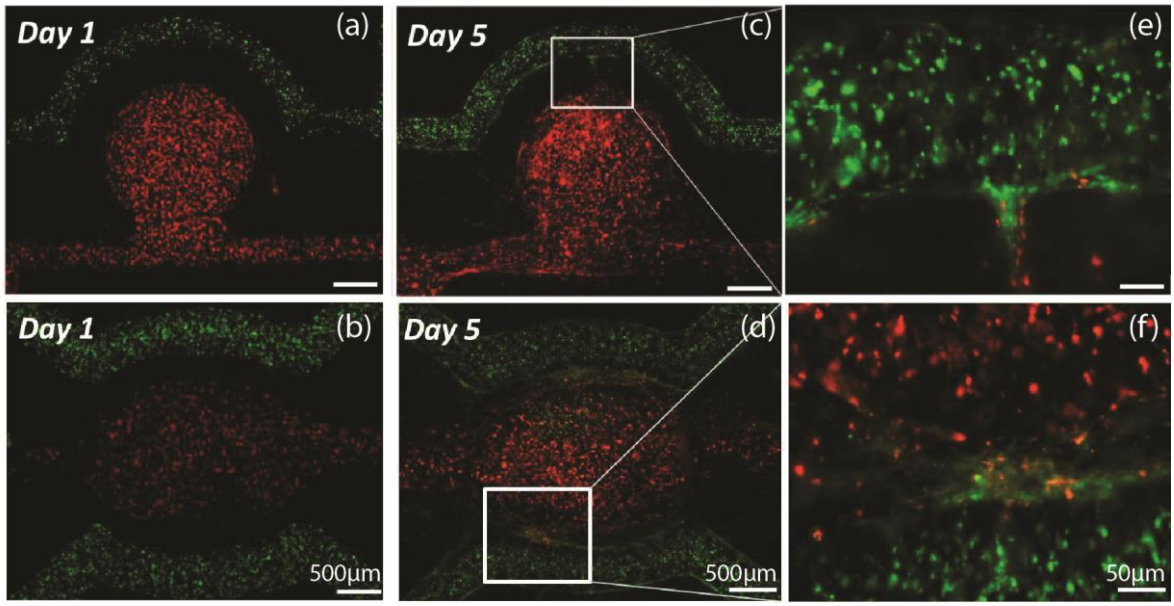

Figure 3.15 *Red and green labeled hBM-MSCs embedded in VA-086-GelMA 3D spatially organized microarchitectures (a and b). Interactions between cells embedded in different areas of microstructures have been showed after 5 days of culture (c-f).*

PMP was then exploited for fast and controlled multi-cell types embedding within multilayered 3D micropatterns. In details, multi-layered cellular structures were fabricated embedding in two consecutive steps differently labeled hBM-MSCs within microchannels featuring increasing dimensions (Fig.3.16).

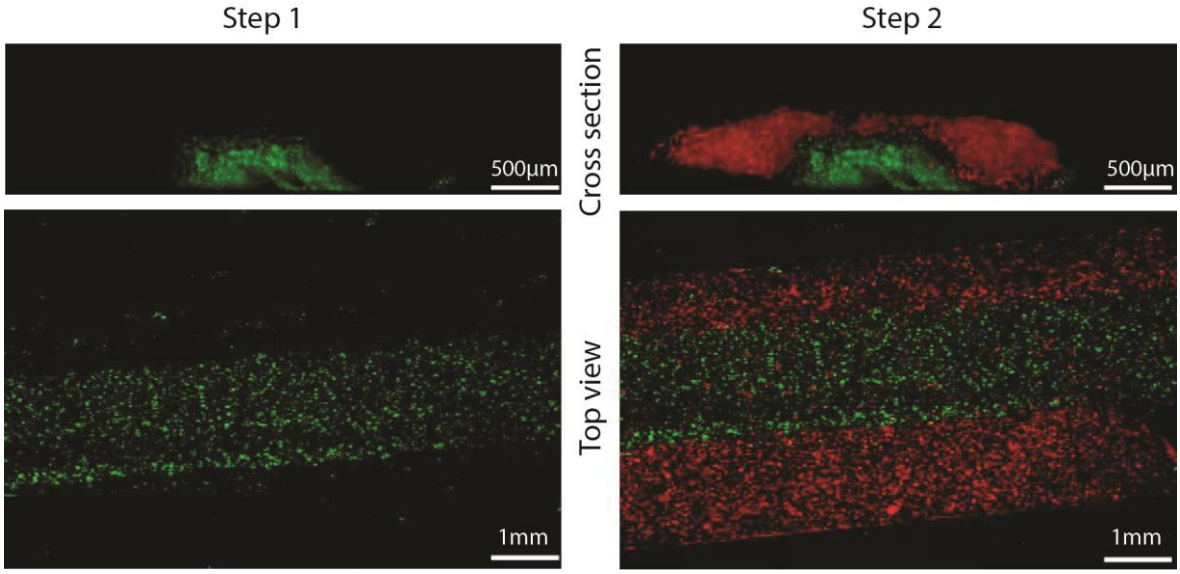

Figure 3.16. *Cross section and top view of a microchannel defined by two concentric VA-086-GelMA hydrogel layers laden with red and green labeled hBM-MSCs.*

3.5 Discussion

In the last decade, advances in microtechnologies together with the definition of novel biomaterial compositions led to the development of microscale approaches for tailoring *in vitro* the microarchitecture around cells [8,42]. Three are the main requirements for the realization of 3D microstructured cell-populated constructs: *i)* the cytocompatibility of the fabrication/embedding protocol, *ii)* the ability to control the microenvironment in size and shape over the three dimensions, and *iii)* the possibility to distribute cells in a uniform and controlled fashion within the microenvironment. Several attempts for matching these requisites have been reported [5,43-45]. Lately, the most promising approaches tried to combine the high spatial resolution achievable through photo- and soft- lithographic techniques with the unique affinity of hydrogels with several cell embedding approaches [12,22,28,46].

Within this context, we presented an innovative photo-mold-patterning (PMP) protocol aiming to meet biocompatibility and microarchitectural control requirements in a simple and cost effective way. The PMP technique enables for fast and controlled cell embedding within 3D micropatterns through the exploitation of standard PDMS soft lithography combined with an innovative low toxicity hydrogel photopolymerization approach. In details, a commercially available UVA LED (emitting peak at 385nm), exhibiting negligible cytotoxicity effects, was employed as controlled light source to photopolymerize methacrylate gelatin hydrogels in combination with the photoinitiator (PI) molecule VA-086, highly activated at this wavelength [47]. As previously shown [48], cell damages from UV light exposure strictly depends on source intensity and emitting spectrum. While short UV wavelengths (UVB range) consistently damage cells even at low energy levels (in the order of mJ/cm^2), the shifting to longer wavelengths dramatically reduces the incidence of cell death, as further demonstrated in the reported 2D cell biocompatibility analyses. Moreover, the VA-086 has been here demonstrated to minimally affect cell viability both in its radical and inactive forms, making it a promising alternative to the widely used Irgacure 2959, highly activated at shorter light wavelengths (adsorption peak around 320nm) [35].

The photo-crosslinking process for fabricating cell-laden VA-086-GelMA-based hydrogels was first deeply characterized at the macroscale, showing the influence of polymer concentration and light irradiance directly on both mechanical and biomimetic properties of resulting matrices.

The presented photopolymerization protocol was demonstrated to be highly effective allowing obtaining fully cross-linked samples within tens to hundreds of seconds. All combinations used of polymer concentrations, VA-086 contents and light irradiance yielded to photo-crosslinking times lower than 360s. These short cross-linking times, indeed, resulted compatible with the cell embedding procedure, avoiding cells from settling down. Moreover, while increasing LED irradiance resulted in lower cross-linking times, it was also showed to enhance the hydrogel porosity by means of N_2 gas release as a result of UV radical induction [49]. Starting from this characterization, an optimal photopolymerization protocol was defined, fixing the LED irradiance at 2mW/cm^2 and the PI concentration at 1.5% w/v, fulfilling both the biocompatibility and the matrix homogeneity requirements for all conditions tested. In details, samples were polymerized for 3 minutes subjecting cells to a total irradiation dose of about 600 mJ/cm^2, well below a level previously demonstrated as not toxic to cells, i.e. 1800 mJ/cm^2 [47,49]. As a remarkable advantage, the entire process was easily performed under sterile conditions by placing the samples within standard Petri dishes, thus taking advantage from the optical transparency of polystyrene to UVA.

The rheological characterization of GelMA hydrogels further showed how the increase of gelatin concentration directly increases sample stiffness, as a consequence of the availability of more cross-links per unit volume, in agreement with previously reported data [32]. This correlation between crosslinking parameters and mechanical behaviour suggested the potentiality of the presented protocol to easily tune the stiffness of the cell-laden matrix according to the required application.

Successful hBM-MSCs embedding within VA-086-GelMA samples revealed the potentiality of our protocol to obtain and culture biocompatible cell-laden hydrogels up to seven days supporting cell proliferation and spreading depending on mechanical properties. Cell behavior and viability results, after seven days in culture, showed how specific cell metabolic activity and viability varied inversely with gel concentration: hBM-MSCs resulted more viable and metabolically active, and appeared more stretched after seven days in culture in 5% w/v GelMA, as compared to 7.5% and 10% w/v samples. This finding suggests that mechanical properties characterizing the lower hydrogel concentration better allowed this cell type to remodel and degrade the matrix. The presented combination of methacrylated gelatin, VA-086 photoinitiator molecule and UVA LED source was also investigated for generating multi-cell types models, co-culturing hBM-MSCs and HUVECs.

Results obtained within the softer GelMA hydrogels showed to enhance the interactions between hBM-MSCs and HUVECs when co-cultured, promoting the formation of well-established HUVECs network-like structures. In the same conditions, neither HUVECs nor hBM-MSCs cultured alone were able to remodel the surrounding matrix at comparable levels, suggesting that the presented material could be considered a promising co-culturing model for further studies on the interplay between these two cell populations.

Based on the macroscale characterization of the presented biomaterial, we defined a method to homogeneously embed and culture primary cells within 3D VA-086-GelMA hydrogels micropatterns exploiting the PMP protocol. The PMP method was in details tested both on a continuous cell line (HUVEC GFP) and primary hBM-MSCs demonstrating the possibility to embed viable cells also within 3D microgels, creating biocompatible and favorable environments for cell proliferation and spreading, while precisely tailoring the microarchitecture around them.

The ability of PMP protocol to replicate defined microarchitectures through hydrogel photopolymerization was first demonstrated. Indeed, 3D structures obtained by PMP presented a geometrical resolution comparable to that offered by traditional mold patterning methods [22,23]. In fact, the PMP protocol exploits UVA-transparent PDMS microstructured stamps as physical molds for cell-laden prepolymer. This leads to micrometrically resolved GelMA structures guaranteeing the desired 3D shape replication both in terms of layout and cross section independently from the light beam collimation [26]. This was also demonstrated starting from a commercially available synthetic prepolymer type (PEGDA) showing how the PMP protocol represents a versatile tool for controlling the 3D geometry of different methacrylated hydrogels in an effective and low cost way.

Well-established multilayer photo- and soft- lithographic techniques expand the range of PMP feasible geometries, allowing to obtain multiple shapes and heights within the same mold. PMP has also been showed to be a flexible and versatile tool to combine different cells (and potentially materials) within multi-shape and muti-layer features, making it a simple tool to design and pattern complex 3D geometries with the aim of replicating *in vivo*-like microarchitectures.

Moreover, the exploitation of a light-initiated polymerization approach enables for a fast cell immobilization within the matrices, generating micrometrically resolved hydrogel patterns upon a 3 minutes exposure to a UVA LED source. Such exposure period was

compatible with the achievement of uniform 3D cell dispersions within the structures for three encapsulation cell concentrations considered. Shorter crosslinking periods (within tens of seconds) could be achieved by exposing the prepolymer to higher light intensities. However, we noticed that at higher optical powers, bubbles were generating within the microstructures thus compromising either the pattern spatial definition or its integrity.

As a remarkable advantage, the presented PMP protocol needs a minimal quantity of reagents and cells for micropatterns formation, being only required the amount of prepolymer to completely fill the mold channels. This advantage becomes more relevant in case two or more cell types and/or materials are considered as fillers of different features of the same mold. It is worth noticing that to the best of our knowledge this is the first time photopolymerizable cell-laden micropatterns are obtained through the use of a LED as light source. Hence, PMP represents a valid tool to create homogenously populated cell-laden constructs able to spatially recapitulate the native 3D cell-cell and cell-ECM interactions.

Conclusive remarks

In the present chapter, a highly biocompatible photo-crosslinking process to obtain uniform 3D cell-laden GelMA hydrogels was fully characterized, demonstrating good potentialities both at the macroscale and at the microscale.

First, we systematically reported how tailoring photopolymerization parameters, such as pre-polymer concentration and UVA irradiance, can influence mechanical and biological properties of final hydrogels. We thus introduced a photopolymerization protocol which could in perspective be considered a versatile tool for generating cell-laden hydrogel with easy tunable mechanical and biomimetic properties, depending on parameters setting during the photopolymerization process.

Finally, a novel protocol (PMP) to generate 3D hydrogel micropatterns with high geometrical resolution and user- defined size and shape was introduced, based on the proposed VA-086-GelMA hydrogel. The PMP approach allows uniform cell inclusion within micropatterns, creating cytocompatible and 3D geometrically controlled environments favorable for cells growth, migration and spreading. The proposed microscale strategy demonstrated highly versatility, being compatible with the *in vitro* generation of multiple shapes and heights 3D microstructures, potentially populated with different cell types and characterized by a precise spatial organization.

Further investigations are currently ongoing to exploit the PMP potentialities for the generation of 3D human adult stem cell hydrogel-based *in vitro* models, integrating the capability to provide to cultured cells different stimuli (i.e. biochemical, electrical and mechanical stimulations), aiming at favor their differentiation towards specific phenotypes.

References

1. Liu Tsang V, Bhatia SN. *Three-dimensional tissue fabrication.* Adv. Drug. Deliv. Rev. 2004;56(11):1635-1647.
2. Titmarsh DM, Chen H, Wolvetang EJ, Cooper-White JJ. *Arrayed cellular environments for stem cells and regenerative medicine.* Biotechnol. J. 2012:n/a-n/a.
3. Greiner AM, Richter B, Bastmeyer M. *Micro-Engineered 3D Scaffolds for Cell Culture Studies.* Macromol. Biosci. 2012;12(10):1301-14.
4. Griffith LG, Swartz MA. *Capturing complex 3D tissue physiology in vitro.* Nat. Rev. Mol. Cell Biol. 2006;7(3):211-224.
5. Fedorovich NE, Schuurman W, Wijnberg HM, Prins H-J, van Weeren PR, Malda J, Alblas J, Dhert WJA. *Biofabrication of Osteochondral Tissue Equivalents by Printing Topologically Defined, Cell-Laden Hydrogel Scaffolds.* Tissue Eng. C-Meth. 2012;18(1):33-44.
6. Kaji H, Camci-Unal G, Langer R, Khademhosseini A. *Engineering systems for the generation of patterned co-cultures for controlling cell–cell interactions.* BBA-Gen. Subjects 2011;1810(3):239-250.
7. Khetan S, Burdick JA. *Patterning hydrogels in three dimensions towards controlling cellular interactions.* Soft Matter 2011;7(3):830-838.
8. Gauvin R, Parenteau-Bareil R, Dokmeci MR, Merryman WD, Khademhosseini A. *Hydrogels and microtechnologies for engineering the cellular microenvironment.* Wiley Interdiscip. Rev. Nanomed. Nanobiotechnol. 2012;4(3):235-246.
9. Geckil H, Xu F, Zhang X, Moon SJ, Demirci U. *Engineering hydrogels as extracellular matrix mimics.* Nanomedicine 2010;5(3):469-484.
10. Tibbitt MW, Anseth KS. *Hydrogels as extracellular matrix mimics for 3D cell culture.* Biotechnol. Bioeng. 2009;103(4):655-663.
11. Zhu J, Marchant RE. *Design properties of hydrogel tissue-engineering scaffolds.* Expert Rev. Med. Devic. 2011;8(5):607-626.
12. Huang GY, Zhou LH, Zhang QC, Chen YM, Sun W, Xu F, Lu TJ. *Microfluidic hydrogels for tissue engineering.* Biofabrication 2011;3(1):012001.
13. Menzies DJ, Cameron A, Maisonneuve BGC, GrOndahl L, Wolvetang E, Cooper-White J. *Enzyme mediated, oxidative crosslinking of multifunctional, branched PEG: Characterization, particle formation and stem cell encapsulation.* Journal of Tissue Engineering and Regenerative Medicine 2012;6:208-208.
14. Zhang HB, Wang L, Song L, Niu GG, Cao H, Wang GJ, Yang HA, Zhu SQ. *Controllable Properties and Microstructure of Hydrogels Based on Crosslinked Poly(ethylene glycol) Diacrylates with Different Molecular Weights.* Journal of Applied Polymer Science 2011;121(1):531-540.
15. Uematsu K, Hattori K, Ishimoto Y, Yamauchi J, Habata T, Takakura Y, Ohgushi H, Fukuchi T, Sato M. *Cartilage regeneration using mesenchymal stem cells and a three-dimensional poly-lactic-glycolic acid (PLGA) scaffold.* Biomaterials 2005;26(20):4273-4279.
16. Lutolf MP, Raeber GP, Zisch AH, Tirelli N, Hubbell JA. *Cell-Responsive Synthetic Hydrogels.* Advanced Materials 2003;15(11):888-892.
17. Nichol JW, Koshy ST, Bae H, Hwang CM, Yamanlar S, Khademhosseini A. *Cell-laden microengineered gelatin methacrylate hydrogels.* Biomaterials 2010;31(21):5536-5544.
18. Mercuri J, Addington C, Pascal R, Gill S, Simionescu D. *Development and initial characterization of a chemically stabilized elastin-glycosaminoglycan-collagen composite shape-memory hydrogel for nucleus pulposus regeneration.* Journal of Biomedical Materials Research Part A 2014:n/a-n/a.

19. Burdick JA, Prestwich GD. *Hyaluronic Acid Hydrogels for Biomedical Applications.* Advanced Materials 2011;23(12):H41-H56.
20. Rao RR, Ceccarelli J, Vigen ML, Gudur M, Singh R, Deng CX, Putnam AJ, Stegemann JP. *Effects of hydroxyapatite on endothelial network formation in collagen/fibrin composite hydrogels in vitro and in vivo.* Acta Biomaterialia (0).
21. Zhang L, Yuan T, Guo L, Zhang X. *An in vitro study of collagen hydrogel to induce the chondrogenic differentiation of mesenchymal stem cells.* J. Biomed. Mater. Res. A 2012;100A(10):2717-2725.
22. Trkov S, Eng G, Di Liddo R, Parnigotto PP, Vunjak-Novakovic G. *Micropatterned three-dimensional hydrogel system to study human endothelial-mesenchymal stem cell interactions.* J. Tissue Eng. Regen. M. 2010;4(3):205-215.
23. Raghavan S, Nelson CM, Baranski JD, Lim E, Chen CS. *Geometrically Controlled Endothelial Tubulogenesis in Micropatterned Gels.* Tissue Eng. A 2010;16(7):2255-2263.
24. Ehrbar M, Sala A, Lienemann P, Ranga A, Mosiewicz K, Bittermann A, Rizzi SC, Weber FE, Lutolf MP. *Elucidating the Role of Matrix Stiffness in 3D Cell Migration and Remodeling. Biophys.* J. 2011;100(2):284-293.
25. Ifkovits JL, Burdick JA. *Review: Photopolymerizable and Degradable Biomaterials for Tissue Engineering Applications.* Tissue Eng. 2007;13(10):2369-2385.
26. Liu V, Bhatia S. *Three-Dimensional Photopatterning of Hydrogels Containing Living Cells.* Biomed. Microdevices 2002;4(4):257-266.
27. Du Y, Ghodousi M, Qi H, Haas N, Xiao W, Khademhosseini A. *Sequential Assembly of Cell-Laden Hydrogel Constructs to Engineer Vascular-Like Microchannels.* Biotechnol. Bioeng. 2011;108(7):1693-1703.
28. Aubin H, Nichol JW, Hutson CB, Bae H, Sieminski AL, Cropek DM, Akhyari P, Khademhosseini A. *Directed 3D cell alignment and elongation in microengineered hydrogels.* Biomaterials 2010;31(27):6941-6951.
29. Tsang VL, Chen AA, Cho LM, Jadin KD, Sah RL, DeLong S, West JL, Bhatia SN. *Fabrication of 3D hepatic tissues by additive photopatterning of cellular hydrogels.* FASEB J. 2007;21(3):790-801.
30. Lu T, Li Y, Chen T. *Techniques for fabrication and construction of three-dimensional scaffolds for tissue engineering.* International journal of nanomedicine 2013;8:337-50.
31. Liu A, Bhatia, S.N. *Three- Dimesional Photopatterning of Hydrogels Containing Living Cells.* Biomed. Microdevices 2002;4(4):257-266.
32. Bulcke Vd. *Structural and Rheological Properties of Methacrylamide Modified Gelatin Hydrogels.* Biomacromolecules 2000; 1(1): 31-38.
33. Eng G, Lee BW, Parsa H, Chin CD, Schneider J, Linkov G, Sia SK, Vunjak-Novakovic G. *Assembly of complex cell microenvironments using geometrically docked hydrogel shapes.* Proceedings of the National Academy of Sciences 2013;110(12):4551-4556.
34. Bryant SJ, Nuttelman CR, Anseth KS. *Cytocompatibility of UV and visible light photoinitiating systems on cultured NIH/3T3 fibroblasts in vitro.* J. Biomat. Sci.-Polym. E. 2000;11(5):439-57.
35. Fairbanks BD, Schwartz MP, Bowman CN, Anseth KS. *Photoinitiated polymerization of PEG-diacrylate with lithium phenyl-2,4,6-trimethylbenzoylphosphinate: polymerization rate and cytocompatibility*. Biomaterials 2009;30(35):6702-6707.
36. Chandler EM, Berglund CM, Lee JS, Polacheck WJ, Gleghorn JP, Kirby BJ, Fischbach C. *Stiffness of photocrosslinked RGD-alginate gels regulates adipose progenitor cell behavior.* Biotechnol. Bioeng. 2011;108(7):1683-1692.
37. Moreira HR, Munarin F, Gentilini R, Visai L, Granja PL, Tanzi MC, Petrini P. *Injectable pectin hydrogels produced by internal gelation: pH dependence of gelling and rheological properties.* Carbohydrate Polymers 2014;103(0):339-347.

38. Xia Y, Whitesides GM. *Soft Lithography.* Angewandte Chemie International Edition 1998;37(5):550-575.
39. Moeller HC, Mian MK, Shrivastava S, Chung BG, Khademhosseini A. *A microwell array system for stem cell culture.* Biomaterials 2008;29(6):752-763.
40. Selimovic S, Piraino F, Bae H, Rasponi M, Redaelli A, Khademhosseini A. *Microfabricated polyester conical microwells for cell culture applications.* Lab on a Chip 2011;11(14):2325-2332.
41. Hutson CB, Nichol JW, Aubin H, Bae H, Yamanlar S, Al-Haque S, Koshy ST, Khademhosseini A. *Synthesis and Characterization of Tunable Poly(Ethylene Glycol): Gelatin Methacrylate Composite Hydrogels.* Tissue Engineering Part A 2011;17(13-14):1713-1723.
42. Gauvin R, Khademhosseini A. *Microscale Technologies and Modular Approaches for Tissue Engineering: Moving toward the Fabrication of Complex Functional Structures.* Acs Nano 2011;5(6):4258-4264.
43. Nikkhah M, Edalat F, Manoucheri S, Khademhosseini A. *Engineering microscale topographies to control the cell–substrate interface*. Biomaterials 2012;33(21):5230-5246.
44. Jin L, Wang T, Zhu M-L, Leach MK, Naim YI, Corey JM, Feng Z-Q, Jiang Q. *Electrospun Fibers and Tissue Engineering.* J. Biomed. Nanotechnol. 2012;8(1):1-9.
45. Park SA, Lee SH, Kim W. *Fabrication of hydrogel scaffolds using rapid prototyping for soft tissue engineering.* Macromol. Res. 2011;19(7):694-698.
46. Yeh J, Ling Y, Karp JM, Gantz J, Chandawarkar A, Eng G, Blumling Iii J, Langer R, Khademhosseini A. *Micromolding of shape-controlled, harvestable cell-laden hydrogels.* Biomaterials 2006;27(31):5391-5398.
47. Rouillard AD, Berglund CM, Lee JY, Polacheck WJ, Tsui Y, Bonassar LJ, Kirby BJ. *Methods for Photocrosslinking Alginate Hydrogel Scaffolds with High Cell Viability.* Tissue Eng. C-Meth. 2011;17(2):173-179.
48. Tuchinda C, Lim HW, Strickland FM, Guzmán EA, Wong HK. *Comparison of broadband UVB, narrowband UVB, broadband UVA and UVA1 on activation of apoptotic pathways in human peripheral blood mononuclear cells.* Photodermatol. Photoimmunol. Photomed. 2007;23(1):2-9.
49. Billiet T, Gevaert E, De Schryver T, Cornelissen M, Dubruel P. *The 3D printing of gelatin methacrylamide cell-laden tissue-engineered constructs with high cell viability.* Biomaterials 2014;35(1):49-62.

4

A Microfluidic Cell Mixing Approach for the Establishment of Programmed 2D and 3D Co-Culture Models

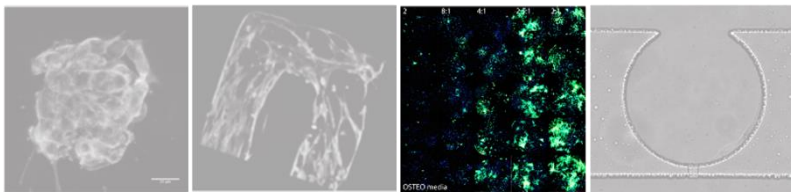

The work described in this chapter was carried out at the *Tissue Engineering and Microfluidics Laboratory (TEaM)*, University of Queensland, Brisbane, Australia.

Rationale

Native tissues are characterized by interactions among different cell types, which communicate to each other through both gradients of paracrine signals and direct cell-cell contacts. Moreover, cues from the extracellular matrix are involved in the inter-cellular communication phenomena, dynamically interacting with cell signaling throughout both soluble and solid factors. The possibility to investigate and better understand this dynamic interplay among diverse cell populations relies on the development of *in vitro* co-culture strategies able to recapitulate such native complexity.

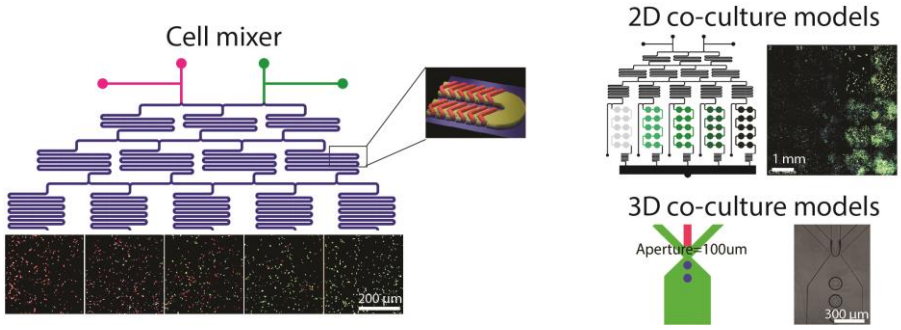

A innovative microfluidic cell mixer was introduced for the generation of 2D and 3D cell co-culture models, within a highly controlled microenvironment.

In this perspective, within a collaboration with the Tissue Engineering and Microfluidics Laboratory (TEaM, University of Queensland, Australia), we proposed an innovative microfluidic approach for easily and rapidly generating 2D and 3D co-culture models characterized by highly controlled microenvironmental conditions. More in detail, this chapter addresses the development of a microfluidic cell mixer that allowed for diluting initially concentrated cellular suspensions, in a programmed manner, generating linear concentration patterns (0% - 100%, with steps 25%). The cell mixer is then integrated as upstream functional element within two different microfluidic platforms, for the automatic establishment of 2D and 3D co-culture models within a highly controlled microenvironment.

Although potentially compatible with any cell type, the versatility of proposed microfluidic platforms as tools for stem cell biology studies have been here demonstrated throughout the establishment of 2D and 3D osteogenic models, aiming at investigating the influence of pre-osteoblastic cells on human mesenchymal stromal cell osteogenic commitment.

4.1 Introduction

In vivo, cell behavior is highly influenced by physical and chemical cues, deriving from both ECM and neighboring cells, which vary dynamically in time and space. Cells are indeed surrounded by a complex environment, in which varieties of cellular phenotypes interact to each other through both gradients of paracrine signals and direct cell-cell interactions. Together, these inter-cellular communication phenomena play a key role in defining cells commitment towards specific fates [1,2]. The possibility to study the dynamic interplay of diverse cell populations relies on the development of *in vitro* co-culture strategies able to recapitulate such native complexity. To date, most co-culture techniques are based on the use of transwell systems, which relies on the exploitation of a permeable membrane to keep cell physically separated, while allowing transmembrane communications. Although exploited in several fields of cell biology (i.e. osteoblast-stem cells [3], neurons-astrocytes [4], cardiac fibroblast-cardiomyocytes [5] co-cultures), these approaches generally lack in accurately recapitulating the complexity of multicellular environments. As already detailed in Chapter 1, they mainly consist in macroscale culture systems in which cells are manually grown under static conditions and where direct cell-cell physical interactions are inhibited [6]. In addition, these methods are time-consuming, allow for testing few conditions at a time and offer a limited control over dynamics of cell communication processes.

Recently, microfabrication technologies have been exploited to downscale co-culture environments to a level that better matches the typical scale size of cellular interaction phenomena [7,8]. A common miniaturized approach for generating highly organized co-culture models relies on the capability of spatially compartmentalizing different cell populations within defined microenvironments, relying on the use of geometrical constrains [9], semi-permeable membranes [10], micropatterning strategies (i.e. as described in Chapter 3) [11-14] or pneumatic/hydraulic valves [7,8]. Moreover, recent advances in the development of microbioreactors for cell cultures allowed the combination of abovementioned advantages of miniaturization with innovative, dynamic and high-throughput strategies for tailoring biomimetic cellular environments [15]. The continuous perfusion within microchannels has been first demonstrated to define more uniform and controlled culture conditions than traditional static approaches, providing constant dilution of catabolites and a stable supply of nutrients [6,16]. Moreover, the ability to handle cells and fluids within precise spatial

configurations allows for potentially screening several culture parameters in a high-throughput fashion [17]. Although many microfluidic strategies have been developed to generate and deliver dynamic and differently shaped patterns of soluble factors (e.g. small molecules such as growth factors, as described in Chapter 2) [18-21], the capability to dilute non-soluble particles (e.g. cells) into defined ratios is still limited due to the lack of convective mixing in standard microchannels [22]. To overcome the diffusive mixing limitations of microfluidic devices, a few technical solutions have been proposed [23]. These are based on either active approaches, relying on external energy inputs [24,25], or passive manipulation of fluid flows [26-29]. Among the latters, great popularity has been obtained by methods based on 'split and recombine' [26] and chaotic mixing [27] strategies, both consisting on the consecutive division and recombination of the streaming flow into multiple sub-portions, thus decreasing the effective diffusion length among adjacent streamlines. In particular, chaotic mixers have become widespread due to their straightforward implementation on most microfluidic layouts without specific redesign but the addition of staggered herringbones (HB) features on top of rectangular cross-sectional channels.

In this chapter, we demonstrated the capability to dilute cell suspensions into predetermined concentrations through the implementation of chaotic mixing. At this aim, we designed an innovative chaotic-based serial dilution generator (SDG), optimized for programmed dilution of cells allowing for the generation of linear concentration patterns (0% - 100%, with steps 25%). The optimized cell mixer was first integrated in a microfluidic device to generate spatially controlled 2D co-culture models within five downstream culture units. The presented platform combined the ability to establish co-culture models in a high-throughput and fully automated fashion, with the advantage of culturing cells within perfusion microbioreactors. Furthermore, the integration of fluidically connected culture chambers allowed to study the evolution of co-culture models in dependence of both different cell ratios and paracrine signaling.

Finally, a second microfluidic platform was *ad hoc* conceived, again based on the cell mixer module, for the fabrication of 3D hydrogel microspheres embedding cells diluted into programmed linear ratios. In details, thanks to well-established knowledge of hydrogel engineering and droplet microfluidic technology [30-35], we coupled the presented cell mixing approach with integrated flow-focusing elements, compatible with the fabrication and the subsequent analysis of uniform-sized aqueous emulsion particles (i.e., droplets of hydrogel

pre-polymer). Potentialities of the proposed cell mixer were thus extended to the generation of 3D multicellular microenvironments directly *on chip*. The possibility to define complex microscale models, recapitulating stimuli from both adjacent cells and microenvironment, was thus envisioned with the final aim to investigate either i) interactions among different cell types within 3D biomimetic microstructures or ii) the role of cell concentration on different tissues morphogenesis.

Upon a complete functional validation, the potentiality and versatility of both proposed microfluidic platforms as tools for stem cell biology studies have been finally demonstrated, throughout the establishment of 2D and 3D osteogenic models, aiming at investigating the influence of pre-osteoblastic cells on human mesenchymal stromal cell osteogenic commitment.

4.2 Design and validation of an innovative microfluidic cell mixer

In the following paragraphs, the CFD design (4.2.1) and fabrication (4.2.2) of an innovative microfluidic cell mixer is be described. The cell mixer is then functionally validated, by assessing its efficiency in mixing soluble factors (4.2.3), non-diffusive particles (4.2.4) and finally cells (4.2.5).

4.2.1 Cell mixer design and CFD optimization

A cell mixer, based on a chaotic SDG element, was implemented to mix cells with a split-and-recombine scheme, achieving programmed concentration ratios. It comprises a symmetric microfluidic network (channel size of 240x100µm in width and length, respectively) [18], integrated with HB grooves to increase the mixing through vortex formation [27]. The HB features, having the same width of underneath channels, were designed 60µm long and 36µm high. The elementary mixing building block (HB unit) consisted of a 1.72mm long channel, embedding a dozen of HB features, changing their orientation every half cycle.

The minimum number of repeating HB units required to ensure mixing of both soluble factors (i.e. growth factors, D=8,4 x 10^{-11} m^2/sec) and non-diffusive species (e.g. cells) was identified through finite element analysis by means of Computational Fluid Dynamic models (CFD, Comsol Multiphysics). Analyses were performed on 3D geometrical models of HB grooved channels consisting of ten HB units, using rectangular channels with the same length as controls. Geometries were discretized through a tethraedrical mesh, consisting of about 1061 x 10^3 and 110 x 10^3 elements, in the case of presence and absence of HBs, respectively (Fig.4.1a). The flow field was computed by solving stationary Navier–Stokes equations for incompressible flow, setting density and viscosity equal to those of water at 37°C (1000 kg/m^3 and 0.890 cP, respectively). Uniform velocity profiles were applied to inlets, corresponding to Reynolds numbers (Re) ranging from 0.01 and 1 (Qin=0.25-25µl/min), while a zero pressure condition was set to the outlet. A no-slip condition was applied to boundary walls. Convergence criterion was satisfied when the normalized residuals for the velocities were below 1×10^{-6}. Mixing efficacy was evaluated along cross sections of channels by means of the Transport of Diluted Species application model. Fig.4.1a and b show the trend of concentrations along both HB and control channels corresponding to Re 0.01 and 1. A range of Re between 0.01 and 1 was investigated, as considered compatible to cell viability in terms of shear stress affecting cells during seeding

procedures. Starting from concentration values obtained along channels, an index of mixing efficacy (ME) was computed as a function of the number of repeated units (*n*) (Fig.4.1c and d). Imposing $\bar{c} = 0.5$, ME was calculated at the end of each repeated unit as it follows:

$$ME_n = 1 - \frac{c_n - \bar{c}}{\bar{c}}$$

The mixing was considered complete for ME_n higher than 0.95, thus being *n* the minimum number of repeated units required for achieving an efficient mixing.

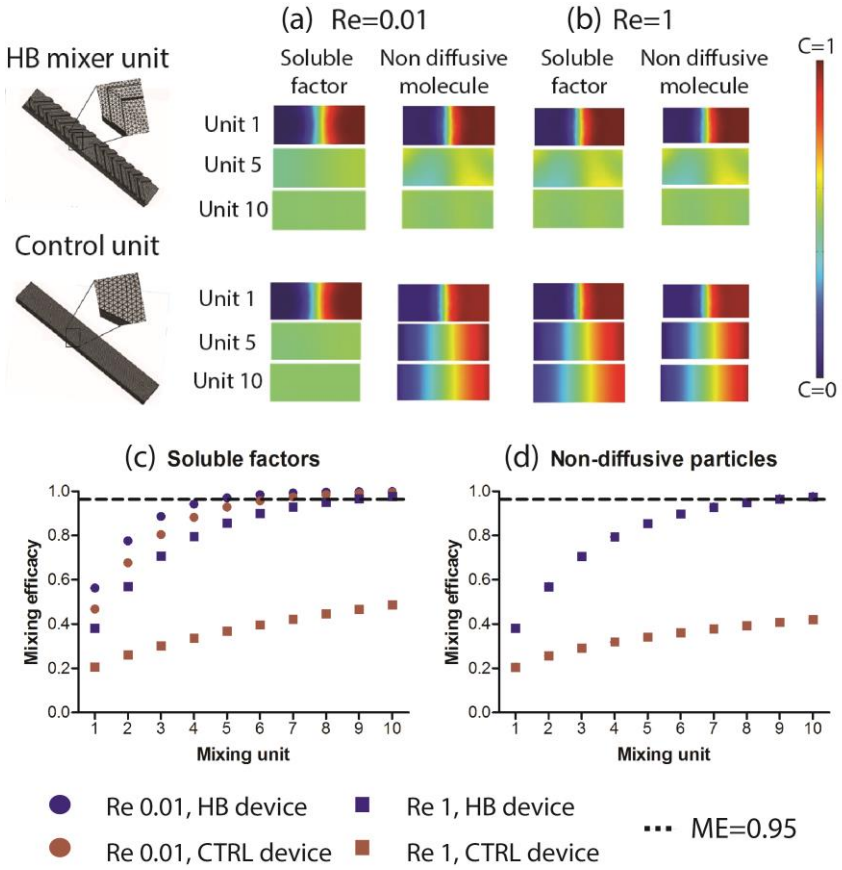

***Figure 4.1**. Mixing efficiency of both HB mixer and control units were evaluated through CFD simulations for both soluble and non-diffusive species. Re=0.01 (a) and 1 (b). An index of mixing efficacy was calculated (ME) as function of repeated units (c, d). The mixing was considered complete for ME_n higher than 0.95, thus being n the minimum number of repeated units required for achieving an efficient mixing.*

Considering soluble factors, the presence of HB structures significantly enhanced the mixing at both Re numbers (Fig.4.1c). In details, for low Re (0.01) the mixing is achieved in both HB and control channels, after five and six repeated units, respectively. Conversely, at Re 1 no mixing occurs in the purely diffusive control channel, while the addition of HBs allowed for obtaining a complete mixing after eight units. Regarding non-diffusive particles (Fig.4.1d), a uniform mixing is achievable through a repetition of at least eight HBs units,

while no significant mixing was detectable in corresponding rectangular control channels at neither Re numbers.

4.2.2 Cell mixer fabrication

A first chip layout (Fig.4.2) was designed *ad hoc* for the preliminary experimental validation of the cell mixer. Each level of the mixer was dimensioned to ensure an efficient cell mixing from the two main inlets (A1, A2). Estimated eight as the minimum number of repeated units theoretically required for reaching the mixing (Fig.4.1d), a margin of safety was defined and the number of HB unit was further increased at each SDG level, according with the decrease of flow rate along the symmetric network [18]. In detail, 17, 21 and 27 HB units were integrated in the three levels of the SDG, respectively. Five downstream independent collecting units were finally implemented, each consisting in a rectangular culture chamber (w3000 x l6000 x h100 µm).

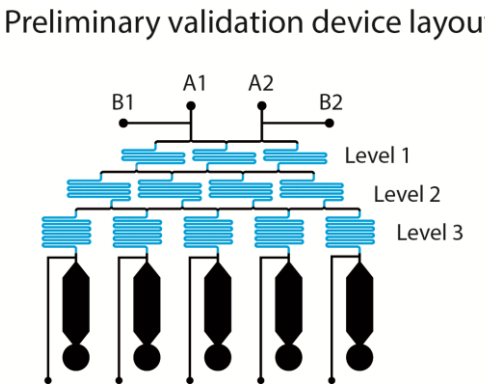

Figure 4.2. *Based on computational results, an* ad hoc *device layout was conceived for preliminary mixing validations, consisting of (i) a three level serial dilution generator integrated with herringbone units for chaotic mixing (blue features) and (ii) a collecting area comprising five parallel units. Each unit consisted of a rectangular culture chamber (w3000 x l6000 x h100 µm).*

The device layout (Fig.4.2) was drawn in CAD software (AutoCAD, Autodesk Inc.) and consisted in two layers: (i) a 100µm thick layer for fluidic channels and chambers (Fig.4.2, black features) and (ii) a 36µm thick layer for the HB structures, positioned on the top of the previous one (Fig.4.2, blue features). Each layer was printed at high resolution on a chrome mask, subsequently used to prepare silicon wafer masters through photolithography. SU8-2050 and SU8-2025 negative tone photoresists were used for first and second layers, respectively. Feature height was confirmed by optical surface profilometry (Veeco NT1100). Master molds consisting exclusively in the 100µm thick layer were also developed to produce control devices.

Microfluidic devices were obtained via soft lithography [36] by replica molding of PDMS (Sylgard® Dow Corning Midland, MI) on the master mold. Briefly, PDMS was cast on the mold in ratio 10:1 w/w (pre-polymer to curing agent), degassed and cured at 80°C for 3hr. After baking, devices were cut out and peeled off the SU-8 device master. Input and output ports were obtained through a 0.75mm biopsy puncher (Harris Uni-Core™). The PDMS layer was finally plasma treated (Plasma Cleaner, Harrick Plasma, 20s, 10W, 380mTorr O_2) and bonded to a cleaned (acetone, isopropanol, nitrogen) 50x75x1mm microscope slide (Proscitech, Thuringowa, Australia).

4.2.3 Cell mixer experimental validation: mixing of soluble factors

The mixing efficiency of soluble species within the cell mixing element (qualitatively visualized by perfusing colored dyes; Fig.4.3a and b) was experimentally validated for Re 1 and compared to that obtained through the equivalent purely diffusive SDG (featuring non-grooved channels). In details, a solution of 20 mg/ml bovine serum albumin (BSA, Sigma) in dH_2O was pumped from the A2 inlet at a flow rate of 25 µl/min, whereas dH_2O was pumped through A1 at the same flow rate. After the establishment of steady state conditions, samples of protein dilutions were collected from the outlets (n=3) and the BSA concentration was measured by means of a BCA Protein Assay kit (Pierce, Thermo Fisher Scientific), following the manufacturer's indications. The concentration of BSA contained in the five dilutions collected from output ports matched the expected linear distribution for the HB device with an accuracy R^2=0.9923 (Fig.4.3c). In contrast, BSA concentration measurements obtained for the purely diffusive SDG demonstrated an inefficient mixing.

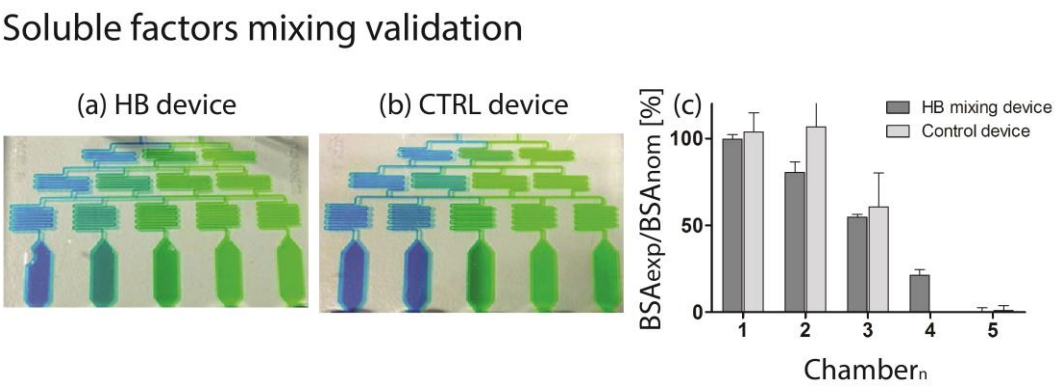

Figure 4.3. *Characterization of HB (a) and CTRL (b) cell mixer devices. For assessing the mixing of soluble factors, devices were perfused either with different colored dyes (a, b) or with 20 mg/ml BSA solution and dH2O (c) at Re=1. Quantitative measurement of BSA concentration in the 5-outlet chamber solutions resulted in a linear trend only for the HB device, demonstrating how the presence of the HB structures significantly enhanced the mixing for high Re numbers (n=3) (c).*

4.2.4 Cell mixer experimental validation: mixing of non-diffusive particles

The partition of non-diffusive particles within the cell mixer was evaluated by means of microparticles image velocimetry (μPIV) analysis, assessing fluid flow profiles at each bifurcation (Re=1). Results were then compared with the equivalent purely diffusive SDG. For these measurements, a suspension of red fluorescent particles of mean diameter 2μm was seeded from inlet A1, while dH_2O was pumped in A2. A TSI PIVCAM 13 – 8 CCD (1280 x 1024 pixel resolution) camera synchronized with a dual-head Nd:YAG pulse laser was used to obtain sequential images. For each intersection of the SDG networks, 50 images were captured at 25fps. As a measurement of the particle concentration, the fluorescence intensity of the area occupied by particle trajectories was quantified in the regions corresponding to the five SDG outlets. Values were finally normalized for the 100% inlet intensity (A1).

Figure 4.4 shows the reconstructed profiles of particle trajectories in the three levels of SDGs. In the HB device (Fig.4.4a), particles injected into inlet A1 were equally splitted after each level of the gradient, giving rise to a final linear concentration gradient at the SDG outlets. Conversely, in the control device (Fig.4.4b), particles resulted confined to the injection side of the device, thus following their original fluidic paths in the absence of chaotic mixing. These results were confirmed by the fluorescence quantification (Fig.4.4c). It is worth noting that comparable net concentration values were obtained at the central outlet (outlet 3) of both devices. However this result is a consequence of the integral nature of the measure. Indeed, as depicted in μPIV images, in the HB device particles are effectively spread throughout the channel width, having a homogeneous concentration corresponding to half of the upstream one, whereas in the control device the channel is divided in two separated lanes (having a width of about half channel each), containing roughly 100% and 0% of the upstream concentration, respectively.

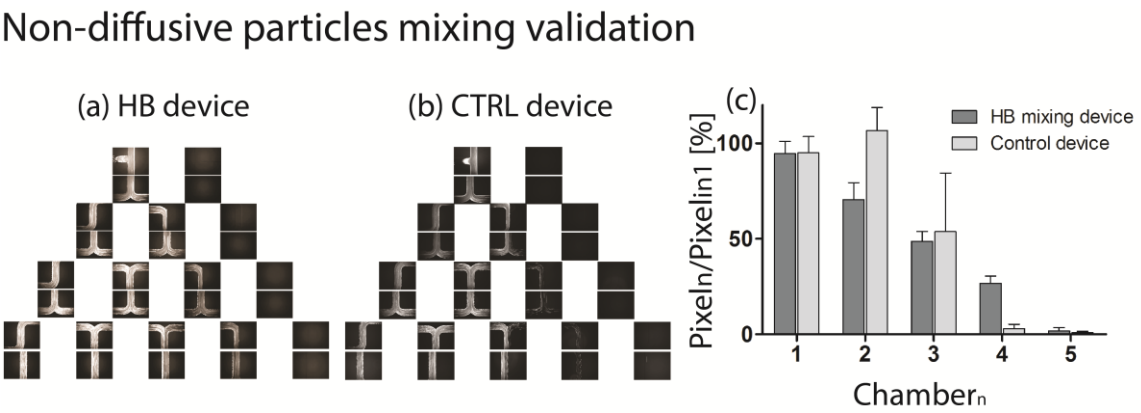

Figure 4.4. *Characterization of HB (a) and CTRL (b) devices in diluting non diffusive particles. The partition of non-diffusive particles were visualized (a,b) and quantified (c) through microparticles image velocimetry (μPIV) analysis, again confirming the requirement of HB features for achieving efficient mixing of non-diffusive particles.*

4.2.5 Cell mixer experimental validation: mixing of cells

Cell mixing was assessed by seeding fluorescently labeled NIH-3T3 cells within both HB and control devices. Before cell seeding, autoclaved devices were submerged in sterile PBS enriched with 25 μg/mL of amphotericin B (Gibco, Australia) and degassed [37]. Subsequently, bioreactors were surface-coated with extracted human fibronectin (BD Biosciences, North Ryde, Australia) at a solution concentration of 25 μg/ml for 30mins at 37°C. After expansions, NIH-3T3 were fluorescently labeled through a 10 minutes incubation in culture medium enriched with 5μl/ml of either DiO or DiL Vibrant solution (DiD, DiL and DiO multicolor kit, Invitrogen Corporation, USA), harvested from tissue culture flasks with TrypLE Express (Gibco, Grand Island, NY) and resuspended in FBS at a final concentration of 1 x 10^6 cells/ml. A reverse color gradient was generated by seeding DiO- and DiL-labeled NIH-3T3 from A1 and A2, respectively, at a flow rate of 25μl/min (Re=1) from each inlet. After 1 min, the flow was stopped and cells were allowed to adhere for 4 hours in an incubator (37°C, 5% CO_2). Subsequently cells were fixed in 4% paraformaldehyde (PFA) and their nuclei were counterstained with Hoechst. 16-bit, multi-color montage images of entire microfluidic platform were acquired using a Zeiss LSM 710 laser scanning confocal microscope and the number of red and green cells for each chamber was quantified by means of CellProfiler software [38].

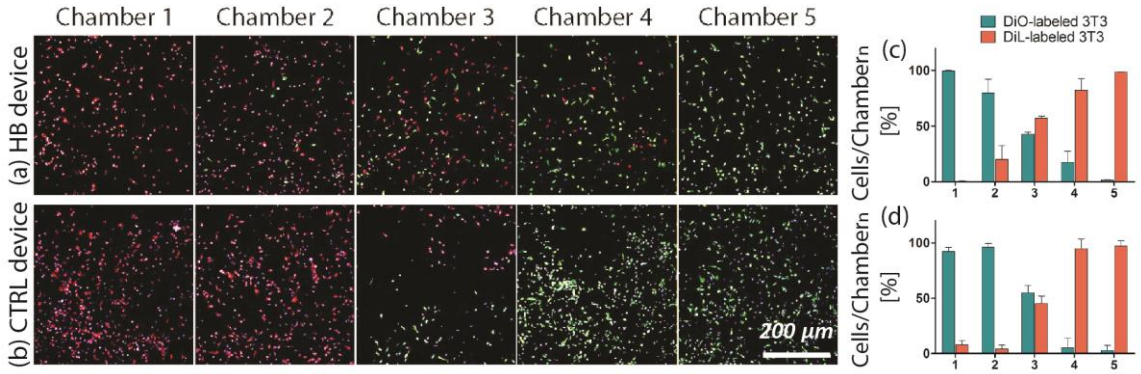

Figure 4.5. *NIH-3T3 cells mixing validation. DiO- and DiL-labeled 3T3 were perfused from opposite inlets of devices (Re=1) and mixing was evaluated at the five outlet chambers. While linear reverse gradients were obtained for the HB device (a), as also confirmed by the quantification (c), no mixing occurred in the control device, characterized by a segregation of differently labeled cells on opposite device sides (b, d). (n=3).*

As evidenced by fluorescence images (Fig.4.5a), linear reverse gradients of red and green cells were achieved through the HB device. Conversely, no mixing occurred within the control device, remaining the two differently labelled cell populations segregated on opposite sides of the chambers (Fig.4.5b). These results were supported by cell quantification within the microbioreactor chambers (Fig.4.5c and d), underlining in the HB device the generation of cell mixing ratios matching the expected values.

4.3 Microfluidic platform for the establishment of 2D co-culture models

With the aim to combine the ability to establish co-culture models in a high-throughput and fully automated fashion, with the advantage of culturing cells under dynamic perfusion, the cell mixer was integrated into a microbioreactor consisting in five independent culture area downstream the mixer outlets (Fig.4.6). Each culture units consisted in ten fluidically connected circular culture chambers (Φ=1.63mm, h=100µm) [21] and was integrated with a lateral seeding channel. Two secondary inlets (Fig.3.6 B1, B2) were finally included in the layout to facilitate the medium change operations. The final microbioreactor layout was drawn in CAD software (AutoCAD, Autodesk Inc.) and fabricated via soft lithography [36] as previously described.

As a proof of principle, osteogenic 2D co-culture models were established within the proposed platform, to assess the role of pre osteoblastic cells (SAOS2) on hBM-MSCs osteogenic differentiation.

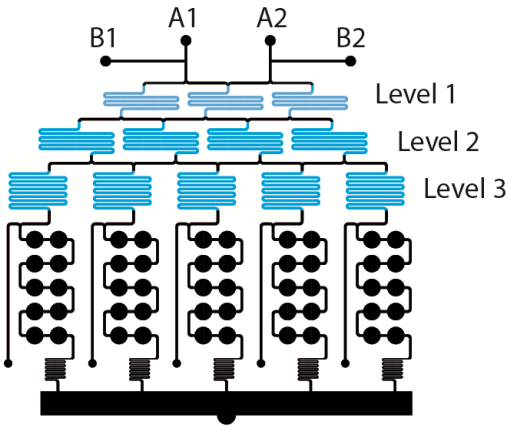

Figure 4.6. *A microbioreactor for culturing 2D co-culture models was designed consisting of (i) the previously validated cell mixer (blue features) and (ii) a culture area comprising five parallel units. Dilutions of cells were generated from two main inlets (A1-A2) and delivered to downstream culture units (b). Each culture unit consisted of 10 fluidically connected culture chambers and was combined with a lateral seeding channel. Two additional inlets (B1-B2) facilitated the medium change operations, defining a by-pass for the device.*

4.3.1 Cell expansion

Primary osteogenic sarcoma human cell line (SAOS2) were cultured until 80% confluent, according to the recommendation of the supplier, in Dulbecco's modified Eagle's medium, high glucose (Gibco, Australia) supplemented with 10% Fetal Bovine Serum (FBS), penicillin (100 units/mL) and streptomycin (100 µg/mL) (Gibco, Australia).

Human bone-marrow mesenchymal stem cell (hBM-MSCs, donor 8006, Lonza) were seeded at 4000 cells/cm^2 and cultured until 80% confluent in maintaining medium (MM), consisting in Dulbecco's modified Eagle's medium, low glucose supplemented with 10% FBS, penicillin (100 units/mL) and streptomycin (100 µg/mL) (Gibco, Australia). Medium was changed twice a week and hBM-MSCs were used between P5 and P6 for experiments.

4.3.2 Establishment of hBM-MSCs and SAOS2 osteogenic 2D co-culture models

Two different co-culture models were generated: (i) a reverse gradient of hBM-MSC/SAOS2 and (ii) a low concentration gradient of SAOS2 seeded on equally dense monolayers of hBM-MSCs (see Table 4.1).

Table 4.1. *hBM-MSCs/SAOS2 co-culture models*

Co-culture model	Microbioreactor unit	hBM-MSCs/SAOS2
hBM-MSCs/SAOS2 reverse gradient	1	1:0
	2	3:1
	3	1:1
	4	1:3
	5	0:1
SAOS2 low concentration gradient	1	8:0
	2	8:1
	3	8:2
	4	8:3
	5	8:4

For the first model, hBM-MSCs (0.5 x 10^6 cells/ml in maintaining medium) and SAOS2 (0.25 x 10^6 cells/ml in maintaining medium) were contemporary seeded from inlets A1 and A2, respectively, at a flow rate of 25µl/min (Re=1) from each inlet. For the second

model, hBM-MSCs were first seeded at a constant concentration (0.5 x 10^6 cells/ml in MM) through both inlets and allowed to adhere for 4 hours in an incubator (37°C, 5% CO_2). SAOS2 were then seeded on top of adherent hBM-MSCs, by perfusing SAOS2-laden medium (0.25 x 10^6 cells/ml) from A2 and maintaining medium from A1 (flow rates of 25µl/min). For both models, cells were allowed to adhere for 4 hours in an incubator (37°C, 5% CO_2). Devices were then either stopped right after seeding for assessing generation of cell gradients or placed in culture under mild continuous perfusion (2µl/hr to each culture unit [39]) of either maintaining medium (control devices) or osteogenic medium (osteo devices) for 7 days. Osteogenic medium (OM) consisted of MM supplemented with 2 mM L-glutamine, 0.1 µM dexamethasone, 50 µM ascorbic acid, and 10 mM β-glycerophosphate. Static controls were also established, consisting of co-cultures of hBM-MSCs and SAOS2 seeded in 96 wells plates with proportions matching those achieved within microbioreactors (see Table 4.1). Medium was changed every two days in static control plates.

The effective establishment of predicted mixing conditions (see Table 4.1) was assessed at day0 within all five culture units. To quantify the final cell mixing ratios, $CD73^+$ stained cells were identified as hBM-MSCs [40]. In the hBM-MSCs/SAOS2 reverse gradient model, immunofluorescence images of cells seeded within chambers demonstrated the formation of two linear patterns moving towards the microbioreactor in opposite directions (Fig.4.7a). Further quantifications showed a correspondence between experimental and expected mixing ratios in each condition (Fig.4.7b). Similarly, within the second model, a linear increase of SAOS2 cells was generated (Fig.4.7f), being 2:1 the highest hMSCs/SAOS2 obtained ratio (Fig.4.7g). The achievement of a uniform hBM-MSCs/SAOS2 ratio within the 10 chambers of each culture unit was also assessed for both models (Fig.4.7c, d, h, i).

The ability to deliver an initial constant number of cells in each bioreactor chamber was finally assessed. In the reverse gradient model, cells were uniformly distributed throughout the entire device (Fig.4.7e) with an average seeding density of (59±20) cells/chamber. Regarding the second model, a uniform cell distribution was achieved in the whole microbioreactor after the establishment of the hBM-MSCs monolayers, featuring each culture chamber an average of (65±17) cells. These cell densities (2830±860cells/cm^2 and 3145±818cells/cm^2, respectively) match the static controls (set to 3000cells/cm^2), being compatible with preceding osteogenic differentiation studies [41,42].

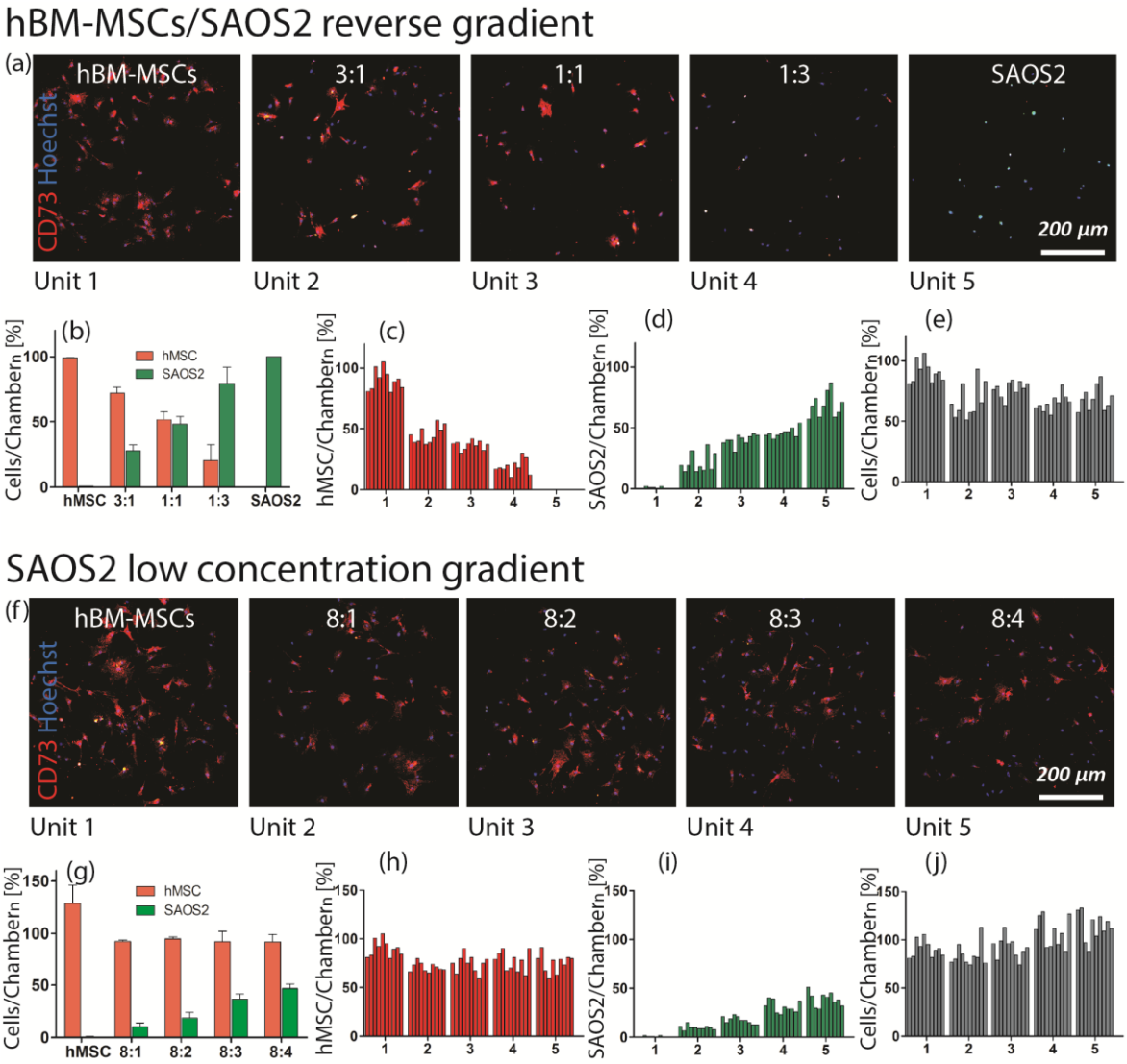

Figure. 4.7. *Establishment of programmed hBM-MSCs/SAOS2 osteogenic co-culture models within the microfluidic platform. Two different models were generated: (i) a reverse gradient of hBM-MSCs/SAOS2 (a-e) and (ii) a low concentration gradient of SAOS2 on a constant monolayer of hBM-MSCs (f-j). Immunofluorescence images of resulting mixing ratios were acquired (a, f), in which hBM-MSC were identified as CD73^{+} cells. Cell partitioning quantification for each culture unit confirmed the achievement of predicted mixing ratios (b, g), matching the first model a reverse linear gradient (from 100% hBM-MSC to 100% SAOS2, with steps of 25%) and the second one a low concentration decrement of SAOS2 (from 0% to 50% than constant hBM-MSC). In both models, cells were uniformly distributed throughout the entire bioreactor (e, j). (n=2)*

4.3.3 hBM-MSCs/SAOS2 perfusion co-culture models: impact of SAOS2 concentration on alkaline phosphatase expression and cell proliferation

The SAOS2 low concentration gradient model was further exploited for investigating the effect of pre-osteoblastic cells on hBM-MSCs differentiation towards the osteogenic lineage. Microbioreactors were maintained in culture for 7 days, under continuous slow perfusion of either maintaining or osteogenic medium (2µl/hr to each culture unit). They were then were fixed and analyzed *in situ* both for immunofluorescence of alkaline phosphatase activity (using an ELF97 endogenous phosphatase detection kit) as a marker for early osteogenic differentiation, and Ki67 as a proliferation marker. Moreover, nuclear DNA staining (propidium iodide) was used as a measure of cell number. Representative fluorescence images acquired from one entire bioreactor are showed in Figure 4.8, where ELF97 and Ki67 expressions are reported for both MM and OM tested conditions. Corresponding fluorescence levels of ELF97 (normalized for culture area) and Ki67 (normalized for the total cell number) are showed for each considered hBM-MSCs/SAOS2 co-culture ratio (Fig.4.8b, d, f, and h). Both images and quantifications demonstrated the translation of the SAOS2 concentration gradient in a corresponding gradient of alkaline phosphatase expression (column groups of the bioreactor). Indeed the increase of pre-osteoblastic cells in the co-culture resulted in a significant higher expression of ELF97 when osteogenic medium was perfused. It is worth noting that a similar trend was observed even under maintaining medium conditions (Fig.4.8a). Moreover, a slight increase in ELF97 expression along downstream chambers of the same bioreactor column may indicate a paracrine effect from upstream chambers, due to mild perfusion. For each conditions, three technical repetition were analyzed, showing the same trend described previously for ELF97 expression (Fig.4.9).

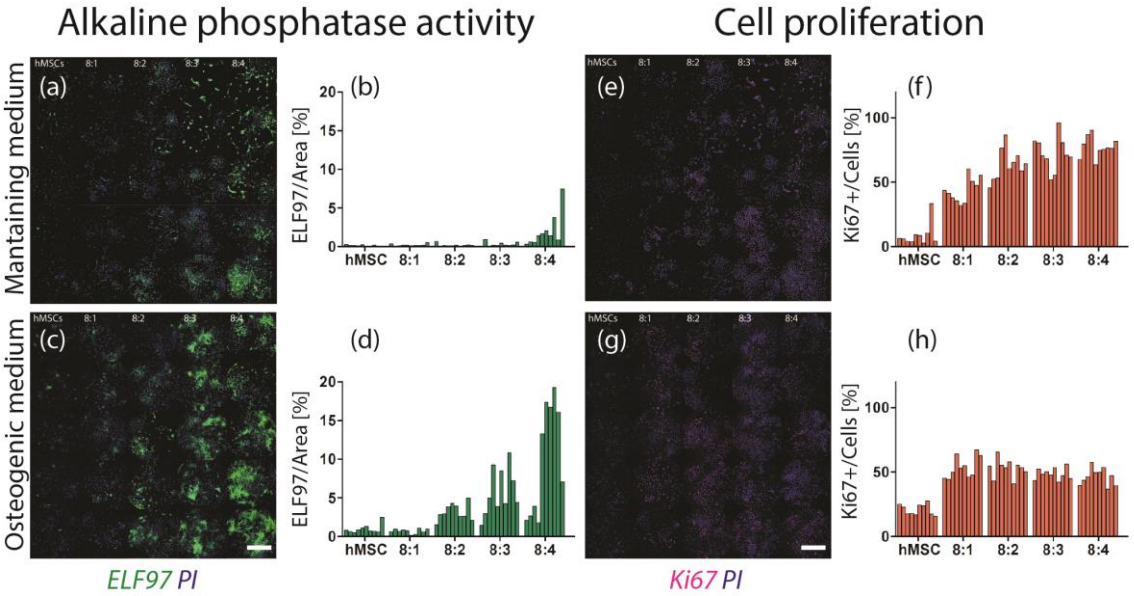

Figure. 4.8. *hBM-MSCs-SAOS2 perfusion co-culture model: impact of SAOS2 concentration on alkaline phosphatase expression and cell proliferation. Fluorescence images showing ELF97 (a, c) and Ki67 (e, g) expressions for each considered hBM-MSCs/SAOS2 co-culture ratios (8:0, 8:1, 8:2, 8:3 and 8:4), after 7 days under either maintaining (a, e) or osteogenic (c, g) medium slow perfusion (2µl/hr each column). Showed results correspond to one bioreactor repetition and five representative chambers are showed for each bioreactor unit (scale bars=1mm). Corresponding fluorescence levels of ELF97 normalized for culture area (b, d) and Ki67 normalized for the total cell number (f, h) are showed for each chamber in the bioreactor.*

Regarding cell proliferation (Fig.4.8e-h), the number of $Ki67^+$ cells increased with the increase of hBM-MSCs/SAOS2 ratio in maintaining medium, in accordance with a higher proliferation rate of the SAOS2 cell line compared to hBM-MSCs. Conversely, the presence of osteogenic medium led to a plateau in the cell proliferation in culture conditions characterized by the presence of SAOS2 cells (Fig.4.8g-h).

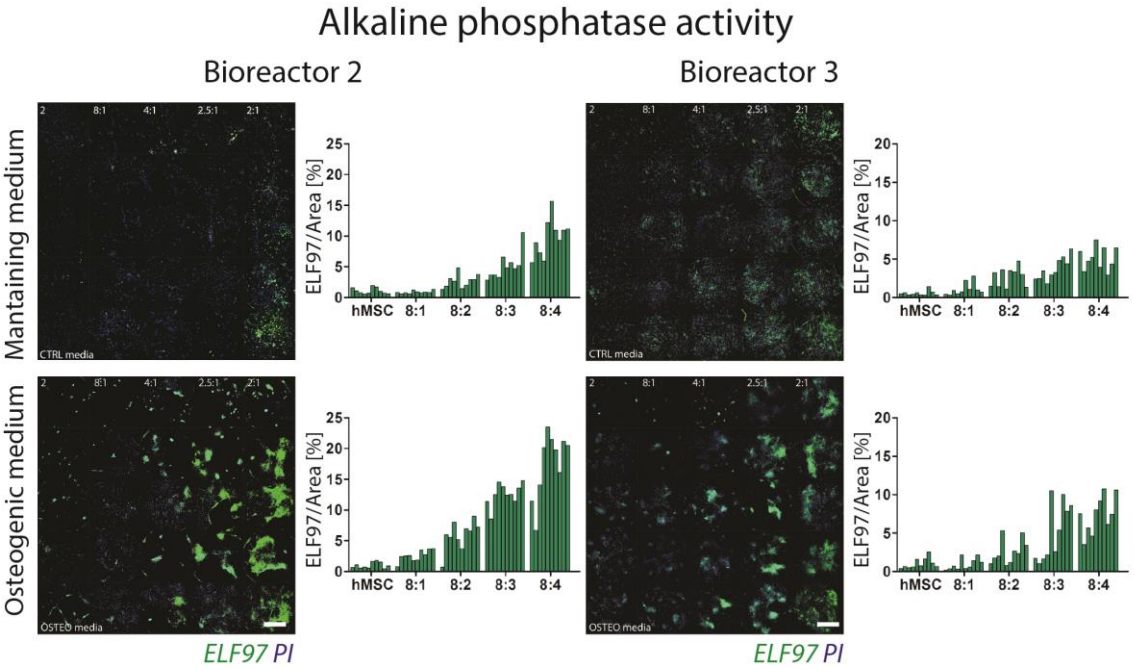

Figure 4.9. *hBM-MSCs/SAOS2 perfusion co-culture model: impact of SAOS2 concentration on alkaline phosphatase expression. Showed results correspond to two technical repetition of the experiments and five representative chambers are showed for each bioreactor unit (scale bar=1mm).*

4.4 3D co-culture models: *on chip* fabrication of hydrogel microspheres embedding cells mixed at controlled ratios

Aiming at recreating complex biomimetic architectures, the cell mixer was exploited as tool for the generation of 3D multicellular microenvironments directly *on chip*. For this purpose, a microfluidic platform was conceived for the fabrication of 3D hydrogel microspheres embedding cells diluted into programmed linear ratios. Whit this platform we envisioned the possibility either i) to model 3D interactions among different cell types or ii) to study the role of cell concentration on different tissues morphogenesis (Fig.4.10).

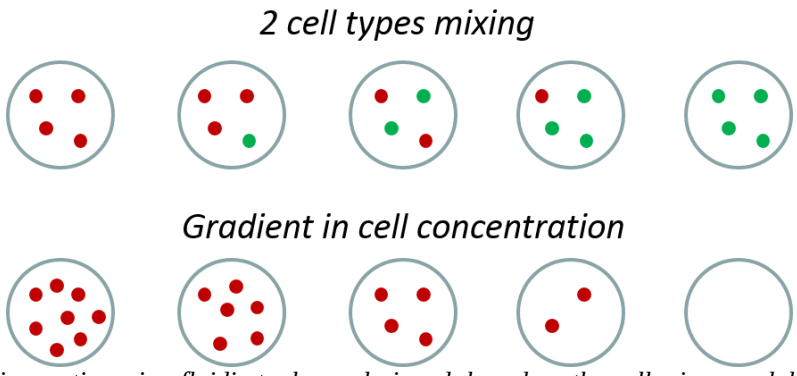

Figure 4.10. *An innovative microfluidic tool was designed, based on the cell mixer module, envisioning the possibility either i) to model 3D interactions among different cell types or ii) to study the role of cell concentration on different tissues morphogenesis.*

At these aims, a flow-focusing element has been developed and functionally validated for the generation of controlled-sized hydrogel microspheres, as described in the next paragraphs (4.4.1, 4.4.2, 4.4.3). Its integration downstream the cell mixer is then showed, demonstrating to be a promising tool for generating 3D co-culture models (4.4.4, 4.4.5).

4.4.1 Microfluidic platform for the generation of 3D microspheres

Several techniques have been proposed in the last few years to generate microspheres within microfluidic devices [23,34,43,44]. Among others, approaches based on the so-called flow focusing techniques have gained popularity due to their robustness [30,31,45,46,47]. Indeed, by designing a 4-channel intersection (3 inlet and 1 outlet, Fig.4.11b), uniform-sized aqueous emulsion particles (i.e. droplets) can be generated by tuning the concurrent flow rates of a continuous phase (i.e. oil) and a disperse phase (i.e. pre-polymer solution) [48]. Based on this principle, a microfluidic platform (Fig.4.11a) was designed, consisting in two functional

units: 1) the previously optimized cell mixer, delivering its outputs (i.e. pre-polymer solutions) to 2) five downstream flow-focusing elements (detailed in Fig.4.11b). Each flow focusing element consisted in the intersection between i) a disperse phase channel (DP, Fig.4.11b pink features), defined as a prolongation of the corresponding cell mixer outlet, and ii) two continuous phase channels (CP, Fig.4.11b green features) for perfusing solutions immiscible with the DP. In particular, aiming at obtaining droplets with diameters ranging around 100µm, an aperture of 100µm was set at the intersection of DP and CP flowing channels, whose heights were set equal to 100µm and 140µm, respectively. To guide the neo-formed droplets at a reduced speed, 600µm wide channels were integrated downstream, connecting each flow-focusing element with a corresponding collection area, conceived for hosting microspheres during polymerization and imaging processes. The complete platform layout (Fig.4.11a) was drawn in CAD software (AutoCAD, Autodesk Inc.) and fabricated via soft lithography [36] as previously described.

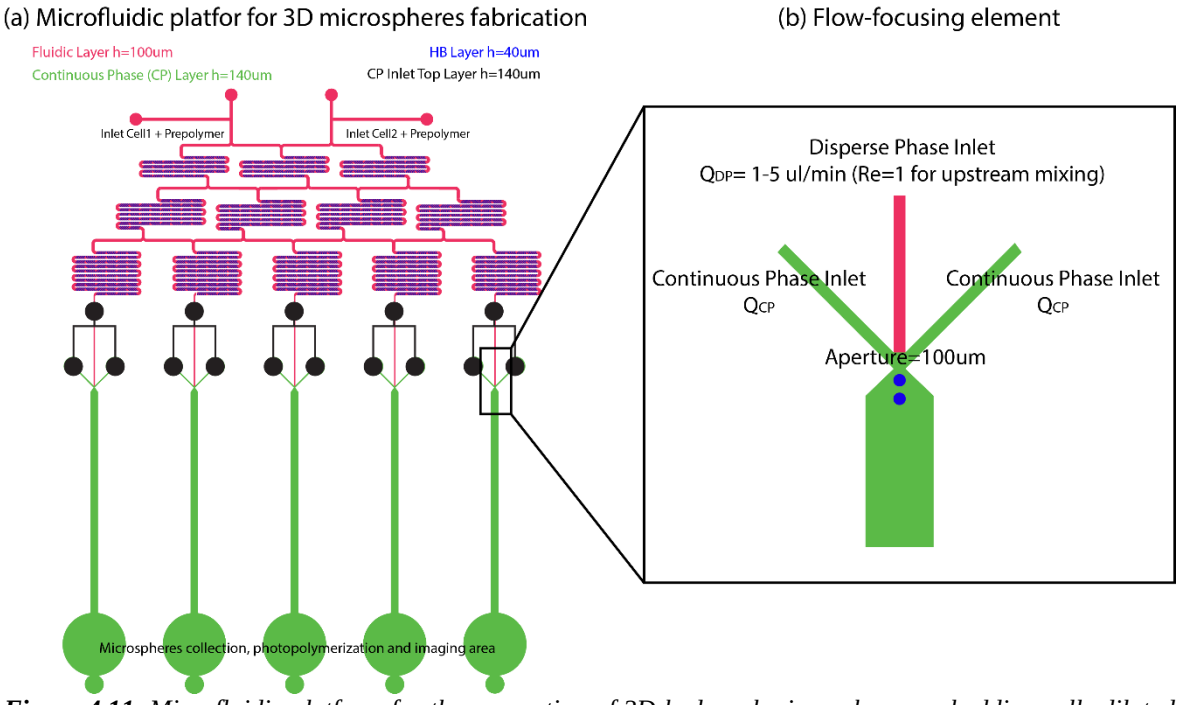

Figure 4.11. *Microfluidic platform for the generation of 3D hydrogel microspheres embedding cells diluted into programmed linear ratios. The final layout (a) consists in two functional units: i) the previously optimized cell mixer (pink and blue features), each outlets integrated with 2) a flow-focusing element (b). The interaction between a continuous phase (CP, black features) and a disperse phase (DP), flowing through outlets of the cell mixer (pink features)(i.e. pre-polymer solution), leads to the generation of uniform-sized droplets (depicted in b as blue spheres). An aperture of 100µm was set at the intersection of DP and CP flowing channels (featuring thickness of 100 and 140µm, respectively). 600µm wide channels were integrated downstream each flow-focusing element for guiding the generated droplets towards a final collection area, also conceived for hosting microspheres during polymerization and imaging processes.*

Fig.4.12 shows the sequence of steps leading to the formation of 3D microspheres embedding cells at programmed linear ratios. Upon perfusion of two different pre-polymer solutions, five homogeneous solutions are provided at the outlets of the cell mixer (Fig.4.12a), obtained as sequential dilutions of the inlet pre-polymer ones. According to the desired application (Fig.4.10), either a reverse gradient of two cell types (inlet solutions containing cells of different phenotypes) or a linear dilution in cell concentration (inlet solutions containing cells at different concentrations) can be achieved. Each mixed pre-polymer solution serves as disperse phase input for the corresponding flow-focusing element (Fig.4.12b). Generated droplets, embedding different combinations/concentration of cells, flow to the collection areas, where the polymerization may occur. Different polymerization techniques can be exploited depending on the pre-polymer chemical nature and application requirements (Fig.4.12c).

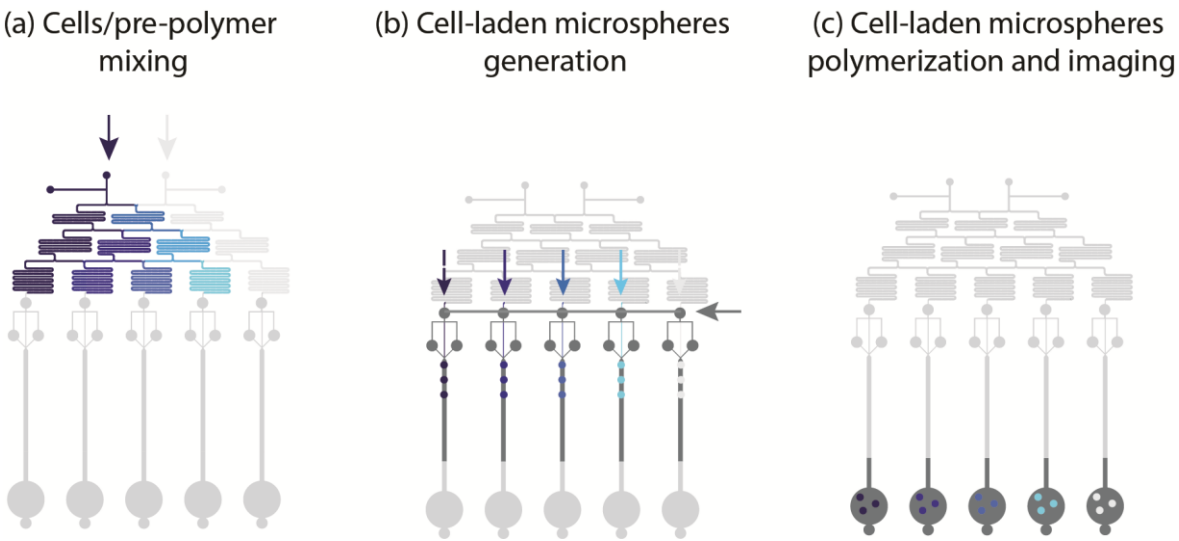

Figure 4.12. *Sequence of steps leading to the generation of 3D hydrogel microspheres embedding cells diluted into programmed linear ratios. By flowing through the cell mixer, five pre-polymer solutions are obtained, each loaded with different combinations/concentration of cells (a). Each solution flows as DP within the corresponding flow-focusing element, where the interaction with the CP leads to the generation of pre-polymer droplets (b). Generated droplets, embedding different combinations/concentration of cells, finally reach a collecting area, where the polymerization occurs (c).*

4.4.2 Validation of non-diffusive particles mixing in viscous fluid

At first, the capability of the previously optimized cell mixer to split non-diffusive particles suspended in viscous fluids (i.e. pre-polymer solutions) was assessed. In details, a solution featuring a dynamic viscosity of 10mPa·sec was obtained by adding glycerol (60% w/w) to water. An aliquot of the solution was further labeled by adding a suspension of fluorescent microparticles (diameter of 2μm). Both solutions were pumped into the inlets of the cell mixer at a flow rate of 2.5μl/min (Re=0.1). The splitting of microparticles into five linear dilutions was evaluated through fluorescence microscopy from the outlets of the cell mixer (Fig.4.13a), and results were compared to ones obtained with a purely diffusive SDG (Fig.4.13b) used as negative control.

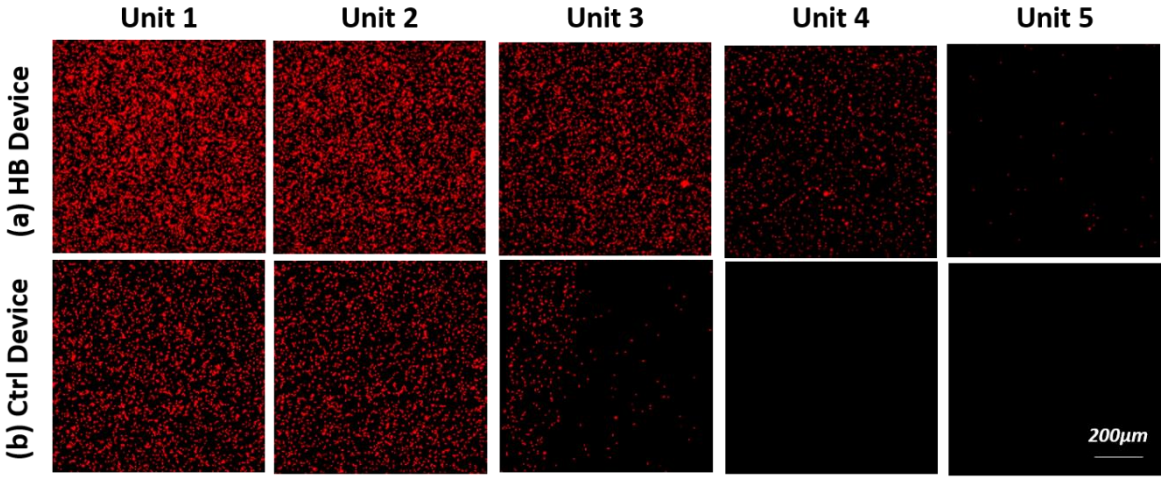

Figure 4.13. *Mixing of microparticles suspended in 60% glycerol. While a linear dilution of microparticles was achieved by means of the cell mixer (a), no mixing occurred within the control device, based on a purely diffusive SDG (b).*

Obtained results qualitatively showed the achievement of a linear dilution of microparticles with the cell mixer (Fig.4.13a), while no mixing occurs within the control device (Fig.4.13b). Thus, one fold increase of the viscosity of the working solution with respect to water did not affect the mixing efficacy of the cell mixer. These findings demonstrated the possibility of expanding the range of applicability of the cell mixer to the mixing of viscous fluid (i.e. pre-polymer solutions) containing cells.

4.4.3 Calibration of the flow focusing element

The capability of tuning the diameter of fabricated microspheres by changing the ratio between flow rates of continuous and disperse phases was then investigated.

A solution of glycerol 60% w/w in water was pumped into both cell mixer inlets at a constant flow rate (each equal to $Q_{in}/2$), thus yielding a flow rate of the disperse phase (Q_{DP}) of $Q_{in}/5$ at the input of the flow-focusing elements. In details, two different Q_{DP} were considered, 1 and 5µl/min, both corresponding to Re numbers showed to promote an efficient mixing in the upstream cell mixer. Mineral oil enriched with 2% v/v of a non-ionic surfactant (Span80, Sigma Aldrich) was exploited as continuous phase and pumped through CP inlets. Several flow rates of the continuous phase (Q_{CP}) were investigated, spanning a Q_{CP}/Q_{DP} ratio between 1 and 20. For each considered Q_{CP}/Q_{DP} ratio, after reaching steady-state conditions, images of neo-formed droplets were acquired by means of an high speed camera (Phantom V9.1 high speed color camera), and their diameter was estimated as the average of ten different particle diameters, measured through ImageJ software. Finally, the center-center distance between consecutive droplets was measured and results were normalized for average diameters. The obtained distance/diameter index gave a quantification of the spatial distribution of generated droplets.

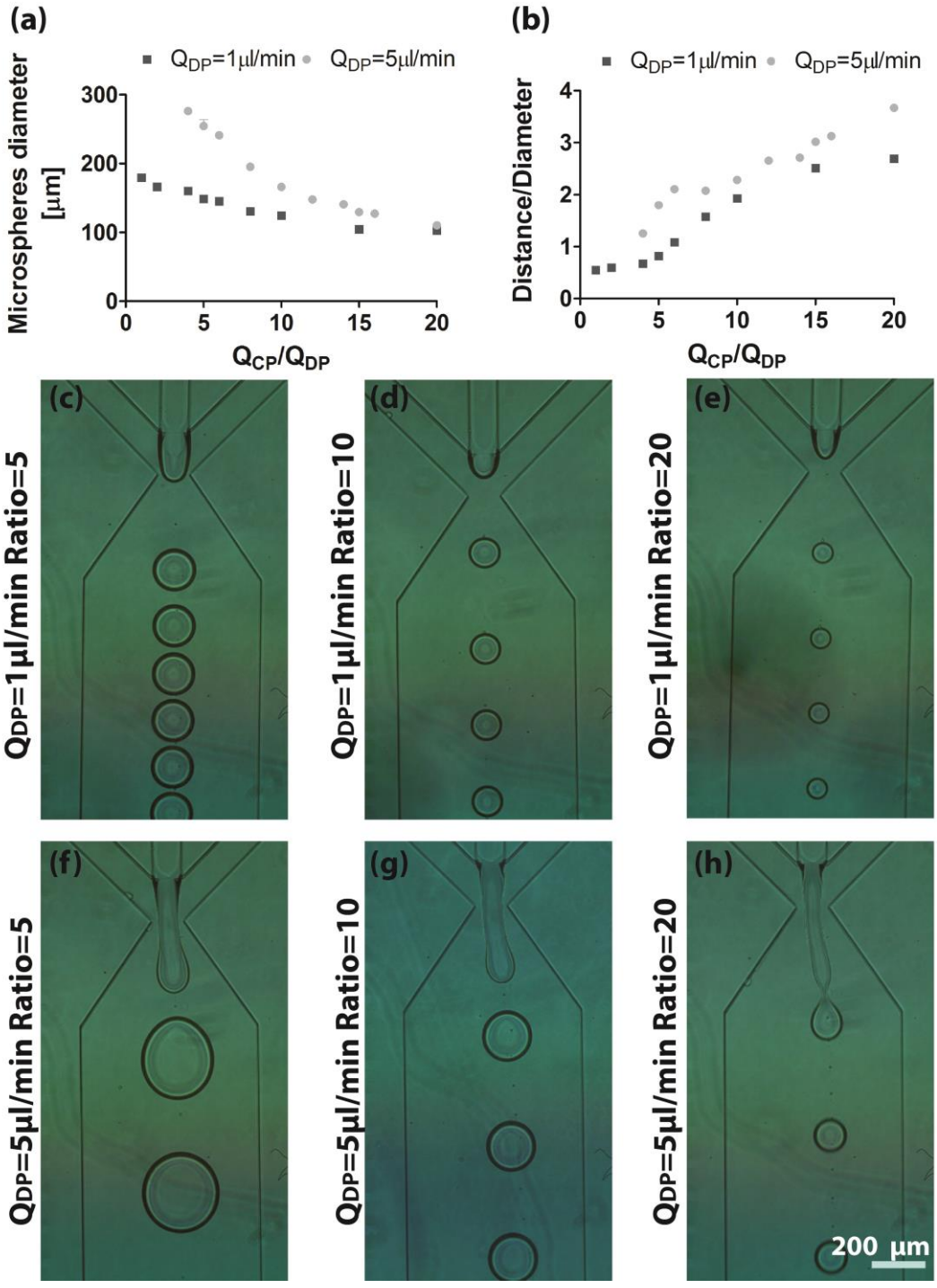

Figure 4.14. *Generation of glycerol 60% droplets by means of the flow-focusing element. The influence of both disperse phase flow rate (Q_{DP}) and Q_{CP}/Q_{DP} ratio on resulting droplet diameters (a) and spatial distributions (b) was assessed and representative results were depicted (c-h). Diameters quantification (a) showed that increasing the Q_{DP} resulted in bigger microspheres, while increasing the Q_{CP}/Q_{DP} ratio led to lower diameter values. Quantification of the distance/diameter ratio (b) showed how decreasing Q_{CP}/Q_{DP} ratios resulted in shorter distances between generated droplets.*

Fig.4.14a shows the influence of both disperse phase flow rate (Q_{DP}) and Q_{CP}/Q_{DP} ratio on the size of generated droplets. In particular, an increase in the Q_{DP} resulted in the generation of bigger microspheres. Considering, for example, a constant Q_{CP}/Q_{DP} ratio of 10 (Fig.4.14d and g, respectively), the droplet diameter increased from 124.58±1.73μm for a Q_{DP} of 1μl/min to 166.02±2.31c for a Q_{DP} of 5μl/min. Conversely, the increase of the Q_{CP}/Q_{DP} ratio led to microspheres featuring smaller diameters. Fixing the Q_{DP} at 1μl/min, the diameter of obtained droplets ranged from 148.79±0.88μm to 68.83±2.28μm, when the Q_{CP}/Q_{DP} ratio was increased from 5 to 20 (Fig.4.14c and e, respectively). Similarly, for Q_{DP} of 5μl/min, the diameter of obtained droplets changed from 254.71±9.43μm to 110.27±2.56μm, increasing the Q_{CP}/Q_{DP} ratio from 5 to 20 (Fig.4.14f and h, respectively). Moreover, a correlation between flow rates and spatial distribution of generated droplets was demonstrated (Fig.4.14b). In details, decreasing Q_{CP}/Q_{DP} ratios resulted in shorter distances between generated droplets. For both considered Q_{DP} values, the distance between consecutive droplets (normalized for respective diameter values) doubled when the Q_{CP}/Q_{DP} ratio was increased from 5 (Fig.4.14c and f) to 20 (Fig.4.14e and h). Moreover, regarding the Q_{DP} of 1μl/min, Q_{CP}/Q_{DP} ratios lower than 5 resulted in overlapped droplets characterized by a distance/diameter index lower than 1. This phenomenon led to the generation of droplets flowing in contact to each other and organized into two adjacent lines (Fig.4.15), which enhanced the possibility of collapsing. For the Q_{DP} of 5μl/min, the same event was not registered, being Q_{CP}/Q_{DP} ratios lower than 5 ineffective to the droplets generation.

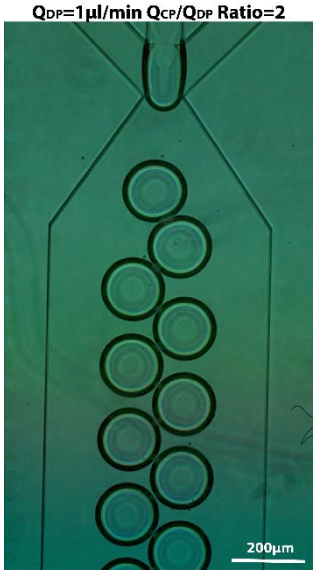

Figure 4.15. *For Q_{DP} of 1μl/min, Q_{CP}/Q_{DP} ratios lower than 5 resulted in overlapped droplets, flowing in contact to each other and organized into adjacent lines.*

Finally, the ability of generating uniformly shaped droplets at the same time throughout all the five flow-focusing elements was assessed. Fig.4.16 shows microspheres obtained at the five outlets of the microfluidic platform, for Q_{CP}/Q_{DP} ratio of 5 and Q_{DP} of 1μl/min.

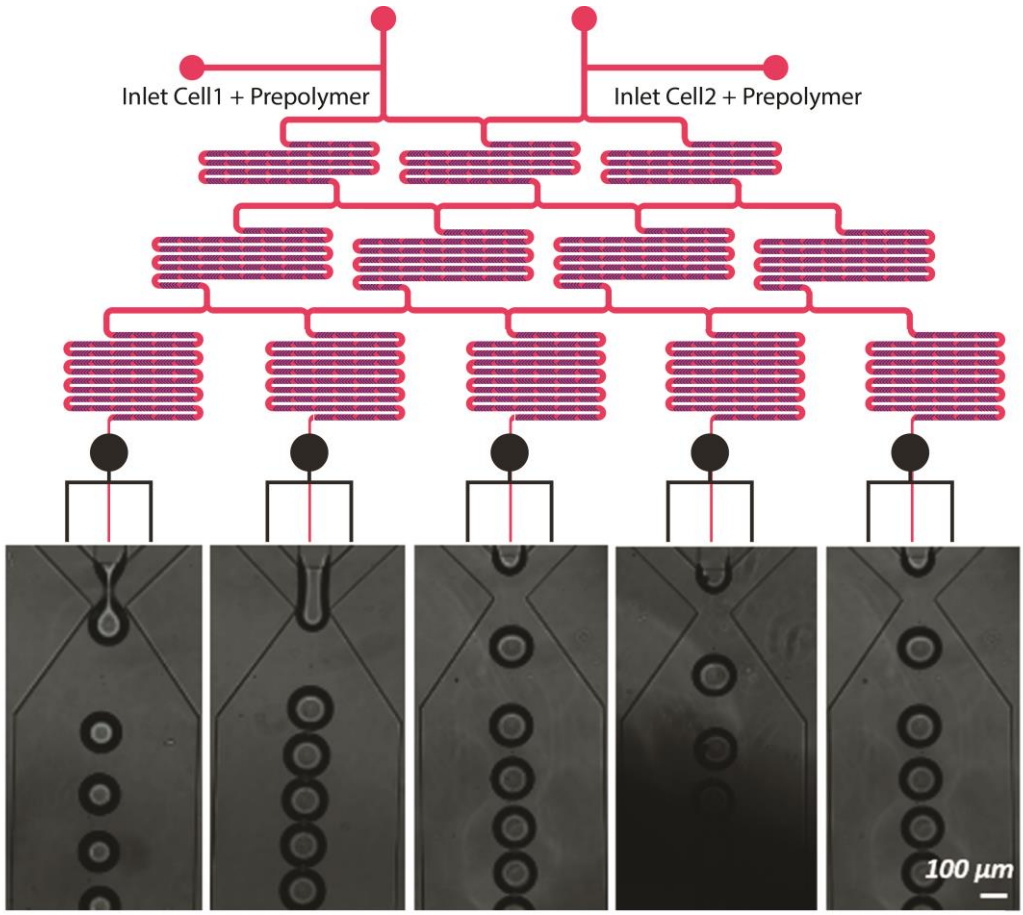

Figure 4.16. *Microspheres simultaneously obtained at the five outlets of the microfluidic platform, for Q_{CP}/Q_{DP} ratio of 5 and Q_{DP} of 1μl/min.*

4.4.4 Generation of microspheres embedding linear dilutions of microparticles

The ability of generating 3D hydrogel microspheres embedding linear dilutions of non-diffusive particles was evaluated by using PEG-based photopolymerizable hydrogels as inlet pre-polymer. Fluorescent microparticles (diameter of 2μm) were suspended in the pre-polymer solution and pumped through one inlet of the cell mixer at a flow rate of 2.5μl/min (Re=0.1), while unloaded pre-polymer was injected throughout the other inlet at the same flow rate. Mineral oil enriched with 2% Span80 was pumped simultaneously through the continuous phase inlets, imposing a Q_{CP}/Q_{DP} ratio of 10. Microparticles generated at each flow-focusing intersection were collected in the five collection areas and polymerized upon exposure to UV light (filtered at λ=365nm, $irradiance_{365nm}$=200mW/cm^2 at 7cm from the source, EXFO Acticure 4000). Phase contrast and fluorescence images of resulting hydrogel microspheres were acquired directly within the device (Fig.4.17). Microspheres were obtained from the five units of the platform, qualitatively exhibiting a linear gradient in the concentration of embedded microparticles (Fig.4.17b). The diameter of microspheres was approximately equal to 130μm (Fig.4.17a), in line with the flow-focusing calibration study. However, several irregularities were observed in particles generation, as clearly depicted in the unit 3. Such irregularity could be due either to perturbations generated upstream the flow-focusing and thus locally affecting the Q_{CP}/Q_{DP} ratio, or to droplets collapsing before the achievement of complete photopolymerization. It is though worth noting that presented data were the results of a preliminary experiment, shown for mere illustrative purposes. Indeed, further validations are currently ongoing for optimizing both microspheres generation and crosslinking steps.

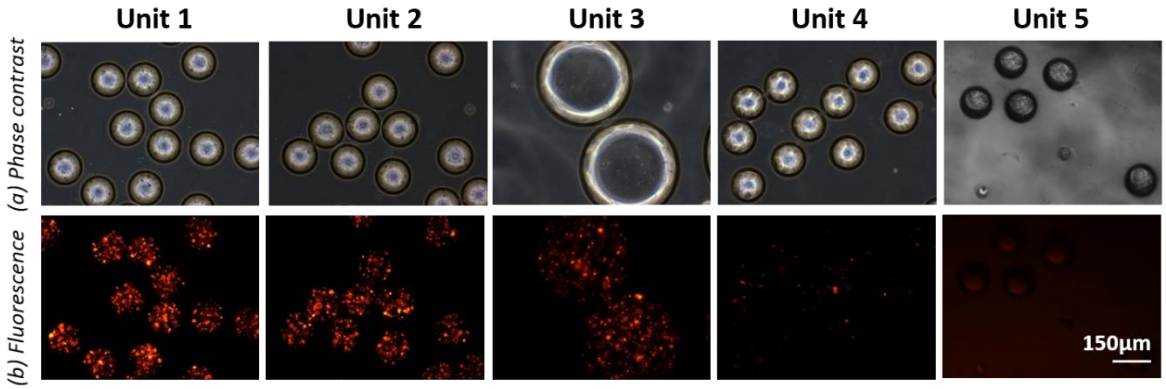

Figure 4.17. *Generation of 3D hydrogel microspheres embedding linear dilutions of non-diffusive particles, for Q_{CP}/Q_{DP} ratio of 10 and Q_{DP} of 1μl/min. Microspheres were obtained from all the five units of the platform, qualitatively exhibiting a linear gradient in the concentration of embedded microparticles (b). Apart from local irregularities, their dimension resulted rather uniform, with diameters ranging around 130μm.*

4.4.5 3D hBM-MSCs/SAOS2 co-culture models: preliminary results

Finally, the possibility to exploit the proposed platform as a tool for generating automatic 3D co-culture models in a high-throughput fashion was preliminary investigated. As a proof of principle, 3D microspheres embedding hBM-MSCs and SAOS2 mixed at programmed ratios were generated, again by means of a PEG-based photopolymerizable hydrogel. hBM-MSCs and SAOS2 were labeled in red and green, respectively, upon incubation with Vybrant staining as previously described. Each cell type was then suspended in a pre-polymer solution at a concentration of 2 x 10^6 cells/ml and obtained cell-laden solutions were simultaneously pumped through the cell mixer inlets at a flow rate of 2.5µl/min (Re=0.1) each. Mineral oil enriched with 2% Span80 was pumped through the continuous phase inlets at a flow rate of 10µl/min, thus imposing a Q_{CP}/Q_{DP} ratio of 10. Microparticles generated at each flow-focusing intersection were collected in the five collection areas and polymerized upon exposure to UV light as previously described. Phase contrast and fluorescence images of resulting hydrogel microspheres were acquired directly within the device, and results are depicted in Fig.4.18. Microspheres were obtained from all the five units of the platform, qualitatively exhibiting a linear reverse gradient of hBM-MSCs/SAOS2 (Fig.4.18b). However, the presence of cells affected the microspheres generation, resulting in low uniformity in droplets dimension and in perturbations of the flow rate balance. These phenomena could be related to changes in the DP viscosity, due either to interactions between cell and pre-polymer or to the generation of cell clusters[49]. Further validations are currently ongoing for optimizing the generation of 3D microspheres embedding programmed ratios of cells.

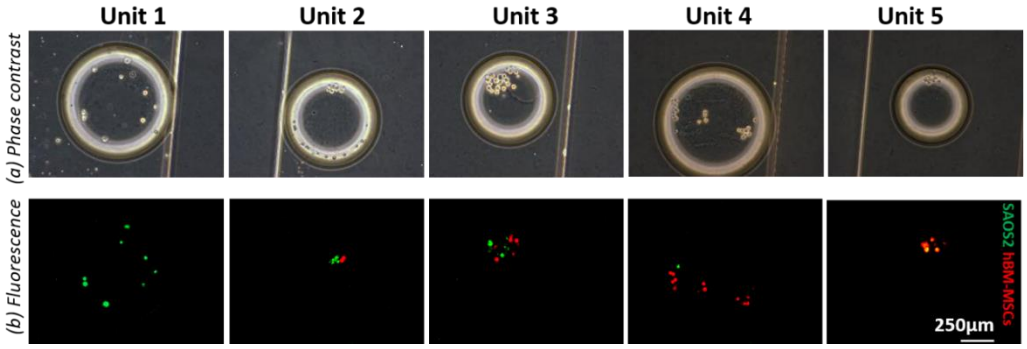

Figure 4.18. *Generation of 3D hydrogel microspheres embedding hBM-MSCs and SAOS2 mixed at defined ratios, for Q_{CP}/Q_{DP} ratio of 10 and Q_{DP} of 1µl/min. Microspheres were obtained from all the five units of the platform, qualitatively exhibiting a reverse linear gradient of hBM-MSCs and SAOS2 (b).*

4.5 Discussion

In the last decade, microfluidic technologies have been increasingly implied to design *in vitro* models able to integrate several stimuli from the cellular microenvironment, with the aim of investigating cell behavior in a controlled and reproducible way [17,50]. Indeed, through the reduction of dimensions down to typical cellular size-scales, fluid and mass transport phenomena become easy to control within microfluidic channels. Moreover, the length scale typical of microfluidics leads to highly predictable fluid dynamics, governed by a laminar flow regime [51]. That characteristics have been successfully exploited in the design of microfluidic networks able to modulate the chemical environment around cells, generating spatially defined chemical patterns by mixing soluble factors (as described in Chapter 1) [18,21]. In this study, we offered a strategy to extend the potentiality of this technology to the control of mixing of different cell types, aiming at providing a versatile and robust tool for the establishment of programmed multicellular patterns. At this aim, we integrated chaotic mixing features on top of a microfluidic network [27] to overcome the diffusion limitation correlated to the absence of convective flow at the microscale. Such grooved structures – named herringbone (HB) – have been demonstrated to induce chaotic stirring at low Re ($0<Re<100$) [27] by division and recombination of the streaming flow, thus decreasing the effective diffusion length among adjacent streamlines. Although computationally and experimentally demonstrated to provide an efficient mixing solution at the microscale [52-54], the exploitation of HB-based microchannels was never considered for mixing cells into defined ratios for downstream co-culture experiments. An HB mixing unit was thus designed and optimized to achieve cell mixing. By means of CFD analyses, the mixing efficacy was correlated to the length of HB-grooved channels. CFD results demonstrated that the inclusion of HBs effectively enhanced the mixing of soluble factors within microchannels, in a wide range of Reynolds numbers. The presence of HB grooves was then demonstrated to be a strict requirement for the achievement of mixing of non-diffusive species. Computational fluid dynamics analyses were used to estimate the minimum number of HBs units required to achieve a uniform mixing.

Considering these requirements, a cell mixer was implemented as a stand-alone tool for generating linear patterns of non-diffusive particles in a highly controlled and automatic fashion. μPIV investigations allowed for visualizing the partition of microspheres (2μm in diameter) within the entire element, showing an effective equipartition of particles at each

intersection. As further demonstrated by the quantification of particles trajectories flowing through the five outlets, the proposed technical solution permitted to achieve linear dilutions of non-diffusive species in a fast and repeatable way. As a first proof of principle, linear cell patterns were generated diluting differently labeled NIH-3T3 cells, underling the ability to obtain programmed mixing ratios with a precision hardly achievable through manual operations.

The cell mixer was then integrated within a 2D microbioreactor system. The ability of establishing co-culture models in a high-throughput and fully automated fashion was thus combined with the advantage of culturing cells under continuous perfusion. Ten fluidically connected chambers were connected to the outputs of the cell mixer to generate controlled cell-mixing ratios. Results obtained seeding different combinations/concentrations of hBM-MSCs and SAOS2 demonstrated the capability of the proposed chaotic mixing element to provide programmed and reliable linear patterns of cells. In particular, the establishment of two different models allowed underlining the versatility of the approach. The generation of a reverse gradient of hBM-MSCs/SAOS2 demonstrated the possibility of combining two different cell types, spatially tailoring their mixing ratios to match the specific application requirements. Furthermore, the ability to timely guide the evolution of co-culture models was also showed by delivering a linear pattern of SAOS2 on previously seeded monolayers of hBM-MSCs.

In both 2D models (the reverse hBM-MSCs/SAOS2 gradient and the SAOS2' low concentration one), a homogeneous cell distribution throughout microbioreactor chambers after the seeding ensured consistent initial culture conditions for further investigating the evolution of co-culture models. Proliferation and osteogenic differentiation studies were thus conducted to assess the possibility of pre-conditioning hBM-MSCs with pre-osteoblastic cells to enhance their osteogenic regenerative potential. An increase on expression of alkaline phosphatase marker (ELF97), consistent with the initial linear distribution of SAOS2, was detected throughout the microbioreactor, independently on the presence of osteogenic factors. Interestingly, the maximum concentration of SAOS2 tested in this model (hBM-MSCs/SAOS2 ratio of 2:1) was enough for inducing alkaline phosphatase activation after only seven days in culture. These results suggested how the presence of few pre-osteoblastic cells could be sufficient for moving hMSCs towards an osteogenic induction. Moreover, a slight increase in ELF97 expression was observed along downstream chambers

of each microbioreactor column. Although further investigations are needed, this result may be correlated to the paracrine effect induced by the continuous mild perfusion from upstream chambers. In addition, it is worth noting that the use of a low concentration gradient of SAOS2, justified by the interest in investigating the role of even few pre-osteoblastic cells on hBM-MSCs osteogenic differentiation [55-57], highlighted the suitability of the system in handling low numbers of living cells in a precise way, far beyond macroscale limiting dilutions.

Finally, the exploitation of the cell mixer as a tool for the automatic generation of 3D multicellular microenvironments directly *on chip* was envisioned, extending its applicability to the mixing of particles suspended in highly viscous fluids (i.e. hydrogel pre-polymers). With this aim, the demonstrated ability to mix cells into programmed ratio was combined with the capability of tailoring the 3D microenvironment around them. In details, the integration of flow-focusing elements downstream the cell mixer allowed the high-throughput generation of pre-polymer microspheres, ideally featuring a wide range of tunable properties. First, the dimension of generated droplets was correlated to flow rate parameters, underlining the possibility to span over a wide range of diameters (~50-300μm) still maintaining the flow rate within the limit required for the upstream cell mixing. Notably, uniform sized microspheres were simultaneously generated throughout the five units of the platform, being this condition strictly dependent on the fluidic coupling between flow-focusing elements and cell mixer, which provides a symmetric partition of the fluid flow.

The presented approach can potentially be applied to the fabrication of hydrogel microspheres starting from different pre-polymer solutions, being the generation of droplets obtained through the flow-focusing approach independent from the subsequent polymerization method of choice. However, the exploitation of photopolymerizable hydrogels represents among others a promising alternative due to the i) fast crosslinking reactions – minimizing the risk of droplet collapses –, and ii) taking advantage on the optical transparency of the PDMS – favoring polymerizations directly *on chip* [33]. The generation of photopolymerized microspheres embedding either a concentration gradient of microparticles or a reverse gradient of hBM-MSCs/SAOS2 was here preliminary demonstrated, showing the technical feasibility of the proposed approach. However, further investigations are currently ongoing to overcome limitations regarding the uniformity of the microspheres production and their subsequent photopolymerization.

Conclusive remarks

In this chapter, an innovative microfluidic strategy was introduced for diluting and mixing different cell populations in an automatic and programmed way. The potentiality of this microfluidic cell mixer was here underlined through the establishment of osteogenic co-culture models. Results obtained from the generated hMSCs/SAOS2 2D co-culture models served as an example for pointing out the potentialities of the proposed microbioreactor as a promising tool for investigating cell-cell interaction dynamics. It is however worth noting how the presented platform would be suitable for generating controlled co-culture models potentially starting from any mammalian cell combination.

Moreover, the presented cell mixing approach was integrated in a platform designed for hydrogel droplets generation, defining an innovative and promising tool for high throughput fabrication of 3D multicellular microenvironments. To this aim, we are envisioning the possibility to integrate the advantages of biomimetic hydrogels with the versatility of the proposed cell mixer, for the fabrication of 3D cell-laden hydrogel microspheres tunable in terms of both concentrations and combinations of cells.

References

1. Greenwald I, Rubin GM. *Making a difference: The role of cell-cell interactions in establishing separate identities for equivalent cells.* Cell 1992;68(2):271-281.
2. Rouault H, Hakim V. *Different Cell Fates from Cell-Cell Interactions: Core Architectures of Two-Cell Bistable Networks.* Biophysical Journal 2012;102(3):417-426.
3. Wang Y, Volloch V, Pindrus MA, Blasioli DJ, Chen J, Kaplan DL. *Murine osteoblasts regulate mesenchymal stem cells via WNT and cadherin pathways: mechanism depends on cell–cell contact mode.* Journal of Tissue Engineering and Regenerative Medicine 2007;1(1):39-50.
4. Walsh E, Ueda Y, Nakanishi H, Yoshida K. *Neuronal survival and neurite extension supported by astrocytes co-cultured in transwells.* Neuroscience Letters 1992;138(1):103-106.
5. Bang C, Batkai S, Dangwal S, Gupta SK, Foinquinos A, Holzmann A, Just A, Remke J, Zimmer K, Zeug A and others. *Cardiac fibroblast-derived microRNA passenger strand-enriched exosomes mediate cardiomyocyte hypertrophy.* Journal of Clinical Investigation 2014;124(5):2136-2146.
6. El-Ali J, Sorger PK, Jensen KF. *Cells on chips.* Nature 2006;442(7101):403-411.
7. Gao Y, Majumdar D, Jovanovic B, Shaifer C, Lin PC, Zijlstra A, Webb D, Li D. *A versatile valve-enabled microfluidic cell co-culture platform and demonstration of its applications to neurobiology and cancer biology.* Biomedical Microdevices 2011;13(3):539-548.
8. Liu W, Li L, Wang X, Ren L, Wang X, Wang J, Tu Q, Huang X, Wang J. *An integrated microfluidic system for studying cell-microenvironmental interactions versatilely and dynamically.* Lab on a Chip 2010;10(13):1717-1724.
9. Taylor AM, Dieterich DC, Ito HT, Kim SA, Schuman EM. *Microfluidic Local Perfusion Chambers for the Visualization and Manipulation of Synapses.* Neuron 2010;66(1):57-68.
10. Kimura H, Yamamoto T, Sakai H, Sakai Y, Fujii T. *An integrated microfluidic system for long-term perfusion culture and on-line monitoring of intestinal tissue models.* Lab on a Chip 2008;8(5):741-746.
11. Bhatia SN, Yarmush ML, Toner M. *Controlling cell interactions by micropatterning in co-cultures: Hepatocytes and 3T3 fibroblasts.* Journal of Biomedical Materials Research 1997;34(2):189-199.
12. Tsang VL, Chen AA, Cho LM, Jadin KD, Sah RL, DeLong S, West JL, Bhatia SN. *Fabrication of 3D hepatic tissues by additive photopatterning of cellular hydrogels.* FASEB J. 2007;21(3):790-801.
13. Khademhosseini A, Ferreira L, Blumling Iii J, Yeh J, Karp JM, Fukuda J, Langer R. *Co-culture of human embryonic stem cells with murine embryonic fibroblasts on microwell-patterned substrates.* Biomaterials 2006;27(36):5968-5977.
14. Fukuda J, Khademhosseini A, Yeh J, Eng G, Cheng J, Farokhzad OC, Langer R. *Micropatterned cell co-cultures using layer-by-layer deposition of extracellular matrix components.* Biomaterials 2006;27(8):1479-1486.
15. Titmarsh DM, Chen H, Wolvetang EJ, Cooper-White JJ. *Arrayed cellular environments for stem cells and regenerative medicine.* Biotechnol. J. 2012:n/a-n/a.
16. Titmarsh D, Hidalgo A, Turner J, Wolvetang E, Cooper-White J. *Optimization of Flowrate for Expansion of Human Embryonic Stem Cells in Perfusion Microbioreactors.* Biotechnology and Bioengineering 2011;108(12):2894-2904.
17. Titmarsh DM, Chen H, Glass NR, Cooper-White JJ. *Concise Review: Microfluidic Technology Platforms: Poised to Accelerate Development and Translation of Stem Cell-Derived Therapies.* Stem Cells Translational Medicine 2014;3(1):81-90.

18. Jeon NL, Dertinger SKW, Chiu DT, Choi IS, Stroock AD, Whitesides GM. *Generation of solution and surface gradients using microfluidic systems.* Langmuir 2000;16(22):8311-8316.
19. Lee K, Kim C, Ahn B, Panchapakesan R, Full AR, Nordee L, Kang JY, Oh KW. *Generalized serial dilution module for monotonic and arbitrary microfluidic gradient generators.* Lab on a Chip 2009;9(5):709-717.
20. Sahai R, Martino C, Castrataro P, Menciassi A, Ferrari A, Beltram F, Cecchini M. *Microfluidic chip with temporal and spatial concentration generation capabilities for biological applications.* Microelectron. Eng. 2011;88(8):1689-1692.
21. Titmarsh D, Cooper-White J. Microbioreactor *Array for Full-Factorial Analysis of Provision of Multiple Soluble Factors in Cellular Microenvironments.* Biotechnology and Bioengineering 2009;104(6):1240-1244.
22. Hessel V, Löwe H, Schönfeld F. *Micromixers—a review on passive and active mixing principles.* Chemical Engineering Science 2005;60(8–9):2479-2501.
23. Stone HA, Stroock AD, Ajdari A. *Engineering flows in small devices.* Annual Review of Fluid Mechanics 2004;36(1):381-411.
24. Meijer HEH, Singh MK, Kang TG, den Toonder JMJ, Anderson PD. *Passive and Active Mixing in Microfluidic Devices.* Macromolecular Symposia 2009;279(1):201-209.
25. Unger MA, Chou H-P, Thorsen T, Scherer A, Quake SR. *Monolithic Microfabricated Valves and Pumps by Multilayer Soft Lithography.* Science 2000;288(5463):113-116.
26. Schonfeld F, Hessel V, Hofmann C. *An optimised split-and-recombine micro-mixer with uniform 'chaotic' mixing.* Lab on a Chip 2004;4(1):65-69.
27. Stroock AD, Dertinger SKW, Ajdari A, Mezić I, Stone HA, Whitesides GM. *Chaotic Mixer for Microchannels.* Science 2002;295(5555):647-651.
28. Kee SP, Gavriilidis A. *Design and characterisation of the staggered herringbone mixer.* Chemical Engineering Journal 2008;142(1):109-121.
29. Di L, Fei H, Yang L, Jintian L, Changning L, Jiangxin S, Ya C. *Three-dimensional staggered herringbone mixer fabricated by femtosecond laser direct writing*. Journal of Optics 2013;15(2):025601.
30. Allazetta S, Hausherr TC, Lutolf MP. *Microfluidic Synthesis of Cell-Type-Specific Artificial Extracellular Matrix Hydrogels.* Biomacromolecules 2013;14(4):1122-1131.
31. Cha C, Oh J, Kim K, Qiu Y, Joh M, Shin SR, Wang X, Camci-Unal G, Wan K-t, Liao R and others. *Microfluidics-Assisted Fabrication of Gelatin-Silica Core–Shell Microgels for Injectable Tissue Constructs.* Biomacromolecules 2013;15(1):283-290.
32. Kim JH, Jeon TY, Choi TM, Shim TS, Kim S-H, Yang S-M. *Droplet Microfluidics for Producing Functional Microparticles.* Langmuir 2013;30(6):1473-1488.
33. Baah D, Floyd-Smith T. *Microfluidics for particle synthesis from photocrosslinkable materials.* Microfluidics and nanofluidics 2014;17(3):431-455.
34. Teh S-Y, Lin R, Hung L-H, Lee AP. *Droplet microfluidics.* Lab on a Chip 2008;8(2):198-220.
35. Zhao C-X, Miller E, Cooper-White JJ, Middelberg APJ. *Effects of fluid–fluid interfacial elasticity on droplet formation in microfluidic devices.* AIChE Journal 2011;57(7):1669-1677.
36. Xia YN, Whitesides GM. *Soft Lithography.* Angew. Chem., Int. Ed. 1998;37:550-575.
37. Monahan J, Gewirth AA, Nuzzo RG. *A Method for Filling Complex Polymeric Microfluidic Devices and Arrays.* Analytical Chemistry 2001;73(13):3193-3197.
38. Carpenter A, Jones T, Lamprecht M, Clarke C, Kang I, Friman O, Guertin D, Chang J, Lindquist R, Moffat J and others. *CellProfiler: image analysis software for identifying and quantifying cell phenotypes.* Genome Biology 2006;7(10):R100.

39. Frith JE, Titmarsh DM, Padmanabhan H, Cooper-White JJ. *Microbioreactor Array Screening of Wnt Modulators and Microenvironmental Factors in Osteogenic Differentiation of Mesenchymal Progenitor Cells.* PLoS ONE 2013;8(12):e82931.
40. Dominici M, Le Blanc K, Mueller I, Slaper-Cortenbach I, Marini FC, Krause DS, Deans RJ, Keating A, Prockop DJ, Horwitz EM. *Minimal criteria for defining multipotent mesenchymal stromal cells.* The International Society for Cellular Therapy position statement. Cytotherapy 2006;8(4):315-317.
41. McBeath R, Pirone DM, Nelson CM, Bhadriraju K, Chen CS. *Cell Shape, Cytoskeletal Tension, and RhoA Regulate Stem Cell Lineage Commitment.* Developmental Cell 2004;6(4):483-495.
42. Jaiswal N, Haynesworth SE, Caplan AI, Bruder SP. *Osteogenic differentiation of purified, culture-expanded human mesenchymal stem cells in vitro.* Journal of Cellular Biochemistry 1997;64(2):295-312.
43. Ralf S, Martin B, Thomas P, Stephan H. *Droplet based microfluidics.* Reports on Progress in Physics 2012;75(1):016601.
44. Atencia J, Beebe DJ. *Controlled microfluidic interfaces.* Nature 2005;437(7059):648-655.
45. Fu T, Wu Y, Ma Y, Li HZ. *Droplet formation and breakup dynamics in microfluidic flow-focusing devices: From dripping to jetting.* Chemical Engineering Science 2012;84(0):207-217.
46. Nie Z, Seo M, Xu S, Lewis P, Mok M, Kumacheva E, Whitesides G, Garstecki P, Stone H. *Emulsification in a microfluidic flow-focusing device: effect of the viscosities of the liquids.* Microfluidics and nanofluidics 2008;5(5):585-594.
47. Baroud CN, Gallaire F, Dangla R. *Dynamics of microfluidic droplets.* Lab on a Chip 2010;10(16):2032-2045.
48. Rondeau E, Cooper-White JJ. *Biopolymer Microparticle and Nanoparticle Formation within a Microfluidic Device.* Langmuir 2008;24(13):6937-6945.
49. Maisonneuve BGC, Roux DCD, Thorn P, Cooper-White JJ. *Effects of Cell Density and Biomacromolecule Addition on the Flow Behavior of Concentrated Mesenchymal Cell Suspensions.* Biomacromolecules 2013;14(12):4388-4397.
50. Whitesides GM. *The origins and the future of microfluidics.* Nature 2006;442(7101):368-373.
51. Hansen C, Quake SR. *Microfluidics in structural biology: smaller, faster… better.* Current Opinion in Structural Biology 2003;13(5):538-544.
52. Stroock AD, McGraw GJ. *Investigation of the staggered herringbone mixer with a simple analytical model.* Philosophical Transactions of the Royal Society of London. Series A: Mathematical, Physical and Engineering Sciences 2004;362(1818):971-986.
53. Aubin J, Fletcher DF, Xuereb C. *Design of micromixers using CFD modelling.* Chemical Engineering Science 2005;60(8–9):2503-2516.
54. Hassell DG, Zimmerman WB. *Investigation of the convective motion through a staggered herringbone micromixer at low Reynolds number flow.* Chemical Engineering Science 2006;61(9):2977-2985.
55. Kim H, Lee JH, Suh H. *Interaction of Mesenchymal Stem Cells and Osteoblasts for in vitro Osteogenesis.* Yonsei Medical Journal 2003;44(2):187-197.
56. Lu Z, Roohani-Esfahani S-I, Wang G, Zreiqat H. *Bone biomimetic microenvironment induces osteogenic differentiation of adipose tissue-derived mesenchymal stem cells.* Nanomedicine: Nanotechnology, Biology and Medicine 2012;8(4):507-515.
57. Rinker TE, Hammoudi TM, Kemp ML, Lu H, Temenoff JS. *Interactions between mesenchymal stem cells, adipocytes, and osteoblasts in a 3D tri-culture model of hyperglycemic conditions in the bone marrow microenvironment.* Integrative Biology 2014;6(3):324-337.

5

High-Throughput Microfluidic Platform for Adherent Single Cell Non-Viral Gene Delivery

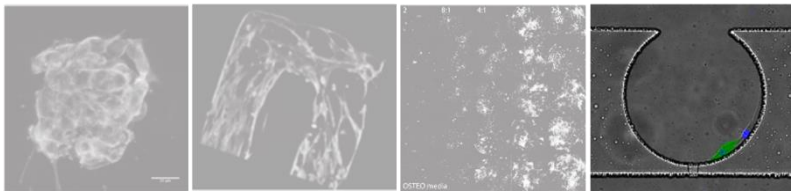

This chapter partially refers to:

High-Throughput Microfluidic Platform for Adherent Single Cell Non-Viral Gene Delivery. Occhetta P, Malloggi C, Gazaneo A, Redaelli A, Candiani G, Rasponi M, RSC Advance, 2015, 5 (7), 5087 – 5095. DOI: 10.1039/C4RA12431F

Rationale

The widespreading of gene therapy as therapeutic tool relies on the development of DNA-carrying vehicles devoid of safety concerns. Opposite to viral vectors, non-viral gene carriers are promising in this perspective, although their low transfection efficiency leads to the necessity of further optimizations. Aiming at overcoming the limitation of traditional macroscale approaches, mainly consisting in time-consuming models relying on the averaged responses from heterogeneous cell populations, we proposed a microfluidic strategy for performing transfection studies on single cells in a high-throughput and deterministic fashion.

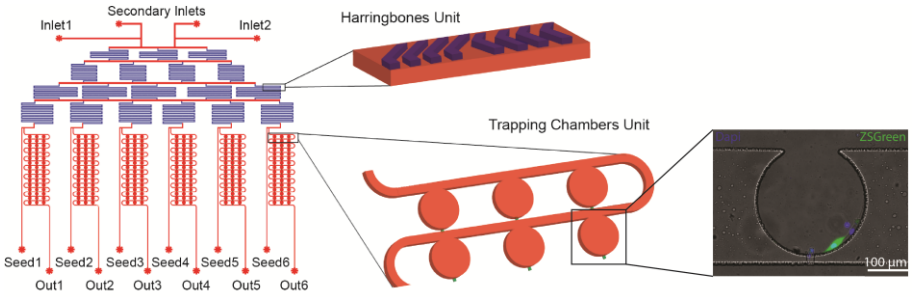

A microfluidic platform was introduced for single cell trapping and culturing, while delivering different combinations/concentrations of non-viral gene vectors for high-throughput screening over their transfection efficacy.

In collaboration with the Biocompatibility and Cell culture Laboratory (BioCell, Politecnico di Milano, Italy) - we combined the ability to trap and culture single cells in precise spatial configurations with the capability of automatically deliver patterns of gene vectors. At this aim, the functionality of the cell mixer introduced in the previous chapter was extended to the generation of linear dilutions of non-viral gene vectors (i.e. polymer/DNA complexes, polyplexes), while adapting channel dimensions for dealing with the single cell scale size.

5.1 Introduction

Gene therapy has opened new scenarios in treating diseases compared to conventional therapeutic strategies by modifying and controlling protein expression of target cells through the introduction of specific genetic material [1]. Being DNA and RNA negatively charged biopolymers, the direct delivery of naked nucleic acids to cells is the least efficient approach. To overcome such a limitation, recent advances in materials science and biotechnology have enabled the development of a variety of systems for the delivery of nucleic acids to cells. Non-viral vectors display striking advantages over viral vectors (i.e. lower cytotoxicity, lower to no immunogenicity and greater ease of preparation and handling) [2]; on the other hand, they still require further optimization in terms of transfection efficiency [3,4]. Non-viral gene delivery vectors are inherently cationic at physiological pH, thus they spontaneously organize with nucleic acids in nano- and micro-particles. In this scenario, the research for optimized and innovative non-viral gene vectors through conventional bench-top systems – such as cell cultures in multiwell plates– is time-consuming, demands relatively large quantities of materials and allows for simultaneously testing only a limited number of materials and parameters. Moreover, such traditional approaches rely on averaging data from heterogeneous cell populations, thus being suboptimal for assessing individual cell responses to exogenous stimuli, such as transfection [5]. In the last years, great interest has thus been focused on single cell analysis and screening, which represents a promising tool aiming at pursuing the direct and deterministic control over cause-effect relationships guiding cell behaviour [6]. However, the analysis on single cells still presents a variety of challenges. First, in order to obtain statistically significant responses, the ability to handle a large number of individual cells in a high-throughput fashion is crucial [7]. Moreover, the capability of reliably allocate individual cells in well-defined locations is crucial for subsequent analyses, often implying the tracking of cells throughout the culture period [8]. Finally, the typical size of features needed to address individual cells demands more strict requirements with respect to standard culture tools in terms of sensitivity, selectivity and temporal resolution [9].

Recent advances in microtechnologies and microfabrication are offering increasing cues for addressing these challenges. Moreover, the reduction of scale leads to unique fluidic phenomena, e.g. the increasing of surface-to-volume ratios, which results in shorter reaction times, higher efficiencies, and lower material consumption [10]. In the last few years, several

strategies have been proposed for single cell manipulations within microfluidic devices, being exploited in a number of applications in the field of cell biology [11]. However, these approaches for trapping single cells require complex and expensive fabrication procedures mostly due to the necessity of multi-layered devices [12,13]. As an alternative, small trapping units were recently proposed [14-17] to block cells along their fluidic path; however their integration with chambers for subsequent culture is not trivial. An interesting approach allowing for trapping and culturing single cells within a microfluidic devices was recently showed by Hong and colleagues [8], which was based on a variable resistance mechanism – the cells functioning as fluid stopper once trapped– at the outlet of a culture chamber. However, the strict requirement in terms of feature sizes did not allow for using conventional photolithographic techniques thus preventing design reproducibility (chemical etching of SU8 photoresist was used to obtain feature sizes of about 3µm).

Herein, based on a similar principle, a low cost and single-layer PDMS microfluidic platform is presented for isolation and culture of a large number of individual adherent cells into defined spatial configurations. The single cell trapping unit was optimized aiming at overcoming issues on fabrication reproducibility, while maintaining high trapping efficacy. Moreover, the upstream integration of a serial dilution generator (SDG) based on a chaotic mixing scheme (based on the concept presented in Chapter 4) allowed for the first time to combine the capability of trapping single cells with the ability of delivering them both soluble factors and non-diffusive particles (i.e. polymer/DNA complexes, polyplexes) under spatio-temporally controlled chemical patterns. Herein, we provide the first proof-of-principle demonstration with a typical transfectant that our microfluidic device can be used proficiently for the forthcoming optimizations of the whole variety of gene delivery vectors. Such platform may thus represent a powerful tool for the implementation of non-viral gene transfection protocols allowing for (i) testing multiple conditions in an automatic and high-throughput fashion, while (ii) directly monitoring gene transfer efficiency and toxicity through "on-off" direct investigations over single cell behaviour.

5.2 Microfluidic platform design and fabrication

In the following paragraphs, the design and fabrication steps of the presented microfluidic platform are detailed. The device concept mainly consists in two "building elements": the trapping chamber (5.2.1 and 5.2.2) and the chaotic based SDG (5.2.3). For both functional units, concept and CFD optimization are reported. Finally, based on computational results, an optimized final platform layout is presented and fabrication steps detailed in paragraph 5.2.4.

5.2.1 Single cell trapping: concept

A microfluidic unit layout was designed aiming at trapping single adherent cells while ensuring enough space for their subsequent growth (Fig5.1a-c).

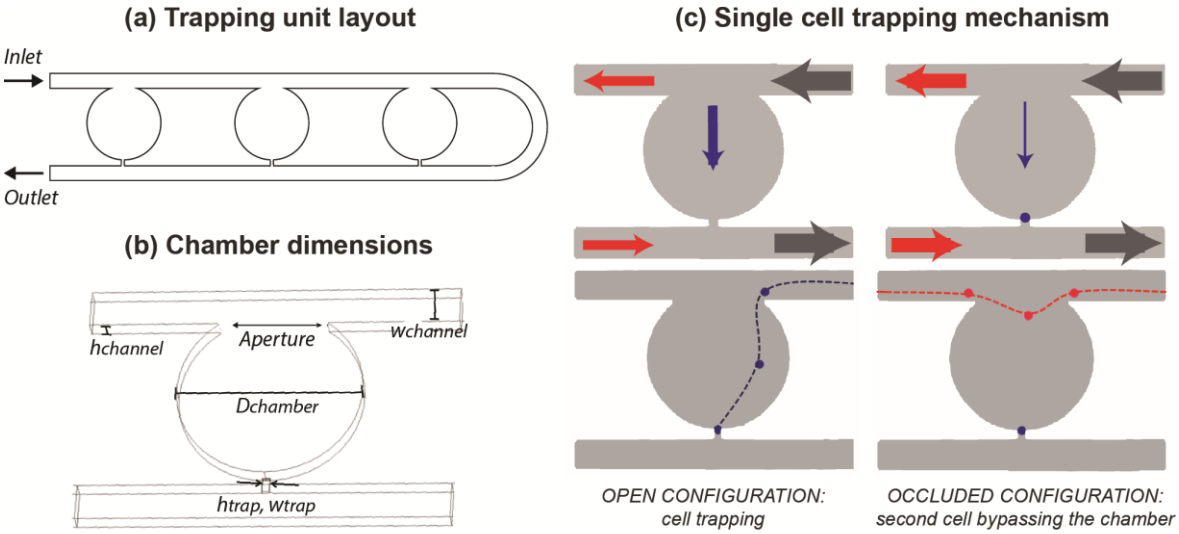

Figure 5.1. *A trapping unit layout was designed for single cell trapping, consisting in three round-shaped culture chambers connected by a curved main channel (a). Each chamber, featuring a diameter of 250µm and a height of 25µm, presents two connections with the main channel: an upstream aperture and a downstream smaller trapping junction (b). The mechanism of trapping exploits an automatic variation of hydraulic resistance within the chamber (c). While in the open configuration the incoming cell can enter the chamber and be trapped (blue path), the subsequent occlusion of the trap through the cell body causes a reduction of inflow into the chamber (blue arrows), thus inhibiting the entrance of further cells (red trajectory).*

A single cell trapping mechanism was thus implemented exploiting an automatic variation of hydraulic resistance within the chamber [8]. In details, a circular culture chamber (Φ=250µm, h=25µm) was conceived provided with two connections to a main fluidic path: (i) an upstream wide opening, which allows for both transportation of cells and diffusion of media/conditioning factors, and (ii) a downstream trapping junction which modulates the hydraulic resistance. The mechanism of trapping is schematically depicted in Fig.5.1c.

Briefly, a cell entering the chamber follows the flow stream, eventually reaching the trapping junction (blue trajectory); the subsequent partial, or total, occlusion of the trap causes an increase in terms of hydraulic resistance, and, in turn, a reduction of inflow into the chamber (blue arrow), thus inhibiting the entrance of further cells (red trajectory).

5.2.2 Singe cell trapping: computational optimization of the chamber geometry

The geometry of the chamber was optimized for single cell trapping by means of Computational Fluid Dynamic modeling (CFD, Comsol Multiphysics). For ease of microfabrication, heights of both fluidic (consisting on flow channels and culture chambers) and trapping layers were fixed at 25μm and 5μm, respectively. Finite element analyses were performed on a 3D model of a fluidic unit, consisting of three culture chambers (provided with trapping elements), and a curved main channel (upstream and downstream) (Fig.5.1a). Trapping junctions were modeled as rounded shaped elements, with the aim of minimizing the trapping effective area, while matching fabrication requirements. Different unit layouts were analyzed, all potentially compatible with standard fabrication techniques, aiming at achieving the highest trapping efficacy, while maintaining the selectivity for individual cell trapping. In details, eight geometries were considered, as combinations of four different widths for the fluidic channels (25, 50, 75 and 100μm) and two widths for the trapping junctions (10 and 15μm) (see Table 5.1).

Table 5.1. *Chamber layouts analyzed by means of CFD model. The layouts differ for both the channel and the trap width, while maintaining constant the channel and the trap height at 25μm and 5μm, respectively.*

Chamber Layout	Channel width [μm]	Trap width [μm]
1	25	10
2	25	15
3	50	10
4	50	15
5	75	10
6	75	15
7	100	10
8	100	15

Furthermore, each configuration was characterized by either the absence or presence of trapped cells –namely open and occluded configurations, respectively–, modeled as solid spheres (diameter either of 10 or 16μm), slightly intersecting the boundaries in proximity of the trapping element. Geometries were discretized through a tethraedrical mesh scheme,

consisting of about $450x10^3$ and $670x10^3$ elements, for occluded and open configurations, respectively. The flow field was computed by solving stationary Navier–Stokes equations for incompressible fluids, setting the density and the viscosity equal to those of water at 25°C (1000 kg/m^3 and 0.890 cP, respectively). A uniform velocity profile was applied to the inlet, corresponding to a total inflow of 0.2µL/min, while a zero pressure condition was set to the outlet. A no-slip condition was applied to boundary walls. Convergence criterion was satisfied when the normalized residuals for the velocities fell below 1×10^{-6}.

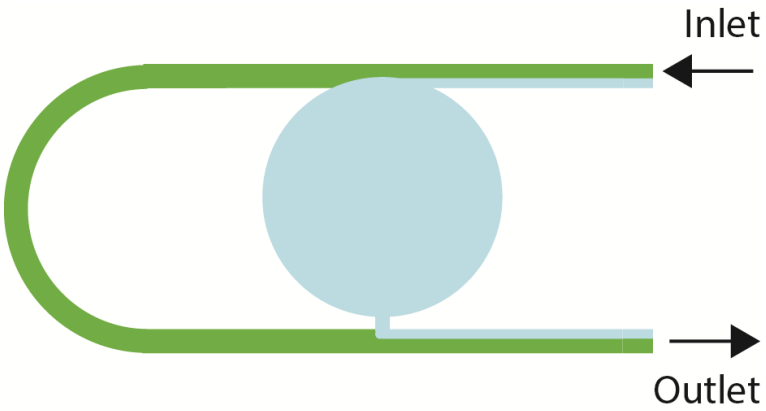

Figure 5.2. *Schematic representation of the partition of the circulating flow in the proximity of a chamber opening. The total fluid flow splits into two different fluidic paths, one entering the chamber (light blue lane) and the other still flowing in the main channel (green lane). The portion of the flow entering the chamber (Q_{in}) depends both on the main channel geometry and on the percentage of occlusion of the trapping junction.*

The inflow entering each chamber was assessed in both open and occluded configurations. In details, a schematic representation of the flow partition within a trapping chamber is shown in Fig.5.2. At each flow rate, the portion of the flow entering the chamber (Q_{in}), depicted as a light blue lane in Fig.5.2, depends both on the main channel geometry and on the percentage of occlusion of the trapping junction. The main channel can thus be divided in two distinct lanes, one entering the chamber (and having a width roughly proportional to Q_{in}) and the other bypassing it. In typical microfluidic flows, round suspended particles (i.e. cells) tend to follow the streamline ideally passing through their center of mass (CM). However, particle's CM cannot approach walls to a distance shorter than the particle radius, thus the minimum Q_{in} required to bring cells into a chamber corresponds to an entering lane (light blue, Fig.5.2) as wide as the particle's radius (Q_{lim}). Ideally, the more Q_{in} is above Q_{lim} the higher are the occurrences of cells entering the chambers (and eventually being trapped), and *viceversa*. As a consequence, for a geometrical

configuration to properly trap single cells, the following conditions must apply: $Q_{in} > Q_{lim}$ in open configuration, and $Q_{in} < Q_{lim}$ in the occluded configuration.

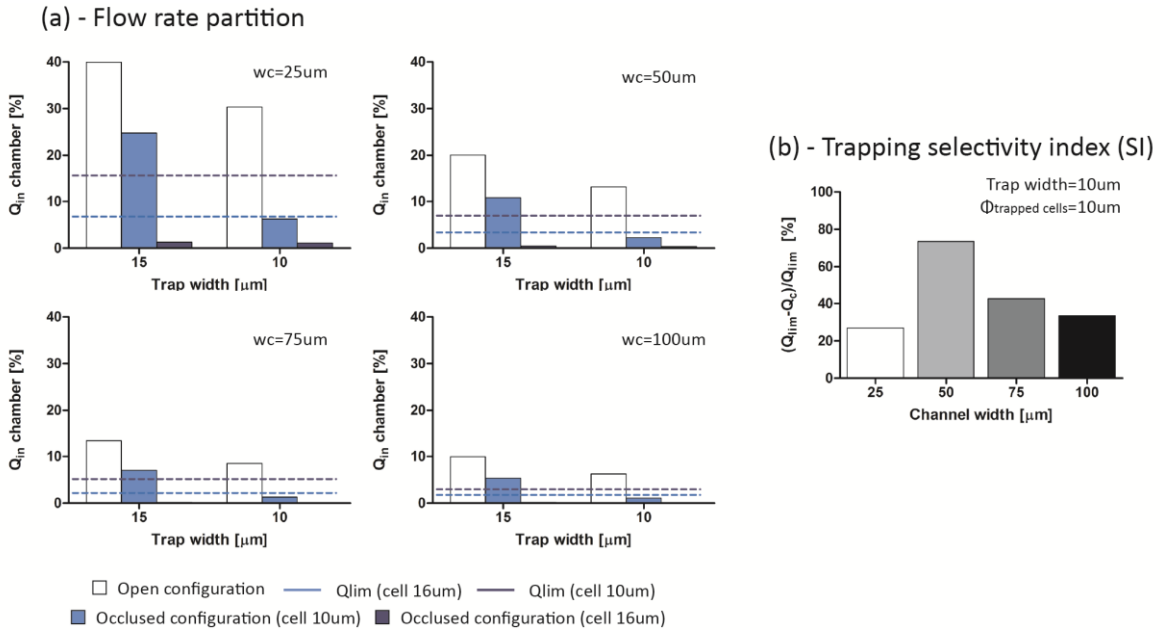

Figure 5.3. *Distribution of the flow rate inside chamber in open and closed configurations (for both 10μm and 16μm trapped cells) for the eight considered layouts. The results were then compared with Qlim (a). Trapping selectivity index trend for the layouts featuring 10μm wide traps considering trapped cells with a diameter of 10μm (b).*

Q_{lim} values were numerically estimated and compared to Q_{in} (Fig.5.3a). For all the considered combinations of channels and traps, Q_{in} resulted higher than Q_{lim}, thus indicating all configurations as compatible with the trapping of cells in the selected size range (Φ=10-16μm). Regarding the occluded configuration, different results were obtained based on the diameter of simulated trapped cells. For bigger cells (Φ=16μm) Q_{in} resulted smaller than Q_{lim} for all combinations, indicating their ability to trap single cells. For smaller cells (Φ=10μm), only the smaller trap configuration was able to catch single cells, while occluded large traps failed to reduce the inflow below Q_{lim} thus being unsuitable to isolate single cells. Indeed, despite the height of the trapping junction (5μm) is small enough to physically block a cell, its relatively large width (15μm) does not allow a sufficient occlusion when smaller cells are considered. As a consequence, 10μm wide traps resulted more effective in trapping single cells over a broader range of cell sizes, and this trap dimension was chosen for following analyses.

In order to identify the width of the main channel, an index of robustness, named selectivity index (SI), was further defined as the percentage difference between Q_{lim} and Q_{in} in each occluded configuration:

$$SI = 100 * \frac{(Qlim - Q_{in})}{Qlim}$$

Larger SI indexes indicate higher probability to inhibit cell entrance in a chamber where a cell is already blocking its trap. SI indexes were evaluated considering occlusions with cells having a diameter of 10µm. As shown in Fig.5.3b, the 50µm wide channel maximized trap selectiviy, yielding the highest probability to only trap single cells.

Results of the CFD analysis thus underlined an optimal configuration in terms of trapping efficacy; featuring 10µm wide trapping junctions and 50µm wide main channel. The optimal geometry was integrated in the final platform and used for experimental validations.

5.2.3 Chaotic mixer serial dilution generator: concept and CFD optimization

A serial dilution generator (SDG) provided with chaotic enhanced mixing features was integrated to the microfluidic platform for mixing both soluble factors (i.e. growth factors) and non-diffusive assemblies (i.e. polyplexes), splitting an initial concentrated solution into 6 linear dilutions (from 0% to 100% in steps of 20%). The chaotic mixer SDG was designed based on a resistive flow model consisting of symmetric microfluidic networks [18] composed of thin channels (60µm wide and 25µm tall) whose lengths were dimensioned to allow diffusive mixing of soluble factors. Furthermore, aiming at mixing non-viral gene vectors which feature diameters ranging from 100nm to 1µm [19-21], staggered herringbone (HB) grooves were integrated on top of the channels [22]. Each HB was designed 24µm wide and 9µm high, being an HB unit constituted of eight HBs changing their orientation between half cycles. The mixing efficiency was computed through finite element analysis by means of Computational Fluid Dynamic models (Comsol Multiphysics). A T junction was designed to merge two different fluids, and a series of straight mixing elements were added downstream. The mixing elements were either repeating HB units (each 416µm long) or rectangular cross-sectional channels as controls. The geometries were discretized with a tethraedrical mesh scheme, consisting of about $195x10^3$ and $20x10^3$ elements, in the case of presence and absence of HB respectively. The flow field was computed by solving stationary

Navier–Stokes equations for incompressible flow, setting the density and the viscosity equal to those of water at 25°C (1000 kg/m^3 and 0.890 cP, respectively). Uniform velocity profiles were applied to the inlets, corresponding to Reynolds numbers (Re) comprised between 0.1 and 10 (Q=0.255-25.5µl/min), while a zero pressure condition was set to the outlet. A no-slip condition was applied to the boundary walls. Convergence criterion was satisfied when the normalized residuals for the velocities fell below 1×10^{-6}. The injection of two differently concentrated non-diffusive species was performed into the inlets, and the profiles of concentration in all output channels were computed by means of the Transport of Diluted Species application module.

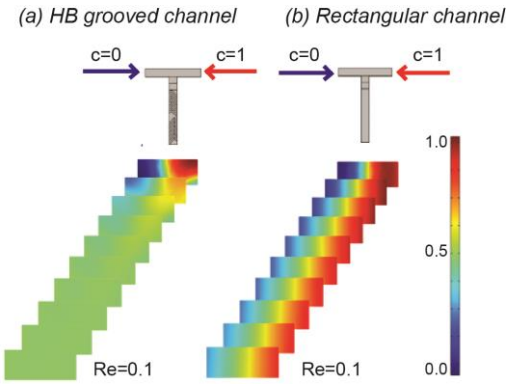

Figure 5.4. *Staggered herringbone (HB) grooves were integrated on the top of the SDG channels for enhancing the mixing of non-diffusive entities. CFD simulations were computed to verify the mixing efficacy of such structures (a) in comparison with rectangular channels (b). A complete mixing between two differently concentrated non-diffusive species was achieved flowing through a 4.2mm long HB grooved channel (a), while no mixing is observed for a rectangular channel featuring the same length (b). Showed results were obtained for Re=0.1.*

Fig.5.4 shows the trend of concentrations for Re=0.1, demonstrating the achievement of a complete mixing of species through the repetition of only ten HBs units (total length=4.2mm) (a), while no significant mixing was detectable in a rectangular channel featuring the same total length (b). The addition of HB grooves thus demonstrated to enhance the mixing of non-diffusive entities and, in the same time, require a lesser occupation of footprint in the device area.

5.2.4 Fabrication of the microfluidic platform

The final chip layout was designed integrating the computationally optimized versions of both the trapping chamber and the HBs mixing unit. In details, the final microfluidic platform featured an upstream chaotic mixer serial dilution generator, which independently delivered six linear dilutions to six downstream culture units (Fig.5.5a).

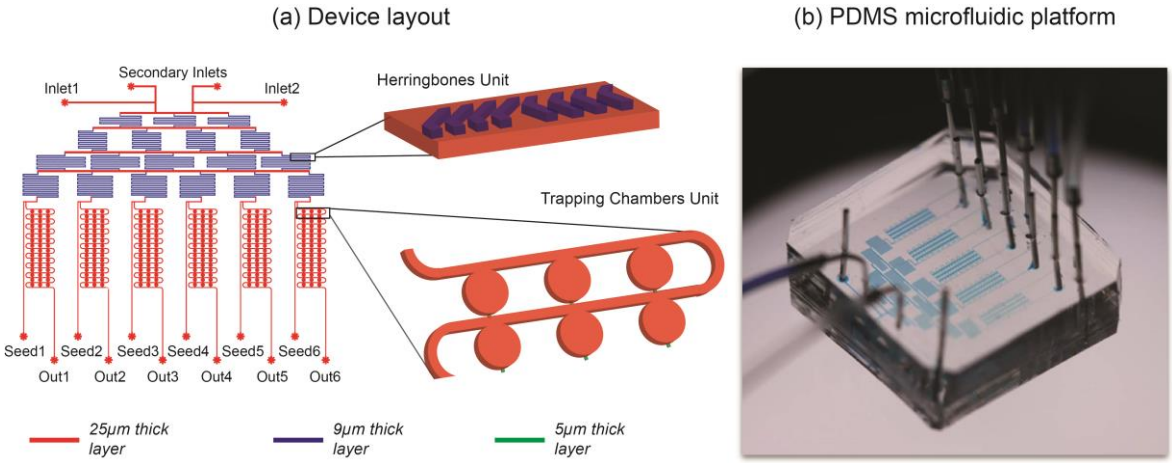

Figure 5.5. *Microfluidic device final layout (a) and fabrication (b). The chip platform consisted of (i) a serial dilution generator integrated with herringbone units for chaotic mixing and (ii) a culture area comprising six parallel units. Each culture unit consisted of 48 single cell trapping chambers and was combined with a lateral seeding channel. Three layers were integrated in the layout: (i) a rectangular 25μm thick layer constituting both fluidic channels and chambers (red features); (ii) a rectangular 9μm thick layer for the HB structures (blue features), and (iii) a 5μm thick layer for the trapping junctions, rendered round shaped after the fabrication re-flow process (green features).*

Each culture unit consisted in the repetition of 48 single trapping chambers (trap size 10μm), connected through a main channel 50μm wide, and integrated with a lateral seeding channel. Two secondary inlets were finally included in the layout to facilitate the medium change operations. The layout was finalized with CAD software (AutoCAD, Autodesk Inc.) and the corresponding master mold was realized through standard photolithography techniques [23]. In particular, three layers were integrated: (i) a 25μm thick layer constituting both fluidic channels and chambers (Fig.5.5a, red features); (ii) a 9μm thick layer for the HB structures, positioned on the top of the previous one (Fig.5.5a, blue features), and (iii) a 5μm thick layer for the trapping junctions, reflowed to achieve a rounded cross-section (Fig.5.5a, green features).

Microfluidic devices (Fig.5.5b) were obtained by replica molding of PDMS (Sylgard® Dow Corning) on the master mold. Briefly, PDMS was cast on the mold in ratio 10:1 w/w (pre-polymer to curing agent), degassed and cured at 80°C for 3hr. Input and output ports were obtained through a 0.5mm biopsy puncher (Harris Uni-Core™) and the PDMS chip was finally permanently bonded to a glass slide (25x75x1mm) upon a 1min of air plasma treatment (Harrick Plasma).

5.3 Microfluidic platform experimental validation

In the following paragraphs, the two main envisioned functionalities of the proposed microfluidic platform are experimentally validated. Single cell trapping efficacy and capability of culturing single cells, allowing for further proliferation are first presented (5.3.1). Moreover, the effective ability of generating linear dilution of non-viral gene vectors by means of the chaotic based SDG is showed (5.3.2).

5.3.1 Single cell trapping and culturing within microfluidic device

Preliminary biological experiments were conducted on the computationally optimized platform to evaluate the trapping efficiency and the device compatibility for adherent single cell cultures.

U87-MG (human glioblastoma-astrocytoma epithelial-like, Φ=15.4±2.5μm) cell line was purchased from the American Type Culture Collection (ATCC, Manassas, VA, USA). Cells were cultured at 37°C in a humidified atmosphere containing 5% CO_2 in Dulbecco's Modified Eagle Medium (DMEM, Sigma-Aldrich, Milano, Italy) supplemented with 1mM sodium pyruvate, 10mM HEPES buffer, 100U/mL penicillin, 0.1mg/mL streptomycin, 2mM glutamine, and 10% (v/v) FBS (hereafter referred as to complete DMEM).

Before cell seeding, microfluidic devices were sterilized by autoclaving (121°C, 20mins, wet cycle) and subsequently dried overnight at 80°C. To favor cell adhesion on the glass substrate, devices were air plasma treated for 5mins to increase the hydrophilicity and subsequently perfused overnight at 37°C with a 0.01% (w/v) Poly-L-Lysine (PLL) solution (Sigma-Aldrich, Milano, Italy) at a flow rate of 30μL/hr. After rising in PBS, complete DMEM was perfused from the two main inlets. Trypsinized U87-MG cells were diluted to a concentration of 2x105 cells/mL and a single cell suspension was obtained by means of a cell strainer (40μm, Falcon®). Cells were then contemporarily seeded within the six culture units by perfusing the cell suspension through the seeding channels at a constant flow rate of 0.2μL/min for 5mins and subsequently rising with fresh medium. Phase contrast images were acquired by means of Leica DMIRD inverted microscope. The dynamics of the cell trapping mechanism and the kinematics of cells while being trapped were further monitored by means of a high-speed camera (Phantom Miro, NJ, USA) (Fig.6.6).

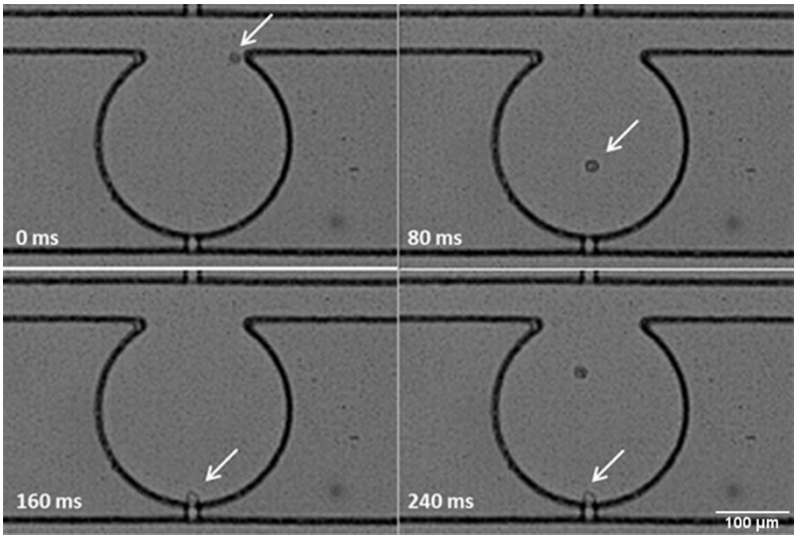

Figure 5.6. *Single cell trapping dynamics within a chamber: the proposed trapping mechanism allowed for selectively trapping single cells within milliseconds.*

Single cell trapping efficacy was then calculated as the percentage of chambers containing a single cell over the total number of chambers *per* culture unit. Moreover, to define the specificity of the proposed approach the percentage of chambers containing either i) multiple cells blocked within a trap or ii) one or more cells out of the trap was assessed and compared with the single cell trapping efficacy (Fig.5.7). Noteworthy, the overall percentage of chambers filled with cells per unit was 47.8±12.2% (Fig.5.9a), whose 39.8±6.2% chambers featured single cell entrapped, 6.2±4.2% multiple cells entrapped and 1.7±2.4% one or more cells out of trap (Fig.5.8).

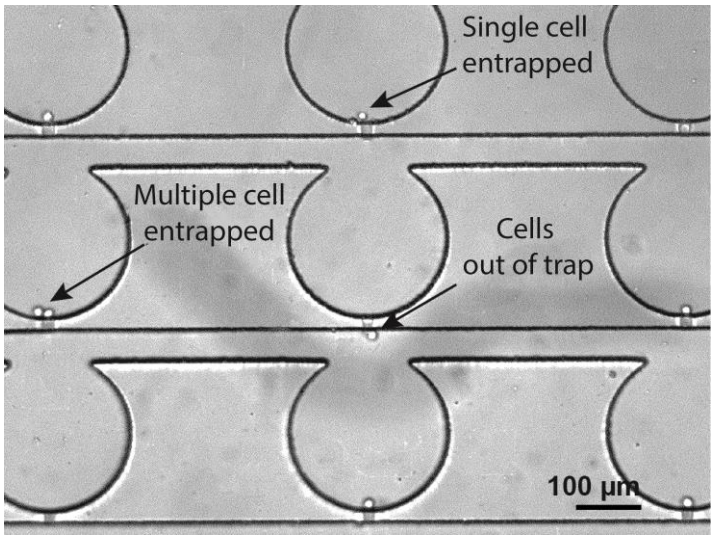

Fig.5.7. *The percentage of filled chambers after the seeding was calculated as the sum of three different possible occurrences, all depicted in this picture: 1) a single cell blocked within the trap; 2) multiple cells blocked within a trap; 3) the presence of cells out of the trap.*

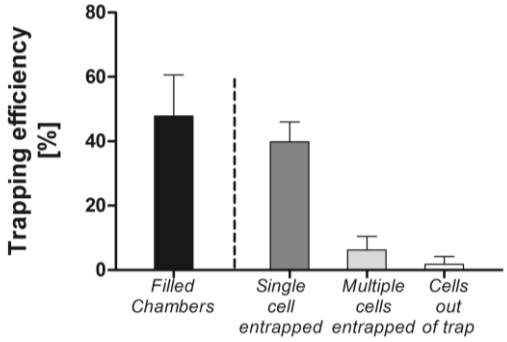

Fig.5.8. *Upon U87-MG cell seeding, the overall percentage of chambers filled with cells per culture unit was 47.8±12.2%, whose 39.8±6.2% chambers featured single cell entrapped, 6.2±4.2% multiple cells entrapped and 1.7±2.4% on or more cells out of trap (n=7).*

Upon cell injection, seeding channels were clamped and a continuous flow rate of 2μL/hr per culture line was imposed. The microfluidic platform was incubated under standard culture conditions and cultured for 5 days, periodically monitoring cell adhesion and proliferation. The single cells seeded within the device took 4hrs to adhere completely to the PLL-functionalized substrate (Fig.5.9b), whereas cell proliferation was apparent only 48hrs after seeding (Fig.5.9b). Most important, the cells did generally maintain high viability, as highlighted by the proper elongated phenotype shown, for up to 5days in culture.

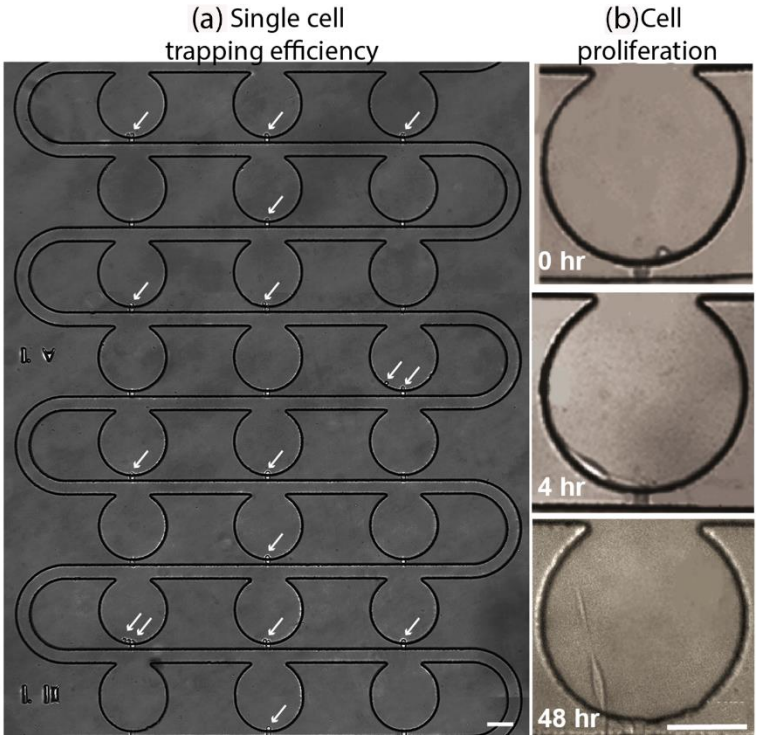

Figure 5.9. *The proposed mechanism allowed trapping cells within defined spatial configurations, leading to trapping efficiencies per unit of 39.8±6.2% for single cells (underlined with single arrows) and 6.2±4.2% for multiple cells (underlined with multiple arrows) (a). Trapped cells started to adhere after 4hrs from the seeding, while proliferation was detected within the first 48hrs (b). (Scale bars=100μm)*

5.3.2 Experimental validation of the chaotic mixer SDG

The dilution patterns generated by the chaotic mixer serial dilution generator were experimentally assessed for both soluble species and non-diffusive particles and compared with those obtained through an equivalent diffusive SDG featuring non-grooved channels. In details, for testing the diffusive mixing of soluble species, a blue dye solution was pumped into either inlet at a flow rate of 36µL/hr while distilled water (dH2O) into the other one, as exemplified in Fig.5.5b. Upon the achievement of a steady state condition, three samples of 20µl of dilution were collected from each outlet and the average emission wavelength for each dilution was quantified by means of a spectrophotometer (NanoDrop 2000c, Thermo Scientific, Wilmington, USA). Experiments were carried out on three different devices (n=3) and compared with expected values. For both the SDG configurations, emission wavelengths of the six dilutions collected from the outlets were measured to match the expected linear distribution with coefficients of determination equal to R^2=0.9891 and R^2=0.9948 for the diffusive SDG and for the chaotic SDG, respectively (Fig.5.10a).

The evaluation of mixing of non-diffusive assemblies was performed for both chaotic and diffusive SDGs by pumping polymer-based non-viral gene vectors through the cmSDG. Briefly, polyplexes were prepared at room temperature (r.t.) by adding ZsGreen plasmid (Clontech Laboratories, Inc., CA, USA) to 25kDa linear polyethylenimine (lPEI, PolyScience, Pennsylvania, USA) (final plasmid concentration in the transfection suspension: 40ng/mL) in 150mM NaCl at N/P40. The N/P ratio is defined as the molar ratio of the amino groups of the cationic polymer used to complex the phosphate groups of a given amount of DNA. Polyplexes were incubated for 20mins at r.t. before use, finally featuring an average hydrodynamic diameter of 1.37±0.27µm, as determined by Dynamic Light Scattering (DLS, Zetasizer Nano ZS instrument. Malvern, UK). The final polyplex suspension was pumped in the right inlet at a flow rate of 3.75µL/min, corresponding at Re=1, while 150mM NaCl into the left one. After the achievement of a steady state condition, three samples of 1.5µL of dilution were collected from each outlet and DNA concentration was assessed by measuring the absorbance at OD260 by means of a spectrophotometer (NanoDrop 2000c, Thermo Scientific, Wilmington, USA). Results were collected as the average of four devices (n=4) and compared with expected values. The results obtained through the chaotic mixer confirmed the generation of a linear partition of the injected vectors (Fig.5.10b), matching the expected linear distribution (R^2=0.9898). In

contrast, constant concentrations of DNA were measured among the three outlets of the diffusive SDG corresponding to 100%, 80% and 60%, while no DNA was detected for the remaining outlets, thus demonstrating no mixing occurred within the device (Fig.5.10b).

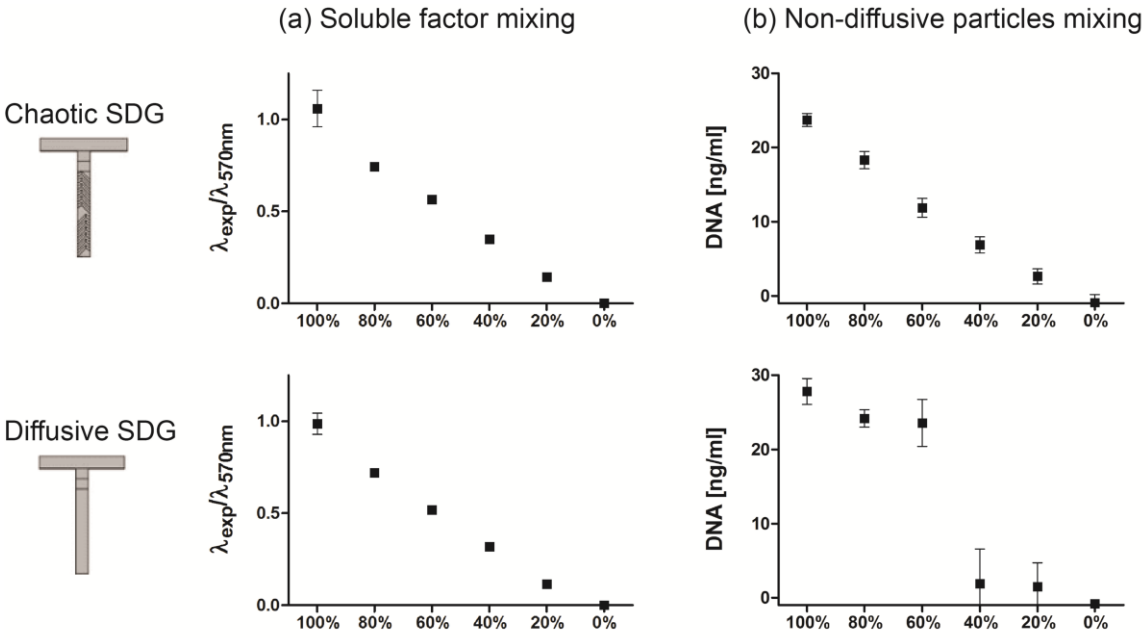

Figure 5.10. *Characterization of chaotic- and diffusive- serial dilution generator (SDG). For assessing the mixing of soluble factors, device were perfused with blue dye solution and dH2O and linear color patterns were obtained for both the configurations (n=3) (a). The mixing of non-diffusive species was validated by mixing non-viral gene vectors and NaCl buffer and measuring the DNA concentration of the dilutions collected at the outlets (n=3). While the chaotic SDG generated a linear pattern of non-viral vectors (R^2=0.9898), within the diffusive SDG no mixing occurred (b).*

5.4 Cell transfection assessment within the microfluidic platform

The proposed single cell microfluidic platform was finally exploited for preliminary experiments of cell transfection. To assess the potentiality of the microfluidic platform as a tool to perform transfection experiments, 25kDa *l*PEI was chosen as one of the most popular and effective polymeric gene delivery vectors, and thus used as a standard in transfection experiments[24-26]. In details, single cells were seeded within the microchambers as previously described and allowed adhering overnight. Twenty-four hours after seeding, the culture medium was replaced with polyplex-containing fresh medium (20ng/μL of ZsGreen plasmid). The microfluidic platform was then incubated at 37°C up to 3 days. Transfected cells were periodically observed and photographed with Zeiss Axioplan microscope for ZsGreen plasmid expression and with Leica DMIRD inverted microscope for cell morphology. Cells were finally fixed by perfusing 4% paraformaldehyde for 20mins, after washing in PBS, and cell nuclei were stained with DAPI. Fluorescence images were acquired directly within the optically transparent glass-PDMS devices.

Fig.5.11 shows a fluorescent image of a transfected ZsGreen-expressing cell detected 12hrs from the exposure. The elongated morphology indicated the complete adhesion of the cell to the substrate and thus its viability. These results, although preliminary, pave the way for the use of such microfluidic device for the high-throughput screening of gene delivery vectors and the optimization transfection protocols.

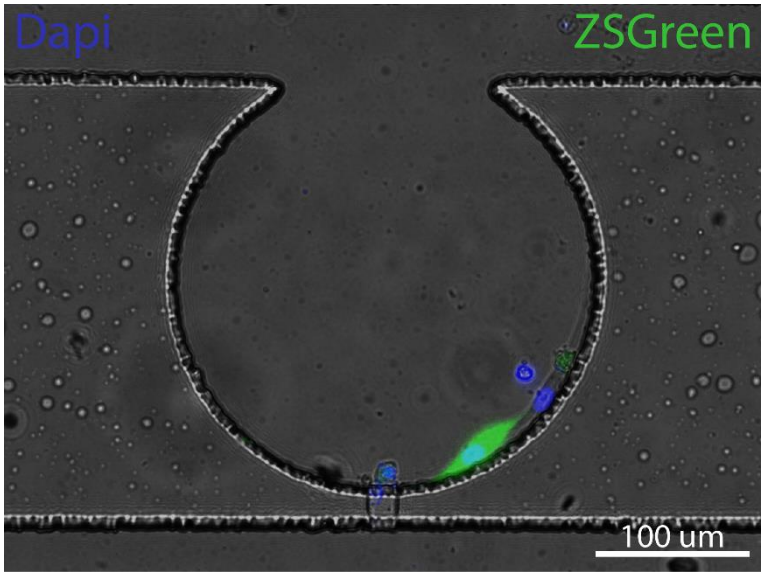

Figure 5.11. *Microscopic observation of a single U87-MG cell transfected with lPEI/ZsGreen plasmid complexes at N/P40. The ZsGreen fluorescence (green) and the DAPI staining (blue) were overlaid onto a contrast image.*

5.5 Discussion

Aiming at the optimization of non-viral based gene delivery strategies [5], the possibility to work at a single cell level allows to directly and deterministically control the efficacy of different transfection stimuli on cell behavior. Although conventional techniques have been exploited for isolating single cells (*i.e.* flow cytometry, capillary electrophoresis) [27], they still suffer from a poor control over the cellular microenvironment. Conversely, microfluidics has proven to be the leading tool for single cell analysis allowing for precise fluid and cell manipulation while featuring a scale-size comparable to the cellular level [9,28]. In addition, microfluidic assays can be easily parallelized for testing several parameters at a time within the same platform. These advantages make them suitable tools for intensive studies aiming at developing optimized and innovative non-viral gene delivery systems in a fast and effective fashion, thus overcoming the limitations of conventional bench-top systems.

In this regards, we computationally designed and experimentally validated a PDMS microfluidic platform for high-throughput single cell analysis, coupling the ability to handle single cells to defined spatial configurations while precisely tailoring the microenvironment around them. The device integrated two functional units: (i) a cell culture area for single cell compartmentalization, consisting of six independent culture units, and that are individually addressable through the lines of (ii) an integrated chaotic serial dilution generator for further conditioning them through spatio-temporally controlled patterns of non-diffusive particles (*i.e.* polyplexes).

To date, existing approaches for trapping single cells within microfluidic devices mainly require either complex actuation systems or expensive fabrication procedures difficult to be replicated in reproducible way [12,13]. Such approaches, which allowed for trapping single cells by actuating integrated valve systems[29] or exploiting physical obstacles as traps[13], have a drawback in terms of device fabrication. Recently a new approach was presented to successfully isolate single cells within small trapping elements [14,30]. While this method was based on trap configurations geometrically optimized for achieving high trapping efficiency, it resulted not suitable for adherent cell cultures, lacking in sufficient space for cell spreading and subsequent proliferation. Thus, the ability to combine both single cell trapping and culturing capabilities in separated chambers still remains an open issue.

Among others, an interesting solution has been recently proposed by Hong S et al. [8], who integrated an easy to handle single cell trapping mechanism, based on passive variation of hydraulic resistances, directly with compartmentalized culture chambers [14]. Although promising, this approach was shown to require non-conventional fabrication approaches to obtain suitable trap dimensions (down to 3µm). Starting from the same principle, we here optimized the trapping chamber geometry in the attempt to match both time reproducible fabrication and trapping efficacy requirements. Culture units were considered, consisting of three fluidically connected round-shaped culture chambers (Φ=250µm, h=25µm) integrated with a downstream trapping junction (h=5µm). Eight geometries were systematically investigated through CFD modeling to maximize the trapping efficacy, while maintaining the selectivity for individual cell trapping over a broad range of cell diameters. The comparison of numerically calculated flow rates entering the chamber in both open and occluded configurations yielded an optimal configuration in terms of trapping efficacy, featuring 10µm wide trapping junctions and 50µm wide main channel. It is worth noting that such optimized configuration featured sizes compatible with standard photolithographic techniques [23], thus overcoming the main limitation of the previous work [8].

The experimental validation further confirmed the computational results. In detail, the proposed trapping mechanism allowed achieving high single cell trapping efficiency (up to 40%), having all six independent culture units simultaneously filled with individual U87-MG cells within few minutes. A flow rate of 0.2µl/min, corresponding to Re 0.1, was chosen to seed the device. Such value was found to be a good compromise between selectivity for capturing single cells and seeding time. Indeed, the use of higher flow rates (around Re 1) increased the possibility for multiple cells to enter the same chamber. At the same time, these flow rates yielded higher pressure drops across traps ends, causing cells deformation and their subsequent escape through the traps, thus in turn worsening the overall trapping efficiency. Conversely, lower flow rates (around Re 0.01) led to longer seeding time, thus enhancing the possibility for cells to aggregate within the perfused suspension and consequently either to be trapped in clusters or to block channels. Noteworthy, at the selected flow rate (0.2µl/min), the occurrence of a chamber entrapping multiple cells was significantly lower than the percentage of single cell filled chambers. Such multiple cell trapping phenomena were also mainly related to cells aggregation before entering the chamber, rather than to the sequential entrapment of multiple cells.

Cells trapped within the device and cultured up to 3 days, exhibited excellent viability and proliferative activity, proving the proposed approach compatible for isolating and culturing adherent single cells within compartmentalized chambers. Moreover, the chambers configuration exhibited enough space for further cell proliferation, which is a fundamental requirement for further transfection experiments. To the best of our knowledge, the preliminary results showed in this study also demonstrated for the first time the possibility to transfect adherent single cell by means of gene vectors within a microfluidic device.

The potentiality of the presented device to culture individual adherent cells in defined spatial configuration and in a high-throughput fashion further allowed for easily tune the chemical environment around them. Indeed, throughout the innovative transfection strategies development stage, the possibility to deliver controlled combinations of vectors in a spatio-temporal controlled manner is crucial for obtaining fast and reliable results. For this purpose, the integrated serial dilution generator was *ad hoc* computationally designed for mixing both soluble factors and non-diffusive entities, which essentially are nano-to-micrometric polyplexes and lipoplexes. Numerical modeling showed that the implementation of herringbone structures[22] within the layout was able to increase the mixing efficiency of large particles even at low Reynolds numbers (Re=1), and therefore such structures were integrated within the final platform. To the best of our knowledge, we here experimentally demonstrated for the first time the generation of linear concentration patterns of DNA vectors within a microfluidic device. By injecting non-viral gene delivery vectors, the establishment of a gradient was quantified through the analysis of the DNA content at each outlet of the six cell culture units. Furthermore, compared to diffusion-based serial dilution generators, the proposed chaotic SDG allowed obtaining reliable linear distribution of polyplexes while maintaining relatively low pressure drops. The integration of this element thus allows extending the potentiality of the device and/or the chaotic SDG module itself for high-throughput screening over a wide range of molecules and particles.

Conclusive remarks

In this chapter, we introduced an innovative microfluidic platform integrating all the required functionalities for the optimization of non-viral gene transfection protocols, allowing for testing multiple conditions (e.g. analyzing and comparing the transfection effect of delivering different polyplex doses, over a variety of dynamic conditions, in diverse culture or buffer media, and in different cell types) in an automatic and high-throughput fashion. The presented preliminary transfection experiments showed the actual possibility to achieve transfection of single cells, thus allowing for directly monitoring the gene transfer efficiency and cytotoxicity by means of an "on-off" investigation at the single cell level. A more exhaustive study is underway in our laboratories to exploit the full potential of this microfluidic device in gene delivery experiments.

In perspective, the presented platform could represent a promising tool also in different application of cell biology, allowing for a deterministic and precise control over cause-effect relationships guiding cell behavior under controlled external chemical stimulations.

References

1. Pezzoli D, Chiesa R, De Nardo L, Candiani G. *We still have a long way to go to effectively deliver genes!* Journal of applied biomaterials & functional materials 2012;10(2).
2. Mehier-Humbert S, Guy RH. *Physical methods for gene transfer: Improving the kinetics of gene delivery into cells.* Advanced Drug Delivery Reviews 2005;57(5):733-753.
3. Vijayanathan V, Thomas T, Thomas TJ. DNA *Nanoparticles and Development of DNA Delivery Vehicles for Gene Therapy*†. Biochemistry 2002;41(48):14085-14094.
4. Thomas CE, Ehrhardt A, Kay MA. *Progress and problems with the use of viral vectors for gene therapy.* Nature Reviews Genetics 2003;4(5):346-358.
5. Schmid A, Kortmann H, Dittrich PS, Blank LM. *Chemical and biological single cell analysis.* Current Opinion in Biotechnology 2010;21(1):12-20.
6. Lindström S, Andersson-Svahn H. *Miniaturization of biological assays — Overview on microwell devices for single-cell analyses.* Biochimica et Biophysica Acta (BBA) - General Subjects 2011;1810(3):308-316.
7. Wang H, Chen H-W, Hupert ML, Chen P-C, Datta P, Pittman TL, Goettert J, Murphy MC, Williams D, Barany F and others. *Fully Integrated Thermoplastic Genosensor for the Highly Sensitive Detection and Identification of Multi-Drug-Resistant Tuberculosis.* Angewandte Chemie International Edition 2012;51(18):4349-4353.
8. Hong S, Pan Q, Lee LP. *Single-cell level co-culture platform for intercellular communication.* Integrative Biology 2012;4(4):374-380.
9. Love KR, Bagh S, Choi J, Love JC. *Microtools for single-cell analysis in biopharmaceutical development and manufacturing.* Trends in Biotechnology 2013;31(5):280-286.
10. El-Ali J, Sorger PK, Jensen KF. *Cells on chips.* Nature 2006;442(7101):403-411.
11. Andersson H, van den Berg A. *Microfluidic devices for cellomics: a review.* Sensors and Actuators B-Chemical 2003;92(3):315-325.
12. Wheeler AR, Throndset WR, Whelan RJ, Leach AM, Zare RN, Liao YH, Farrell K, Manger ID, Daridon A. *Microfluidic device for single-cell analysis.* Analytical Chemistry 2003;75(14):3581-3586.
13. Hanke C, Waide S, Kettler R, Dittrich P. *Monitoring induced gene expression of single cells in a multilayer microchip.* Analytical and Bioanalytical Chemistry 2012;402(8):2577-2585.
14. Lawrenz A, Nason F, Cooper-White JJ. *Geometrical effects in microfluidic-based microarrays for rapid, efficient single-cell capture of mammalian stem cells and plant cells.* Biomicrofluidics 2012;6(2).
15. Yamaguchi Y, Arakawa T, Takeda N, Edagawa Y, Shoji S. *Development of a poly-dimethylsiloxane microfluidic device for single cell isolation and incubation.* Sensors and Actuators B-Chemical 2009;136(2):555-561.
16. Di Carlo D, Aghdam N, Lee LP. *Single-Cell Enzyme Concentrations, Kinetics, and Inhibition Analysis Using High-Density Hydrodynamic Cell Isolation Arrays.* Analytical Chemistry 2006;78(14):4925-4930.
17. Kobel S, Valero A, Latt J, Renaud P, Lutolf M. *Optimization of microfluidic single cell trapping for long-term on-chip culture.* Lab on a Chip 2010;10(7):857-863.
18. Jeon NL, Dertinger SKW, Chiu DT, Choi IS, Stroock AD, Whitesides GM. *Generation of solution and surface gradients using microfluidic systems.* Langmuir 2000;16(22):8311-8316.
19. Goula D, Remy JS, Erbacher P, Wasowicz M, Levi G, Abdallah B, Demeneix BA. *Size, diffusibility and transfection performance of linear PEI/DNA complexes in the mouse central nervous system.* Gene Therapy 1998;5(5):712-717.

20. Ogris M, Steinlein P, Kursa M, Mechtler K, Kircheis R, Wagner E. *The size of DNA/transferrin-PEI complexes is an important factor for gene expression in cultured cells*. Gene Therapy 1998;5(10):1425-1433.
21. van Gaal EVB, van Eijk R, Oosting RS, Kok RJ, Hennink WE, Crommelin DJA, Mastrobattista E. *How to screen non-viral gene delivery systems in vitro?* Journal of Controlled Release 2011;154(3):218-232.
22. Stroock AD, Dertinger SKW, Ajdari A, Mezić I, Stone HA, Whitesides GM. *Chaotic Mixer for Microchannels.* Science 2002;295(5555):647-651.
23. Xia YN, Whitesides GM. *Soft lithography.* Angewandte Chemie-International Edition 1998;37(5):551-575.
24. Dai Z, Gjetting T, Mattebjerg MA, Wu C, Andresen TL. *Elucidating the interplay between DNA-condensing and free polycations in gene transfection through a mechanistic study of linear and branched PEI.* Biomaterials 2011;32(33):8626-8634.
25. Huh S-H, Do H-J, Lim H-Y, Kim D-K, Choi S-J, Song H, Kim N-H, Park J-K, Chang W-K, Chung H-M and others. *Optimization of 25kDa linear polyethylenimine for efficient gene delivery.* Biologicals 2007;35(3):165-171.
26. Pezzoli D, Olimpieri F, Malloggi C, Bertini S, Volonterio A, Candiani G. *Chitosan-Graft-Branched Polyethylenimine Copolymers: Influence of Degree of Grafting on Transfection Behavior.* PLoS ONE 2012;7(4):e34711.
27. Andersson H, van den Berg A. *Microtechnologies and nanotechnologies for single-cell analysis.* Current Opinion in Biotechnology 2004;15(1):44-49.
28. Mu X, Zheng W, Sun J, Zhang W, Jiang X. *Microfluidics for Manipulating Cells.* Small 2013;9(1):9-21.
29. White AK, VanInsberghe M, Petriv OI, Hamidi M, Sikorski D, Marra MA, Piret J, Aparicio S, Hansen CL. *High-throughput microfluidic single-cell RT-qPCR.* Proceedings of the National Academy of Sciences 2011;108(34):13999-14004.
30. Frimat J-P, Becker M, Chiang Y-Y, Marggraf U, Janasek D, Hengstler JG, Franzke J, West J. *A microfluidic array with cellular valving for single cell co-culture.* Lab on a Chip 2011;11(2):231-237.

6

General conclusions

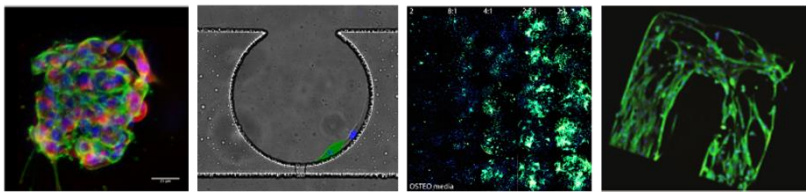

Nowadays, there is an increasing demand for innovative biomedical technologies able to accelerate drug discovery and gene/cell therapy development processes. New strategies are thus needed which allow for the simultaneous improvement of in vitro models accuracy and experimental throughput. Over the past decade, microfluidics has emerged as a promising tool in biology and biomedical research. In particular, its ability to generate advanced microscale cell culture strategies offers insights to speed up and optimize the design and development of novel biopharmaceutical and advanced (cellular or gene-based) therapeutic approaches in an effective way.

In this scenario, this PhD project focused on the development and validation of four microscale platforms for investigations in the cell biology field. All platforms were conceived with the common aim of studying the effects of specific cues from the native cellular microenvironment on stem cell behavior at a biologically relevant size level. To this goal, each platform was ad hoc designed by applying key principles of microfluidics to meet specific biological requirements. In details, different technical solutions were integrated within the proposed platforms to control and screen the effect of combinations/concentrations of soluble factors and solid cues on cultured cells, while featuring high-throughput screening capabilities. Moreover, exploiting the ability to precisely manipulate fluids and particles (i.e. cells) within microchannels, we were able to handle cells in precise spatial and functional configurations, otherwise difficult (or impossible) to achieve through traditional macroscale approaches: from 3D scaffold-free microaggregates, to controlled multicellular environment, down to the single cell level.

Once designed and fabricated, the proposed microfluidic platforms were fully validated. At first, functional evaluations were carried out to investigate their technical performances, and the corresponding outcomes were used to optimize their design. Subsequently, as biological validation, each platform allowed the collection of relevant results in a specific study in cell biology.

Such achievements suggest that the set of microfluidic platforms developed during this PhD project could define a promising tool for different applications, ranging from the optimization of new drugs and gene therapies, to the development of more specific and effective tissue engineering strategies. However, to this ultimate goal, further optimizations have yet to be done.

First, with the final aim to transfer microfluidic technologies to biological, biomedical and pharmaceutical research and development fields, the proposed final systems should ideally be highly automatized and feature user-friendly interfaces, in order to be easily translatable to non-specialized users. For this reason, a first required step forward will be the optimization of the proposed devices, introduced here as research laboratory prototypes, toward the generation of more automatic and accessible platforms, characterized by intuitive sequences of operations and easily interpretable outcomes.

Moreover, a possible step forward is represented by the integration of two (or more) of the different approaches proposed in this project as separate tools, within a single microfluidic platform. This would allow to investigate the combined effect of multiple stimuli on stem cell fate, thus better elucidating both their single and orchestrated contribute. From a technological point of view, this requirement could be addressed increasing the functionalities integrated within final systems. In turn, this could lead to complex technical solutions, potentially more difficult to be translated to unskilled users. In this perspective, a tradeoff between complexity and accessibility has to be reached before the introduced platforms could effectively find ordinary applicability in cell biology investigations.

A further upgrade aiming at improving the performance and the biological benefit of the proposed microfluidic platforms would be the integration of detection methods directly *on chip*. Indeed, the readout of the presented platform was mainly limited to optical microscopy techniques. Although a few traditional methods have already been proven successful to the micrometer size scale (i.e. PCR, DNA array), the majority of traditional assays requires quantities of samples typically higher than those achievable within microfluidic devices, and this cannot be integrated within microscale platforms without further innovations/optimization steps. In this perspective, more types of readouts should be conceived and adapted, also considering the possibility to introduce new assays specifically developed to take advantage of the unique characteristics of microfluidic devices (e.g. improved control over fluid flow, energy transfer and reagent delivery).

As a possible limitation, it is worth noting that the achieved miniaturization leads on one side to perform screening analyses in a high-throughput fashion, consuming small quantities of potentially rare and/or expensive samples, but suffers on the other side from a limitation in the possibility to scale up the processes. This could be considered a drawback

for example in traditional TE, in which the understanding of processes involved in cell commitment and the optimization of protocols for the generation of engineered tissues are strictly related to their final clinical applications.

In conclusion, while underlining some limitations that still have to be addressed before the widespreading of microfluidics as a common tool in cell biology, the main findings of this PhD project suggest the effective potentiality of the presented set of microfluidic platforms as a candidate starting point for the realization innovative and effective tools to support future biological and biomedical researches.

List of Publications

Papers on international peer-reviewed journals

1 **Occhetta P**, Sadr N, Piraino F, Redaelli A, Moretti M, Rasponi M. *Fabrication of 3D cell-laden hydrogel microstructures throughphoto-mold patterning.* Biofabrication, 2013 (vol.5 issue 3 pp.10) DOI: 10.1088/1758-5082/5/3/035002

2 **Occhetta P**, Visone R, Russo L, Cipolla L, Moretti M, Rasponi M. *VA-086 Methacrylate Gelatine Photopolymerizable Hydrogels: a Parametric Study for Highly Biocompatible 3D Cell Embedding.* Journal of Biomedical Materials Research: Part A, 2014 DOI: 10.1002/jbm.a.35346

3 **Occhetta P**, Malloggi C, Gazaneo A, Licini M, Redaelli A, Candiani G, Rasponi M. *High-Throughput Microfluidic Platform for Adherent Single Cells Non-Viral Gene Delivery*. RSC Advances, 2015, 5(7), 5087-5095. DOI: 10.1039/C4RA12431F

4 **Occhetta P**, Centola M, Tonnarelli B, Redaelli A, Martin I, Rasponi M. *High-Throughput Microfluidic Platform for 3D Cultures of Mesenchymal Stem Cells, Towards Engineering Developmental Processes.* Scientific Reports (Under review)

International Conferences proceedings

1. **Occhetta P,** Malloggi C, Gazaneo A, Licini M, Redaelli A, Candiani G, Rasponi M. *Microfluidic Platform for Adherent Single Cell High-Throughput Screening.* MNF 2014; London (UK) 7-10 September 2014 (pp.7)
2. Rasponi M, Gazaneo A, Bonomi A, Ghiglietti A, **Occhetta P**, Cavicchini L, Fiore GB, Pessina A, Redaelli A. *Lab-on-Chip for Testing Myelotoxic Effect of Drugs and Chemicals.* MNF 2014; London (UK) 7-10 September 2014 (pp.6)
3. **Occhetta P**, Sadr N, Piraino F, Redaelli A, Moretti M, Rasponi M. *Validation of a Novel Microscale Mold Patterning Protocol Based on Gelatin Methacrylate Photopolymerizable Hydrogels.* Summer Bioengineering Conference, ASME 2012 [SBC2012-80723]; Fajardo (Puerto Rico) 20-23 June 2012
4. **Occhetta P**, Sadr N, Piraino F, Redaelli A, Moretti M, Rasponi M. *A Photo-Mold Patterning Protocol To Microstructure Cell-Laden Hydrogels.* TERMIS 2013 European Meeting; Instanbul (Turkey) 17-20 June 2013 (pp.1)
5. **Occhetta P**, Ramella M, Boccafoschi F, Rasponi M. *A Method To Control The Mechanical Stretching Of 3D Cell-Laden Hydrogels.* TERMIS 2013 European Meeting; Instanbul (Turkey) 17-20 June 2013 (pp.1)
6. **Occhetta P**, Centola M, Tonnarelli B, Redaelli A, Martin I, Rasponi M. *High-Throughput Microfluidic Platform for the In Vitro Recapitulation of the Endochondral Development Pathway*. TERMIS 2014 European Meeting; Genova (Italy) 10-13 June 2014 (pp.1)
7. **Occhetta P**, Glass N, Rasponi M, Cooper-White JJ. *A microfluidic platform for the rapid establishment of defined cell co-cultures using chaotic mixing.* NanoBio Australia Conference 2014; Brisbane (Australia) 6-10 July 2014 (pp.1)

8. **Occhetta P**, Russo L, Arrigoni C, Visone R, Redaelli A, Cipolla L, Moretti M, Rasponi M. *In Vitro Fabrication Of 3D Cell-Laden Microenvironment Through Gelatin-Derived Hydrogel Photo-Mold Patterning.* WBC 2014; Boston (USA) 6-11 July 2014 (pp.1)

Contributions in international books

1. **Occhetta P**, Biffi E, Rasponi M. *A reliable reversible bonding method for perfused microfluidic devices.* Microfluidic and Compartmentalized Platforms for Neurobiological Research. Neuromethods Series, Springer Science, 2014 (In press)

National Conference proceedings

1. **Occhetta P**, Sadr N, Piraino F, Redaelli A, Moretti M, Rasponi M. *Control the geometry of photopolymerizable hydrogels through a novel microscaled mold patterning protocol.* In: Atti del Terzo Congresso Nazionale di Bioingegneria GNB 2012, Roma 26-29 June 2012.

2. **Occhetta P**, Centola M, Tonnarelli B, Redaelli A, Martin I, Rasponi M. *High-Throughput Microfluidic Platform for the In Vitro Recapitulation of the Endochondral Development Pathway.* GNB 2014; Pavia 25-27 June 2014 (pp.3)

3. **Occhetta P**, Malloggi C, Gazaneo A, Redaelli A, Candiani G, Rasponi M. *High-Throughput Microfluidic Platform for Adherent Single Cell Screening.* GNB 2014; Pavia 25-27 June 2014 (pp.3)

4. Rasponi M, Gazaneo A, Bonomi A, **Occhetta P**, Cavicchini L, Coccé V, Sisto F, Fiore GB, Pessina A, Redaelli A. *Lab-on-Chip for testing myelotoxic effect of drugs and chemicals.* GNB 2014; Pavia 25-27 June 2014 (pp.3)